MICROCOPY RESOLUTION TEST CHART

NATIONAL BUREAU OF STANDARDS-1963-A

②

WAVE PROPAGATION IN HETEROGENEOUS MEDIA

by

CHAIRAT SUDDHIPRAKARN

supervised by
Jose M. Roesset

AD-A150 800

a report on research
sponsored by
United States Air Force
Office of Scientific Research
Bolling Air Force Base

DTIC
ELECTE
S MAR 0 1 1985
E D

85 02 15 103

REPORT DOCUMENTATION PAGE

1a. REPORT SECURITY CLASSIFICATION	1b. RESTRICTIVE MARKINGS
UNCLASSIFIED	

2a. SECURITY CLASSIFICATION AUTHORITY	3. DISTRIBUTION/AVAILABILITY OF REPORT
	APPROVED FOR PUBLIC RELEASE;
2b. DECLASSIFICATION/DOWNGRADING SCHEDULE	DISTRIBUTION LIMITED

4. PERFORMING ORGANIZATION REPORT NUMBER(S)	5. MONITORING ORGANIZATION REPORT NUMBER(S)
	AFOSR-TR- 85-0099

6a. NAME OF PERFORMING ORGANIZATION	6b. OFFICE SYMBOL (If applicable)	7a. NAME OF MONITORING ORGANIZATION
UNIVERSITY OF TEXAS AT AUSTIN		AFOSR/NA

6c. ADDRESS (City, State and ZIP Code)	7b. ADDRESS (City, State and ZIP Code)
DEPARTMENT OF CIVIL ENGINEERING	Bolling AFB DC.

8a. NAME OF FUNDING/SPONSORING ORGANIZATION AIR FORCE OFFICE OF SCIENTIFIC RESEARCH	8b. OFFICE SYMBOL (If applicable) AFOSR/NA	9. PROCUREMENT INSTRUMENT IDENTIFICATION NUMBER
		AFOSR-83-0062

8c. ADDRESS (City, State and ZIP Code)	10. SOURCE OF FUNDING NOS.			
	PROGRAM ELEMENT NO.	PROJECT NO.	TASK NO.	WORK UNIT NO.
BOLLING AFB, DC 20332	61102F	2307	C1	

11. TITLE (Include Security Classification)
WAVE PROPAGATION IN HETEROGENEOUS MEDIA (UNCLASSIFIED)

12. PERSONAL AUTHOR(S)
CHAIRAT SUDDHIPRAKARN

13a. TYPE OF REPORT	13b. TIME COVERED	14. DATE OF REPORT (Yr., Mo., Day)	15. PAGE COUNT
ANNUAL	FROM 2-1-83 TO 2-15-84	JUNE 1984	182

16. SUPPLEMENTARY NOTATION
Originator-supplied keywords:

17.	COSATI CODES		18. SUBJECT TERMS (Continue on reverse if necessary and identify by block number)
FIELD	GROUP	SUB. GR.	WAVE PROPAGATION, EFFECT OF INCLUSIONS, SOIL DYNAMICS PROPAGATION VELOCITIES, ATTENUATION.

19. ABSTRACT (Continue on reverse if necessary and identify by block number)

The propagation of stress waves due to a point type excitation in the form of a sinusoidal pulse in an infinite medium with inclusions having different properties is studied. The solution is carried out using the boundary element method in the frequency domain with a Discrete Fourier transform. The inclusion-medium interfaces are discretized using a constant element which assumes a uniform stress and displacement field over the element. Studies were conducted primarily with a two-dimensional plane strain model but some were also performed in the three-dimensional case, focusing on the attenuation characteristics and the velocity of the wave in terms of the arrival time for both the free field and the case with inclusions. Results are presented in the form of a dimensionless displacement and arrival times at the target under consideration. With a point excitation, as used in this study, the free field attenuation follows the geometrical damping law for both the two and the three-dimensional cases, except at distances in the neighborhood of one wavelength or closer, where a more complex pattern

20. DISTRIBUTION/AVAILABILITY OF ABSTRACT	21. ABSTRACT SECURITY CLASSIFICATION
UNCLASSIFIED/UNLIMITED ☒ SAME AS RPT. ☐ DTIC USERS ☐	UNCLASSIFIED

22a. NAME OF RESPONSIBLE INDIVIDUAL	22b. TELEPHONE NUMBER (Include Area Code)	22c. OFFICE SYMBOL
Lt Col Lawrence D Hokanson	202/767-4935	AFOSR/NA

DD FORM 1473, 83 APR EDITION OF 1 JAN 73 IS OBSOLETE.

of waves is developed. Some comparative studies were also performed using the finite element method by integrating the equations of motion in the time domain with an explicit integration scheme. The results were similar to those of a system with a small amount of damping. Cases with different sizes, shapes and properties of inclusions as well as different arrangements of an inclusion cluster were studied and their effects on the attenuation and velocity of the wave were investigated. Results show that while the effect on the amplitude and the arrival time depends on the wavelength and the relative size of the inclusions, the attenuation rate is practically unchanged. The arrival time of the wave is affected more by a single inclusion than a cluster of inclusions with the same total area.

WAVE PROPAGATION IN HETEROGENEOUS MEDIA

by

CHAIRAT SUDDHIPRAKARN, B.ENG, M.ENG.

supervised by

Jose M. Roesset

a report on research

sponsored by

United States Air Force

Office of Scientific Research

Bolling Air Force Base

June, 1984

ACKNOWLEDGEMENTS

There are many individuals whose encouragement, support, and advice make this work possible.

I owe, first of all, a great debt to Professor Jose M. Roesset who not only guided me throughout the development of this research but also helped me in many ways with kindness and concern.

I also want to express my thanks to Professor Kenneth H. Stokoe who gave practical advice, and to Professor John L. Tassoulas who helped on theoretical points in the early stage of my work. Appreciation is also extended to other members of my committee, Professor Stephen G. Wright and Professor Ching-Hsu Yew, for reviewing my manuscript.

There are also many friends whose contributions were invaluable in times of crises: Rozlan Taha, Saphachai Apisaksiri, Pana Thongmeear- kom, Wijit Siripun, and Somchai Supphatada, for offering me places to stay this past year; Joe Kimbel for allowing me to use an IBM typewriter; Frank Jackson for reviewing Chapter 4; Lisa Merritt for typing most of

the first draft and some figures of the final draft; and finally, Barbara Hull for her constant encouragement, support and companionship.

Last, and most of all, my deepest gratitude goes to my brother, Sumitt, from whom I have been receiving both moral and financial support through all these years. I owe him an enormous debt that can never be repaid.

ABSTRACT

The propagation of stress waves due to a point type excitation in the form of a sinusoidal pulse in an infinite medium with inclusions having different properties is studied. The solution is carried out using the boundary element method in the frequency domain with a Discrete Fourier transform. The inclusion-medium interfaces are discretized using a constant element which assumes a uniform stress and displacement field over the element. Studies were conducted primarily with a two-dimensional plane strain model but some were also performed in the three-dimensional case, focusing on the attenuation characteristics and the velocity of the wave in terms of the arrival time for both the free field and the case with inclusions. Results are presented in the form of a dimensionless displacement and arrival times at the target under consideration. With a point excitation, as used in this study, the free field attenuation follows the geometrical damping law for both the two and the three-dimensional cases, except at distances in the neighborhood

of one wavelength or closer, where a more complex pattern of waves is developed. Some comparative studies were also performed using the finite element method by integrating the equations of motion in the time domain with an explicit integration scheme. The results were similar to those of a system with a small amount of damping. Cases with different sizes, shapes and properties of inclusions as well as different arrangements of an inclusion cluster were studied and their effects on the attenuation and velocity of the wave were investigated. Results show that while the effect on the amplitude and the arrival time depends on the wavelength and the relative size of the inclusions, the attenuation rate is practically unchanged. The arrival time of the wave is affected more by a single inclusion than a cluster of inclusions with the same total area.

TABLE OF CONTENTS

LIST OF FIGURES

vii

LIST OF TABLES

LIST OF SYMBOLS

a	least dimension of an inclusion.
A	amplitude of the displacement.
A_f	amplitude of the displacement for the free field.
b	subscript for inclusions.
b_i	body force components.
B	matrix relating element strains to nodal displacement.
c_s	shear wave velocity.
c_{sb}	shear wave velocity of the inclusion.
c_p	compression wave velocity
c_1, c_2	constants controlling the natural period of a finite element.
c_n	Fourier components.
d	distance from source to target.
d_b	total distance in the inclusions along the principal wave path.
D	damping ratio, matrix relating stresses to strains in the finite element
e	superscript indicating "element".
e_i	unit normal vector components
f_{max}	highest frequency in the frequency domain analysis.
f_p	frequency of the excitation including the quieting period.
f_s	frequency of the sinusoidal part of the excitation.
f_{tr}	truncated frequency.

F	force per unit length, the peak amplitude of an excitation force.
G	shear modulus, boundary matrix.
G_b	boundary matrix of an inclusion.
H	boundary matrix.
H_b	boundary matrix of an inclusion.
I	identity matrix.
K_0	modified Bessel's function of the second kind of order zero.
K_1	modified Bessel's function of the second kind of the first order.
K_2	modified Bessel's function of the second kind of the second order.
M	mass matrix.
N	matrix of the displacement function, number of points in time.
N_f	number of the frequency points.
NFR	number of frequency points used in the interpolation method.
DFR	frequency increment used in the interpolation method.
$p(t)$	loading function.
r	distance between the point on the boundary element and the point of application of a virtual force.
R	external load vector.
t	time, subscript indicating at time t.
t_i	traction components.
T	period of vibration, traction vector.
T_p	period of the excitation including the quieting period.

T_s	period of the excitation of the sinusoidal part.
u_i	displacement components.
u_o	displacement component for the free field.
$u(t)$	total response.
U	displacement vector.
$\dot{U}$	velocity vector.
$\ddot{U}$	acceleration vector.
U_o	free field displacement vector.
$U(\omega)$	frequency response for a unit concentrated harmonic excitation.
Z	argument for the modified Bessel's function.
α	constant
γ	unit weight, Euler's constant.
Γ	symbol representing boundary.
δ_{ij}	Kronecker's delta.
Δ	Dirac delta function.
ε	small radius of a semi circle or a hemisphere in the boundary element formulation.
η_i	unit normal vector component.
λ	wavelength.
ν	Poisson's ratio.
ρ	mass density.
ω	circular frequency.
Ω	circular frequency, symbol representing a domain.
χ	function definded in text.

ψ function definded in text.

ℓ length of one dimensional element, least dimension of two or three dimension elements, subscript indicating point on the boundary element.

*   superscript indicating the virtual state.

^   a cap indicating the transformed domain parameter.

CHAPTER 1

INTRODUCTION

The study of elastic stress wave propagation has regained momentum in recent years because of increasing needs for accurate information in the field of seismology, earthquake engineering and soil dynamics. Recent developments in electronic instrumentation have made the detection of small amplitude motion due to stress waves possible, and the experimental work in this area can now cope with the advances that had been made on the theoretical side. This has resulted in an increasing number of papers on both the experimental and the theoretical aspects of the problem. Another reason for this change is the development in the field of material science with the application of the stress wave technique in the investigation of material properties. Finally, the application of seismic techniques in geophysics and the study of the propagation of stress pulses of large amplitude, which is particularly important from the engineering point of view, make the subjects even more interesting.

In dealing with wave propagation in soil deposits where the state of stress varies depending on the geological conditions, the information on the effect of the general state of stress on the velocity of waves is very important, but the experimental results available on this area are still limited. A research program was, therefore, con-

ducted at the Geotechnical Engineering Division, University of Texas, Austin, to investigate these effects at low levels of strain. A large scale triaxial testing device, which is a reinforced steel cube designed to hold a cubic soil sample measuring 7 ft. on each side, was used. The waves are generated along the principal axes through one of three excitation ports located on three walls of the cube. Accelerometer packages are embedded in the soil along each principal axis of the cube to monitor the waves.

The first motivation for the present work arose from the need to investigate: (1) the effect of the much stiffer (almost rigid) accelerometer packages mentioned above on the characteristics of the waves propagating through the soil, and (2) how well the motion of the accelerometer package itself represents the soil motion. The original investigation was conducted using the finite element method with an explicit integration scheme, which was appropriate for this particular problem because of the finite domain. The results of the first investigation were presented in Stokoe et al (1980). Further studies were also performed on the same problem using the same numerical model to investigate the effect of different boundary conditions, different types of excitation and different wavelengths (or frequencies of excitation). The results of these studies were presented in Suddhiprakarn (1983).

There are increasing interests in the problem of diffraction and scattering of elastic waves by obstacles or inclusions in recent years, because of its wide range of applications in engineering, geophysics, acoustic and military applications. It was, therefore, decided to

investigate further the more general area of wave propagation in a medium with inclusions having different properties. Instead of a finite domain representing a large triaxial cube, as used in the previous studies, a full space was considered. The main reason for this was to eliminate the boundary effects and to concentrate only on body waves.

In this work, the boundary element method is used and the problems are solved in the frequency domain with the application of the Fourier transform. The numerical model consists of an infinite space with a unit point excitation, inclusions and target points where the results are calculated. The target points can also be located at the inclusion surface. The number of inclusions, their shapes and their arrangements can be varied arbitrarily as long as the number of boundary elements used does not exceed the maximum limit. The properties of a medium and the inclusions can also be selected to handle a wide range of situations. Both three-dimensional and two-dimensional plane strain models are developed. The formulation based on the boundary element method and a frequency domain analysis is presented in Chapter 4.

Some results are also obtained using the finite element model to compare with those from the boundary element method. The finite element model from those of the early investigations is modified to handle an infinite space problem as considered in this work. The formulation, which was not shown in the early work, is presented in Chapter 3.

In Chapter 5, a preliminary investigation on the effect of some important parameters involving both numerical models are presented. In the finite element model, the investigation involves the size of the

4

domain necessary to represent an infinite medium. In the boundary element model, most of the investigation focuses on the Fourier transform parameters.

Chapter 6 shows the effects of inclusions of different sizes and properties on the waveform and the attenuation characteristics of the wave. In Chapter 7, the arrival time of the wave and the effect from inclusions having different sizes, shapes, and properties are presented. The effect of an inclusion cluster versus a single inclusion are also discussed. Conclusions from the results in Chapter 6 and Chapter 7 are presented in Chapter 8.

CHAPTER 2

BACKGROUND

2.1 WAVE PROPAGATION

The study of elastic wave propagation originated from the attempt to explain the true nature of light, which was thought, in the early nineteenth century, to be the propagation of a disturbance in an elastic aether. After the research of Fresnel (1788-1827) and Young (1773-1829) on the polalization of a light beam, it was concluded that light could be explained only by transverse waves in an elastic aether. This conclusion paved the way for further studies of elasticity and wave propagation by many great mathematicians. Navier (1785-1836), who was the first to investigate the general equations of equilibrium and vibration of elastic solids, presented a molecular theory of an elastic body, giving an equation of motion in terms of the displacement of the material point (molecule).

In 1822, Cauchy (1789-1857) developed what is known today as the "Mathematical Theory of Elasticity", including the stress and displacement equation of motion which agreed with Navier's in some aspects. In 1828, Poisson (1781-1840) succeeded in solving the differential equation of motion for an elastic solid by decomposing the displacement into an

irrotational and equivoluminal part, with each being a solution of a wave equation. This led to the conclusion that an elastic disturbance was in general composed of two types of fundamental waves, the longitudinal (irrotational) and transverse (equivoluminal) waves.

Further important investigations made earlier on the propagation of elastic waves were carried on by several investigators such as Ostrograsky, Green, Stokes, Lame, Clebsch, and Christoffel. The history of the studies on elastic waves and theory of elasticity is presented in detail by Love (1944).

In the transition period between the end of the nineteenth century and the beginning of the twentieth century, the study of waves in elastic solids regained momentum due to applications in the field of geophysics. There are several contributions in this period especially in the area of wave propagation in an elastic half space. In 1887, Rayleigh discovered his now well-known surface wave, which is a very significant type of wave involving a traction free surface. In 1904, Lamb was the first to study the propagation of a pulse in an elastic half space. This problem is of primary importance in the field of seismology, and was further studied by many researchers such as Nakano, Lapwood, Sobolev, Smirnov, Stoneley, and Cagniard.

Since World War II, the research on elastic wave propagation has expanded at an increasing rate due to the need for information on earthquake phenomena, nuclear explosions and the performance of structures under high rates of loading. A survey of most of the contributions in this field until 1965 was cited in Miklowitz (1966). Ewing et al (1956)

gave a comprehensive treatment of elastic waves with extensive references on most topics. More recent comprehensive books on general elastic wave propagation have been written by Achenbach (1973), Eringen and Suhubi (1975), and Miklowitz (1978).

2.2 DIFFRACTION OF ELASTIC WAVE

The term diffraction was given by Grimaldi (1618-1663) to the phenomenon of a light beam bending slightly while passing the edge of an aperture. Nowaday, this term is applied to a phenomenon of wave propagation when the wave rays deviate from rectilinear paths, which cannot be interpreted as reflection or refraction. The definition of a scattered wave, on the other hand, is not as clear. Rayleigh's definition is that the scattered wave is the difference of the total wave field observed in the presence of an obstacle and the incident wave (or the free field) which means that the scattered wave may contain the reflected wave or the combination of the refracted and diffracted wave depending on the position of the target. Outside the field of molecular physics, the term scattering and diffraction are often used to describe the same wave phenomenon. When the diffracted wave forms the major part of the scattered wave, as in the case of an obstacle with sharp edges, the term "diffraction" is normally used. On the other hand, when the diffracted part of the wave is less significant as in the case of an obstacle without sharp edges, the term "scattering" is preferred.

8

In parallel to the development of the elastic theory of light, the studies on diffraction and scattering phenomena was also developed. The first attempt was made by Stokes, who studied the diffraction of light by an aperture in a screen, and Clebsch, who studied the reflection and transmission of light through lenses. A few years later, Rayleigh discussed the scattering of light by very small particles in relation to the wavelength and explained why the sky is blue. Rayleigh was also the first to study the scattering of sound waves by a spherical obstacle having different density and compressibility than the surrounding air. He considered plane as well as spherical waves and the results confirmed his law of scattering known as Rayleigh's scattering, which involved a small scatterer and large incident wavelengths.

There were several further studies of the diffraction and scattering on both electromagnetic and elastic solid waves by various investigators. The interest in the diffraction of waves in an elastic solid, however, had declined for some time. After the paper published in 1927 by Sezawa of the Tokyo Imperial University on the scattering of an incident compressional wave by circular and elliptical cylinders as well as by a sphere, numerous publications followed, all of which dealt only with a sinusoidal incident wave, i.e. with a steady state response. The problems of the transient response, on the other hand, have been investigated only in recent years with the first contribution by Baron and Matthews (1961) who calculated the stress response at the surface of a cylindrical cavity by a step compressional wave. Pao and Mow (1973) presented a comprehensive review of literature and treatment on the subject

focusing on the dynamic stress concentration. Some solution methods and results on the diffraction of elastic waves by circular and spherical scatterers with emphasis on the transient problems are also presented in Miklowitz (1978).

Due to the increasing complexities of the geometry of the problem together with the development of powerful digital computers during the last decade, more research has been oriented toward the application of numerical models to solve the problem of wave propagation and diffraction.

2.3   BOUNDARY ELEMENT METHOD

Most of the problems in the field of engineering and science are usually formulated by considering the behaviour of an infinitesimal element of the system with an assumed relationships between the variables involved. This leads to a set of differential equations that describes the nature of the system. It had long been realized, especially for the case of partial differential equations, that general solutions are not so useful as the solutions for specific problems where the initial and boundary conditions are given. The solutions of such initial value or boundary value problems has been of major concern to investigators for many years.

The majority of the practical problems often involve complicated boundary conditions and parameters which are not tractable with analytical solutions. Numerical methods become then the only feasible means to

obtain reliable results. The most widely used numerical methods at present manipulate directly the original differential equations using various approximation techniques. These approximations can be done either by replacing the differential in the equations by difference operators and satisfying the governing equations at certain discrete points, as in the finite difference method, or dividing the continuous domain into subdomains, each having a finite number of degree of freedom, as in the finite element method.

The boundary element method (BEM),sometimes called the boundary integral equation method (BIEM), follows a different approach. Instead of working directly on the original set of differential equations, these governing differential equations are converted into a set of integral equations before applying any discretization or approximation scheme. The resulting integral equations to be discretized involve only the value of the variables at the extreme range of the integration, i.e. on the boundaries of the region. This implies that the subsequent discretization scheme needs to be done only at the boundary of the domain and the spatial dimensions of the problem are reduced by one. The distribution function for the field variables over each discretized element can be uniform, linear, or higher order, similarly to the finite element method.

The boundary element method resulted from the advancements made in the theory of integral equations and the development of digital computers. In the pre-computer era, the study of integral equations and their application to various types of boundary and initial value prob-

lems had been a topic of interest to mathematicians for years. The first rigorous investigations on the general theory of the subject was made by Volterra (1860-1940) and later by Fredholm (1866-1927) who also treated the subject in conjunction with the theory of linear elastostatics. Since then integral equations have been studied intensively by mathematicians and investigators in the field of theoretical mechanics, notably among Russian workers as Muskhelishvili, Mikhlin and Kupradze. Recent analytical work along these lines has been done in the areas of steady state elastodynamics (Kupradze, 1963) and transient elastodynamics (Doyle, 1966). With the development of high speed digital computers, many investigations have been carried out to obtain boundary element formulations and to implement a general numerical algorithm for solving a wide range of practical problems.

Boundary element methods are classified by most investigators into three different types:

1. **Indirect Formulation.** In this formulation, the integral equations are formulated in terms of a unit singular solution that satisfies the original differential equation such as the free-space (infinite domain) Green's function. This unit singular solution is distributed over the boundary of the region in a manner specified by density functions which are unknowns and have to be obtained in the numerical solution process. Once the density functions are known, the solution anywhere within the body can be calculated by a simple integration process. Algorithms based on the indirect formulation were

presented in Massonet (1965) and Oliveira (1968). Banerjee (1971);
and, Tomlin and Butterfield (1974) extended and improved the algo-
rithm to two and three dimensional problems involving buried founda-
tion as well as nonhomogeneity and orthotropy of the medium.

2. **Direct Formulation.** The unknown functions in the integral equations
of this formulation are the actual physical variables of the prob-
lem. The algorithm was first developed by Rizzo (1967) for the elas-
tostatic problem; Cruse (1968), Cruse and Rizzo (1968) applied it to
transient elastodynamic problems. Using Betti-Maxwell reciprocal
theorem, they derived Somigliana's identity for the displacement
inside the body due to known surface displacements and tractions.
The integral equation relating displacements and tractions on the
boundary was then obtained by taking the limiting case of
Somigliana's identity. This direct formulation can also be derived
as a special case of a generalized FEM based on the Galerkin weighted
residual technique as in Zienkiewicz (1978), Brebbia (1978), or
Brebbia and Walker (1980).

3. **Semi-direct Formulation.** In this formulation, the integral
equations are formulated in terms of selected unknown functions such
as stress functions or stream functions for elasticity and flow
problem respectively. The physical solution can then be obtained from
these unknown functions by simple mathematical operation. This for-

mulation was used in the work of Jaswon and Ponter (1963) and Symm (1963).

The boundary element method has become very popular and has been successfully applied to a variety of linear problems in elastostatics, elastodynamics, potential theory, fracture mechanics, fluid-structure interaction, soil structure interaction, porous media flow, etc. A comprehensive account of these applications was collected in the books by Cruse and Rizzo (1975), Brebbia (1978), Brebbia and Walker (1980), Brebbia (1981), Banerjee and Butterfield (1981) and Liggett and Liu (1983).

For the transient elastodynamic problem, the method is very useful especially in the field of geophysics and dynamic soil structure interaction. In this case, the boundary element method can be applied in conjunction either with integration in the time domain as in Cole et al (1978), or with frequency domain analysis using Laplace or Fourier transform as in Dominguez (1978). With the recent development of the dynamic Green's function for a half space (Johnson, 1974), and a layered half space (Luco and Apsel, 1983), the research on the application of the boundary element method in dynamic geotechnical engineering and geophysics appears to be a very promising area.

CHAPTER 3

FINITE ELEMENT FORMULATION

To solve the problem of wave propagation in an infinite medium with inclusions using finite elements, it is necessary to represent an infinite domain with a finite one. This approximation can give good results if the boundaries of the domain are extended far enough so that the amplitude of the reflected waves reaching the region of interest is very small (if there is internal damping), or so that the time of arrival of these reflected waves exceeds the duration of interest. At the same time, the size of the finite element mesh should be fine enough to reproduce accurately the propagation of waves of a given wavelength. With these constraints, if a formulation that requires the assembly of the global stiffness matrix is used, it will result in an extremely large system of equations which is impractical to handle. With some simplified assumptions involving the use of a diagonal mass matrix and neglecting velocity-dependent damping forces, it is possible, however, to solve the problem using an explicit integration scheme, such as the central difference method, and then marching out the solution in the time domain. The solution can essentially be carried out at the element level without assembling the global stiffness matrix. This numerical scheme can drastically reduce the size of computer storage required. The solution is,

still, time consuming since the time step of integration must be kept sufficiently small to guarantee stability.

To keep the computation cost within a reasonable limit, only a two-dimensional finite element model with four-node linear elements will be used and presented in this chapter.

3.1   FINITE ELEMENT MODEL

The concept of the finite element method is very broad and can be applied in a number of different formulations. In this work, the stiffness or displacement method is used. This method is based on assuming functions to approximate the displacement field for each element. These displacement functions can be expressed in various forms, the simplest linear functions for four-node rectangular element will be used here. The equations of equilibrium for a finite element system in motion can then be derived either by using the principle of virtual displacement in conjunction with d'Alembert forces or by applying Hamilton's principle.

3.2   EQUATION OF EQUILIBRIUM

With the viscous damping term neglected for simplicity, the equation of equilibrium derived for a finite element system can be written as

$$\ddot{M}U + KU = R \qquad\qquad (3.1)$$

where M and K are mass and stiffness matrices; R is the external load vector; U and Ü are the displacement and acceleration vectors of the finite element assemblage.

The stiffness matrix K is formed by assembling each element stiffness matrix K^e which is expressed as

$$K^e = \int_{\Omega^e} B^T DB \, d\Omega^e \qquad\qquad (3.2)$$

where B is a matrix relating element strains to nodal displacements; D is a matrix relating stresses to strains in the element and sometimes called the element elasticity matrix. The integral above is carried out over the region Ω^e of the element.

The only external load considered in our case is the concentrated load at the excitation point. The element mass matrix M^e is in the form

$$M^e = \int_{\Omega^e} \rho N^T N \, d\Omega^e \qquad\qquad (3.3)$$

where ρ is the mass density, and N denotes the matrix of assumed displacement functions.

The element mass matrix resulting from (3.3) is called the consistent mass matrix because the same displacement functions (sometimes, called the basis functions) are used to formulate the stiffness and mass

matrices. If this consistent mass matrix is used, the resulting global mass matrix M will be non-diagonal. It is, however, not a requirement for convergence to use a consistent mass matrix; therefore, different functions may also be used. If the basis functions that have unit value over the region tributary to the node under consideration and zero elsewhere are used and the tributary regions do not overlap, the resulting matrix M will be diagonal. The use of a diagonal (or lumped) mass matrix involves much less computational effort and suffers no loss in order of convergence and accuracy in most cases especially in wave propagation problems with linear displacement expansions (Scaletti, 1977).

For the finite element numerical scheme used in this work, it is necessary to use a diagonal mass matrix because the solutions will be carried out on the element level without assembling the global matrices. Furthermore, the benefits of a diagonal mass matrix are evident when applying a conditionally stable integration scheme since the element will have a lower natural frequency (i.e., larger natural period) and a larger time step of integration may be used.

3.3   DIRECT INTEGRATION METHOD

Mathematically, Equation (3.1) represents a system of linear differential equations of second order which can be solved by integration using a numerical step-by-step procedure. The numerical integration is based on approximations. First, the equilibrium equation (3.1) is satisfied only at each discrete time (with interval Δt) instead

of at any time t; second, a variation of displacements, velocities, and accelerations within each time interval Δt is assumed. The first one is the basis for all finite difference methods. The latter concept differentiates one method from another (such as central difference and forward difference methods, etc.) and determines the accuracy, stability, and cost of the solution procedure.

One of the procedures that is effective and will be used in this work is the central difference method which assumes that

$$\ddot{U}_t = \frac{(U_{t+\Delta t} - 2U_t + U_{t-\Delta t})}{\Delta t^2} \qquad (3.4)$$

where the subscripts in the above equation denote the discrete time at which the values are obtained.

The velocity expansion which has the same order of error is

$$\dot{U}_t = \frac{(U_{t+\Delta t} - U_{t-\Delta t})}{2\Delta t} \qquad (3.5)$$

Considering the equilibrium equation (3.1) at time t

$$M\ddot{U}_t + KU_t = R_t \qquad (3.6)$$

and substituting the relations for $\ddot{U}_t$ in (3.4) into (3.6), we get

$$(\frac{1}{\Delta t^2}M)U_{t+\Delta t} = R_t - (K - \frac{2}{\Delta t^2}M)U_t - (\frac{1}{\Delta t^2}M)U_{t-\Delta t} \qquad (3.7)$$

The method assumes that the initial conditions (the displacement, velocity, and acceleration at time t = 0) are known. The solutions at the next time steps are then calculated using Equation (3.7) up to the end of the time span under consideration. Since the solution of $U_{t+\Delta t}$ is calculated using the equilibrium conditions at time t instead of at time t+Δt, the method is called an explicit integration scheme.

Equation (3.7) can be rewritten in the form of summations of the element matrices

$$\sum_e \frac{1}{\Delta t^2} M^e U_{t+\Delta t} = [\sum_e (R_t^e - K^e U_t)] + [\sum_e \frac{1}{\Delta t^2} M^e (2U_t - U_{t-\Delta t})] \quad (3.8)$$

If the global mass matrix M is diagonal, Equation (3.7) can be solved without factoring a matrix, and only matrix multiplication are necessary on the right hand side of (3.7). Let m_i denotes the ith diagonal element of the mass matrix M, the ith components of the vectors $U_{t+\Delta t}$ can be determined from (3.8) as

$$U_{t+\Delta t}^i = \frac{\Delta t^2}{m_i} [\sum_e (R_t^e - K^e U_t)^i] + 2U_t^i - U_{t-\Delta t}^i \quad (3.9)$$

where the summation term indicates the result of $R_t^e - K^e U_t$ for the ith components contributed by each element 'e'. Therefore, all calculations can be done at the element level and the solutions can be marched out in the time domain without assembling the global stiffness matrix. The method becomes even more effective when the element stiffness matrices

K^e of all elements are the same since only one element stiffness matrix needs to be calculated. It can be stored and then recalled for uses.

In the formulation shown in (3.9), it is possible to include the damping terms without a significant increase in the cost of computation if the damping matrix is diagonal. With this condition, the benefits of performing the solution on the element level are still preserved. Since the main purpose of the finite element formulation is to check and compare with the boundary element method (BEM) and since the same type of damping cannot be incorporated into both models, the damping terms are, however, neglected.

3.4 TIME STEP OF INTEGRATION

The central difference method used in the formulation presented in Section 3.3 is classified as a conditionally stable integration scheme. It requires that the time step Δt be smaller than a critical value Δt_{cr} to guarantee stability, i.e

$$\Delta t \leq \Delta t_{cr} = \frac{T}{\pi} \qquad (3.10)$$

where T is the minimum period of the finite element assemblage. This minimum period T can be calculated using any of the numerical techniques available for the solution of eigenproblems, which is not possible in our case. Since the solution for a large eigenvalue problem is also time consuming and expensive, it is not practical to solve the large eigenva-

lue problem just to determine the appropriate time step Δt for the direct integration method. A simpler method is to determine a lower bound for T which is controlled by the smallest natural period of any element in the finite element model. The minimum period for a single element can be calculated numerically from the stiffness and mass matrices of the element or it can be determined from

$$T_{min} = c_1 c_2 \sqrt{(0.5 - \nu)} \frac{\ell}{c_s} \tag{3.11}$$

The equation above applies for a four-node, rectangular, plane strain element where ℓ is the minimum element dimension, c_s is the shear wave velocity, ν is Poisson's ratio, c_1 is either π for lumped masses or $\pi/\sqrt{3}$ for consistent masses, and c_2 is a shape factor, equals to 1 for a square element.

The benefit of using lumped masses over a consistent mass matrix mentioned above is evidenced by Equation (3.11). The lumped mass approximation results in a larger natural period, hence a larger time step Δt may be used. On the other hand, any reduction in the size of one single element (which will reduce a certain diagonal element in a global mass matrix) will decrease the minimum period T of the system. Any increases in the stiffness (or shear wave velocity c_s) on one element will have the same effect.

3.5   FINITE ELEMENT MESH AND BOUNDARY CONDITIONS

In this work, four-node square elements with linear basis functions will be used. All elements used in the model are the same in order to take advantage of the solution scheme mentioned earlier when all elements have the same stiffness matrices K^e. Each inclusion is represented by a single element and is assumed to be perfectly rigid with compatibility satisfied everywhere. It is also possible to modify the model for inclusions of varying stiffness but the time step of integration must be changed according to the stability criterior mentioned in Section 3.4.

The size of a finite element mesh relative to the wavelength determines the accuracy of the results. Typically, nodal spacing in the direction of the propagating wave should range from 1/4 to 1/10 of the shortest wavelength of interest, and the value of 1/8 will be used throughout this work.

For a finite element model, an infinite medium is approximated by a finite domain with fixed or free boundaries. These boundaries may hamper any motions in their vicinity; in addition, the reflected waves from these boundaries will be combined with the direct wave making interpretation of the results more difficult. Therefore, the domain has to be sufficiently large to make boundary effects negligible over the time span of interest. The investigation for the proper size of the domain will be discussed in Chapter 5.

Since each inclusion is to be represented by a single element, the centerline of the domain, which is also the principal axis of wave

propagation, has to pass through the center of inclusions (or element) in order to take advantages of symmetry and antisymmetry. Because of these conditions, the excitation at a point has to be approximated by distributing the force evenly between two nodes as shown in the model of Figure 3.1. This approximation is not serious as long as the distance between these two nodes is small compared with the distances from the excitation point to the inclusion and the target point.
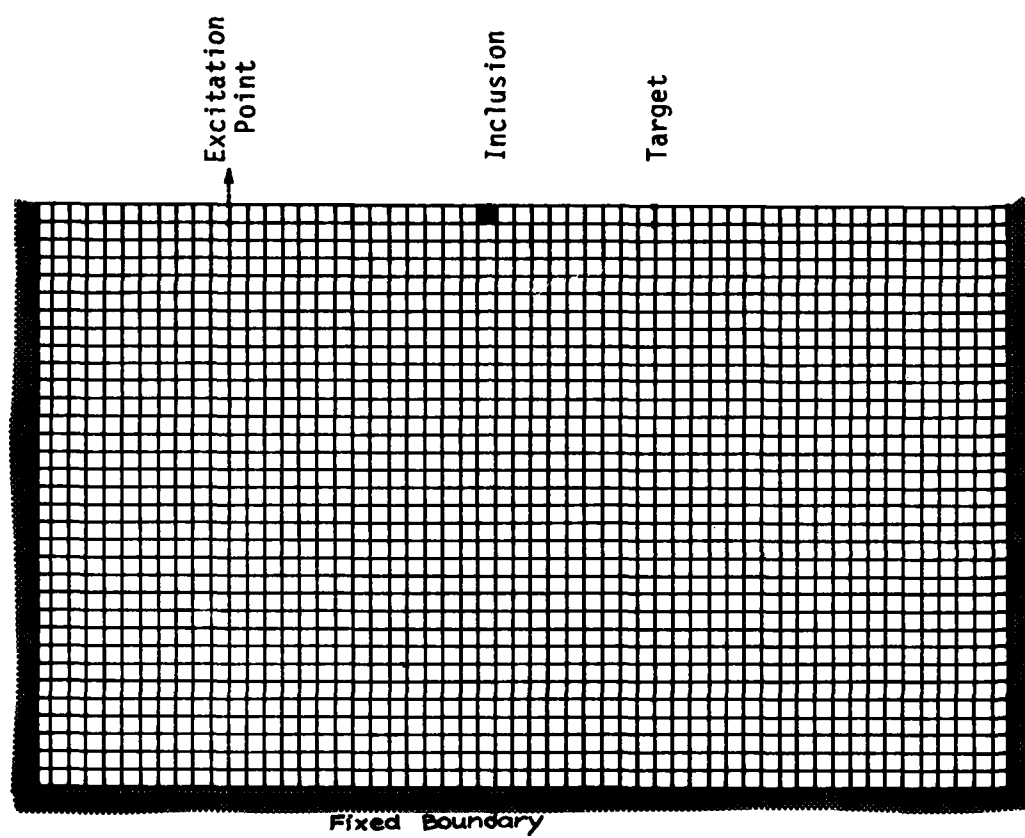
Figure 3.1 - Two Dimensional Finite Element Model

CHAPTER 4

BOUNDARY ELEMENT FORMULATION

The boundary element method is basically a solution in discrete form of the boundary integral equation that relates the tractions and the displacements over the boundaries of the domain under consideration. The discretization is achieved by dividing the boundaries into a number of smaller elements and then calculating the integrals numerically. The variations of the displacements and the tractions may be assumed to be constant or of a higher order (linear, quadratic, cubic, etc.). This procedure leads to a system of equations with the tractions, the dis-placements or both as unknowns. Once these tractions and displacements over the boundary are solved for, the results at any point inside the domain can be calculated.

For time-dependent problems, the boundary element method may be solved either in the time domain by a step-by-step integration (Cole et al, 1978) or in the frequency domain by eliminating the time variable with a Laplace transform (Cruse and Rizzo, 1968) or a Fourier transform (Dominguez, 1978). Once the equations are solved in the transformed space, the original variable involving the time dependence may be recovered by inverting the transform numerically.

The boundary element formulation described in this chapter is based on the method used by Dominguez (1978), who studied the dynamic stiffness of surface and embedded foundations. For the case of wave propagation through an infinite medium with inclusions, some modifications are needed in the formulation. By working in the frequency domain using the Betti-Maxwell reciprocity relation and a fundamental solution in transform space for a unit harmonic point force in an infinite medium, an equation for displacement inside the body due to the known boundary tractions and displacements (so called Somigliana's identity) is derived. The integral equation is then formed by taking the limiting case of Somigliana's identity for points located of the boundary of the domain. By discretizing the boundaries into small elements, the boundary matrices representing a system of equations that relate the displacements and the tractions at the boundaries are formed. This formulation is carried out in two separate parts: (1) for the inclusions; and (2) for the infinite medium with cavities and an excitation by a unit harmonic point force. These two parts are then combined using equilibrium and compatibility conditions. This leads to a system of equations which can be solved for unknown displacements and tractions at the surface of the inclusions. Then, the displacements at any points inside the medium are calculated using Somigliana's identity. For a frequency domain analysis, these displacements or transfer functions are solved for different frequencies. The solution for a transient excitation can then be obtained using Fourier transforms.

The details of the boundary element formulation are presented in the following sections.

4.1   BOUNDARY ELEMENT MODELS

4.1.1   Model for Soil with Cavity

The formulation starts with the Betti-Maxwell reciprocity relation between the Fourier transforms of the actual and virtual states. Consider a body Ω with a boundary Γ under a certain system of loads (see Figure 4.1a). Assuming a virtual state '*' on the same body, the following relation can be established

$$\int_\Gamma \hat{t}_i \hat{u}_i^* \, d\Gamma + \int_\Omega \hat{b}_i \hat{u}_i^* \, d\Omega \quad = \quad \int_\Gamma \hat{t}_i^* \hat{u}_i \, d\Gamma + \int_\Omega \hat{b}_i^* \hat{u}_i \, d\Omega \qquad (4.1)$$

The usual indicial notation of Cartesian tensor analysis is used. The variables u_i, t_i, and b_i are the components of displacement, traction and body force, respectively. The sign '^' over each terms indicates that they are in the transform space (i.e., the frequency domain).

Let each component of the virtual force $\hat{b}_i^*$ be a Dirac delta function Δ^k which represents a unit concentrated force at point k, then

$$\hat{b}_i^* = \Delta^k e_i \qquad (4.2)$$
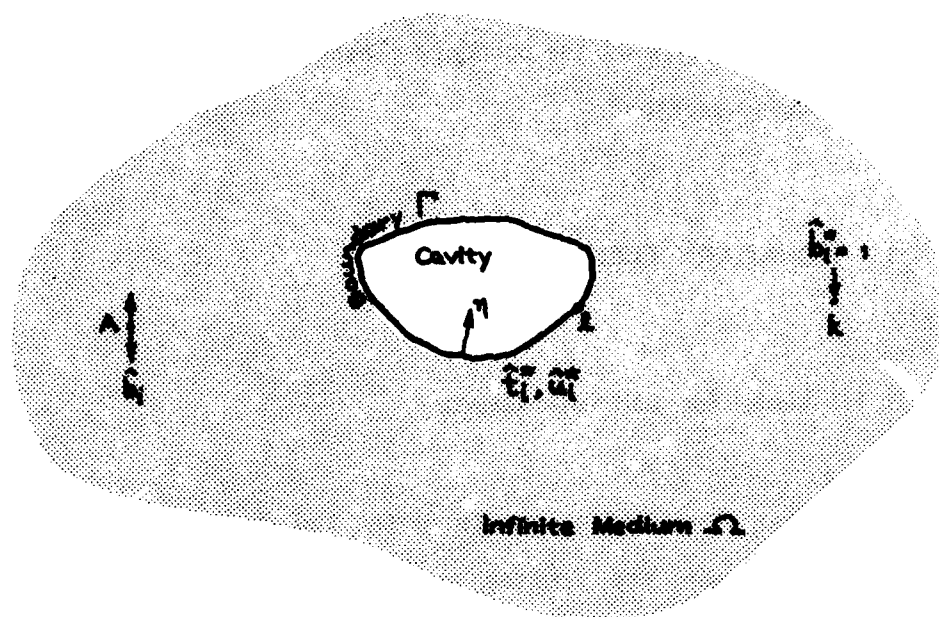
(a) Infinite Medium with an Interior Boundary (Cavity) and
an Excitation Force as a Body Force
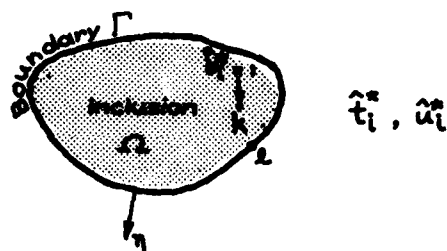
(b) Infinite Medium with an Exterior Boundary (Inclusion)

Figure 4.1 - Virtual State for an Infinite Medium

where e_i is a unit normal vector in the i direction.

The virtual state, therefore, becomes the fundamental solution, or the response of the infinite medium to a unit concentrated harmonic force applied at point P. This solution, following the works by Doyle (1966) and Cruse and Rizzo (1968), can be obtained from the equations of motion of a linear isotropic elastic body and is of the form

$$\hat{U}_{ji} = \frac{1}{\alpha\pi\rho c_s^2} [\psi\delta_{ij} - \chi r_{,i}r_{,j}] \tag{4.3}$$

$$\hat{T}_{ji} = \frac{1}{\alpha\pi} [(\frac{d\psi}{dr} - \frac{\chi}{r})(\delta_{ij}\frac{dr}{dn} + r_{,i}n_j) - \frac{2\chi}{r}(n_i r_{,j} - 2r_{,i}r_{,j}\frac{dr}{dn})$$

$$- 2\frac{d\chi}{dr} r_{,i}r_{,j}\frac{dr}{dn} + (\frac{c_p^2}{c_s^2} - 2)(\frac{d\psi}{dr} - \frac{d\chi}{dr} - \frac{\alpha\chi}{2r})r_{,j}n_i] \tag{4.4}$$

where $\hat{U}_{ji}$ and $\hat{T}_{ji}$ are respectively the displacement and traction in i direction at point ℓ due to the unit force in direction j at point k, r is the distance from k to ℓ, ρ is the mass density, c_s and c_p are the velocity of shear wave and compression wave of the medium respectively, and η is a unit outer normal vector.

In the equations above, $\alpha = 2$ for the two-dimensional case, and $\alpha = 4$ for three dimensions. The functions ψ and χ for the three-dimensional case are

$$\psi = (1 + \frac{c_s}{i\omega r} - \frac{c_s^2}{\omega^2 r^2}) \frac{e^{(-i\omega r/c_s)}}{r} - \frac{c_s^2}{c_p^2}(\frac{c_p}{i\omega r} - \frac{c_p^2}{\omega^2 r^2}) \frac{e^{(-i\omega r/c_p)}}{r} \tag{4.5}$$

$$\chi = (1 + \frac{3c_s}{i\omega r} - \frac{3c_s^2}{\omega^2 r^2}) \frac{e^{(-i\omega r/c_s)}}{r} - \frac{c_s^2}{c_p^2}(1 + \frac{3c_p}{i\omega r} - \frac{3c_p^2}{\omega^2 r^2}) \frac{e^{(-i\omega r/c_p)}}{r} \tag{4.6}$$

For the two-dimensional case, ψ and x are

$$\psi = K_0(\frac{i\omega r}{c_s}) + \frac{c_s}{i\omega r} [K_1(\frac{i\omega r}{c_s}) - \frac{c_s}{c_p} K_1(\frac{i\omega r}{c_p})] \qquad (4.7)$$

$$x = K_2(\frac{i\omega r}{c_s}) - \frac{c_s^2}{c_p^2} K_2(\frac{i\omega r}{c_p}) \qquad (4.8)$$

where K_0, K_1, and K_2 are modified Bessel functions of the second kind of orders zero, one, and two respectively. Note that

$$\hat{u}_i^* = \hat{U}_{ji} e_j$$

$$(4.9)$$

$$\hat{t}_i^* = \hat{T}_{ji} e_j$$

by substituting (4.9) and (4.2) into (4.1), we get

$$\int_\Gamma \hat{t}_i \hat{U}_{ji} e_j \, d\Gamma + \int_\Omega \hat{b}_i \hat{U}_{ji} e_j \, d\Omega = \int_\Gamma \hat{u}_i \hat{T}_{ji} e_j \, d\Gamma + \int_\Omega \hat{u}_i \Delta^k e_i \, d\Omega \qquad (4.10)$$

The dummy index of the last term of (4.10) can be changed from i to j, and

$$\int_\Omega \hat{u}_j \Delta^k \, d\Omega = \hat{u}_j^k \qquad (4.11)$$

where Δ^k and $\hat{u}_j^k$ are the delta function and displacement at point k in direction j respectively. Equation (4.10) becomes

$$\hat{u}_j^k = \int_\Gamma \hat{U}_{ji}\hat{t}_i \, d\Gamma - \int_\Gamma \hat{T}_{ji}\hat{u}_i \, d\Gamma + \int_\Omega \hat{b}_i\hat{U}_{ji} \, d\Omega \qquad (4.12)$$

Equation (4.12) is known as Somigliana's identity, which will be used later to compute the displacement at any interior point. In order to formulate the problem as a boundary technique, the virtual load point k has to be taken to the boundary. Consequently, the integral along the boundary will present a singular point. This singular integration can be done by considering the hemisphere on the boundary of a three-dimensional model (semi-circle for the two-dimensional case). The boundary point k is assumed to be at the center of the sphere, and the radius 'ε' is reduced to zero. The point will then become a boundary point.

For a smooth boundary at the point k, it can be shown that

$$\lim_{\varepsilon \to 0} \int_{\Gamma_\varepsilon} \hat{U}_{ji}\hat{t}_i \, d\Gamma = 0$$

and

$$\lim_{\varepsilon \to 0} \int_{\Gamma_\varepsilon} \hat{T}_{ji}\hat{u}_i \, d\Gamma = -\frac{1}{2}\hat{u}_j^k$$

where ε is the radius of the hemisphere over point k. The Somigliana's identity (4.12) can then be written for a boundary point as

$$\frac{1}{2}\hat{u}_j^k = \int_\Gamma \hat{U}_{ji}\hat{t}_i \, d\Gamma - \int_\Gamma \hat{T}_{ji}\hat{u}_i \, d\Gamma + \int_\Omega \hat{b}_i\hat{U}_{ji} \, d\Omega \qquad (4.13)$$

Equation (4.13) will now be applied on the boundary of the domain under consideration. For the wave propagation model, there are no body forces except at the excitation point, where $\hat{b}_i$ is a unit impulse function. Therefore, the last term of (4.13) becomes

$$\int_\Omega \hat{b}_i \hat{U}_{ji} \, d\Omega = (\hat{u}_0)_j^k \tag{4.14}$$

where $(\hat{u}_0)_j^k$ is theoretically the displacement at the excitation point (in the same direction as the excitation force) due to the virtual load at point k in j direction. Since both the excitation force and the virtual load are the same (unit point load), by the reciprocal theorem, $(\hat{u}_0)_j^k$ is also equal to the displacement at the point k in the j direction due to the excitation force.

The solution of the integral equation (4.13) can be done in a systematic way using numerical procedures by dividing the boundary Γ into n elements. In this work, the constant element is used (i.e., there is only one node at the center of each element). The displacements and tractions are assumed to be constant throughout each element and equal to the value at the mid-node.

By considering the discretized model as shown in Figure 4.2, and using Equation (4.14), Equation (4.13) can be written in discretized form for a given point k as

$$\frac{1}{2}\hat{u}_j^k = \sum_{\ell=1}^n \int_{\Gamma_\ell} \hat{U}_{ji} \, d\Gamma \, \{\hat{t}_\ell\}_i - \sum_{\ell=1}^n \int_{\Gamma_\ell} \hat{T}_{ji} \, d\Gamma \, \{\hat{u}_\ell\}_i + (\hat{u}_0)_j^k \tag{4.15}$$
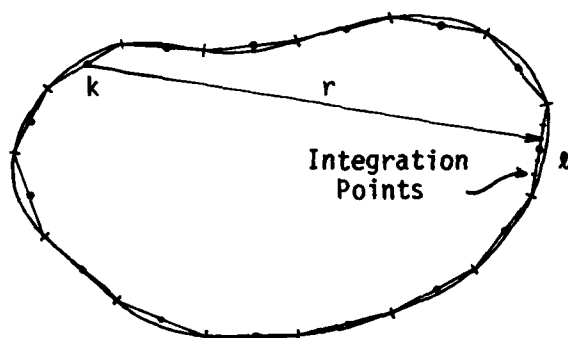
k: Nodal point under consideration where virtual load is applied

ℓ: Element over which the integration is carried out.

Figure 4.2 - Discretized Model

The above equation applies for a particular node k. Define the terms

$$\int_{\Gamma_\ell} \hat{U}_{ji} \ d\Gamma \ = \ [G_{k\ell}]_{ji}$$

$$\int_{\Gamma_\ell} \hat{T}_{ji} \ d\Gamma \ = \ [\bar{H}_{k\ell}]_{ji}$$

(4.16)

Both integrals above relate the k node with element ℓ over which the integral is carried out. Equation (4.15) can be rewritten as

$$\frac{1}{2}\hat{u}_j^k + \sum_{\ell=1}^{n} [\bar{H}_{k\ell}]_{ji}\{\hat{u}_\ell\}_i \ = \ \sum_{\ell=1}^{n} [G_{k\ell}]_{ji}\{\hat{t}_\ell\}_i + (\hat{u}_o)_j^k \qquad (4.17)$$

Equation (4.17) relates the value of $\hat{u}$ at mid-node k with the value of $\hat{u}$ and $\hat{t}$ at all the nodes on the boundary, including k. It can be written for each k node obtaining n equations. Let

$$H_{k\ell} \ = \ \bar{H}_{k\ell} \qquad\qquad \text{when } k \neq \ell$$

(4.18)

$$H_{k\ell} \ = \ \bar{H}_{k\ell} + \frac{1}{2} \qquad \text{when } k = \ell$$

Equation (4.17) can then be written as

$$\sum_{\ell=1}^{n} [H_{k\ell}]_{ji}\{\hat{u}_\ell\}_i \ = \ \sum_{\ell=1}^{n} [G_{k\ell}]_{ji}\{\hat{t}_\ell\}_i + (\hat{u}_o)_j^k \qquad (4.19)$$

The complete system of equations for the n nodes can be expressed in matrix form as

$$HU = GT + U_o \qquad (4.20)$$

where U and T are vectors with two (three for 3-D case) displacement and traction components for each of the n nodes. U_o is the vector of free field displacement components at each of the n nodes due to the unit excitation force and can be calculated directly from Equation (4.3). G and H are $2n \times 2n$ square matrices ($3n \times 3n$ for 3-D case) obtained by assembling the 2×2 submatrices (3×3 for 3-D case) that relate every two element nodes k and ℓ

Note that the matrices G and H are not symmetric and most of their elements differ from zero. In spite of these factors, the boundary element method is, in many cases, very efficient due to the much smaller number of unknowns. This is because the spatial dimension of the problem is reduced, and only the boundary of the region under study needs to be discretized.

4.1.2   Model for Inclusion

Equation (4.20) is formulated as a relationship between the displacements and the tractions at the boundary of the cavity in an infinite medium with a unit excitation force. In order to formulate the problems of wave propagation in an infinite medium with inclusions, a similar relationship is needed for each inclusion. The equations for the infinite medium and the inclusions are then combined from the equilibrium condition and the compatibility of displacements at interfaces.

36

The derivation of an equation like (4.20) for an inclusion fol-
lows the same procedure as in Section 4.1.1 except that there are no body
force terms in this case. By considering the model shown in Figure 4.1b,
starting with Equation (4.1), and neglecting the body force term in the
actual state, a system of equations that establishes a relation between
displacements and tractions over the surface of an inclusion is obtained
as

$$H_b U_b \;=\; G_b T_b \qquad\qquad (4.21)$$

All symbols in the equation above are as defined for Equation
(4.20), while the subscript 'b' indicates that they belong to an inclu-
sion.

It is worth noting here the distinctive structure of the bounda-
ry matrices (G and H matrices) for the cavity and for the inclusion. In
the boundary element formulation, the major difference between an inclu-
sion and a cavity is the direction of the outer normal vector η used in
the calculation of traction $\hat{T}_{ji}$ as shown in Equation (4.4). It can be
seen from Equation (4.16) that the calculation of the G matrix involves
the integration of the displacement $\hat{U}_{ji}$ which is independent of η; there-
fore, the matrix G (for soil with a cavity) and the matrix G_b (for an
inclusion) are identical provided that their surfaces, their elements,
and their properties are the same. In the same way, the H matrix is
obtained by integrating the traction $\hat{T}_{ji}$ which depends on the direction
of the outer normal η. Consequently, the matrix H (for soil with a cavi-

ty) and the matrix H_b (for an inclusion) will have the same value but opposite sign except for each diagonal elements of the matrix which are still the same and, for our case, equals to 1/2. In summary,

$$G = G_b$$

and

$$H = I - H_b$$

where I is an identity matrix.

4.1.3 Model for Wave Propagation in a Medium with Inclusions

A formulation for wave propagation in an infinite medium eith inclusions is derived by combining (4.20) and (4.21) under two conditions imposed at the interfaces of soil and inclusions. These two conditions are, first, that the tractions at interfaces must be in equilibrium, and second, that there is no separation between soil and inclusions at those interfaces. Both conditions imply that

$$T_b = -T$$

$$U_b = U \tag{4.22}$$

and

Equation (4.21) can be rewritten as

$$T_b = G_b^{-1} H_b U_b \tag{4.23}$$

By using (4.22), Equation (4.23) becomes

$$T = -G_b^{-1} H_b U \qquad (4.24)$$

Substituting (4.24) into (4.20) and rearranging, an equation is obtained that can be solved for the displacements at the surfaces of the inclusions

$$(H + GG_b^{-1}H_b)U = U_o \qquad (4.25)$$

In the above equation, $G_b^{-1}H_b$ belongs to each inclusion and has the same size as G and H if there is only one inclusion in the system. For the case of more than one inclusion, the matrix $G_b^{-1}H_b$ for each inclusion will be a submatrix along the diagonal of the global matrix because the inclusions cannot interact with each other except through the soil. The global matrix $G_b^{-1}H_b$ for the case of multiple inclusions is typified in Figure 4.3.

Once the displacements U at boundary are solved, the boundary tractions T can be calculated using Equation (4.24). The displacement at any point in the domain can then be computed using equation (4.12), which can be written for the displacement at any interior point k in discreatized form as

$$\hat{u}_j^k = \sum_{\ell=1}^{n} [G_{k\ell}]_{ji} \{\hat{t}_\ell\}_i - \sum_{\ell=1}^{n} [\bar{H}_{k\ell}]_{ji} \{\hat{u}_\ell\}_i + (\hat{u}_o)_j^k \qquad (4.26)$$
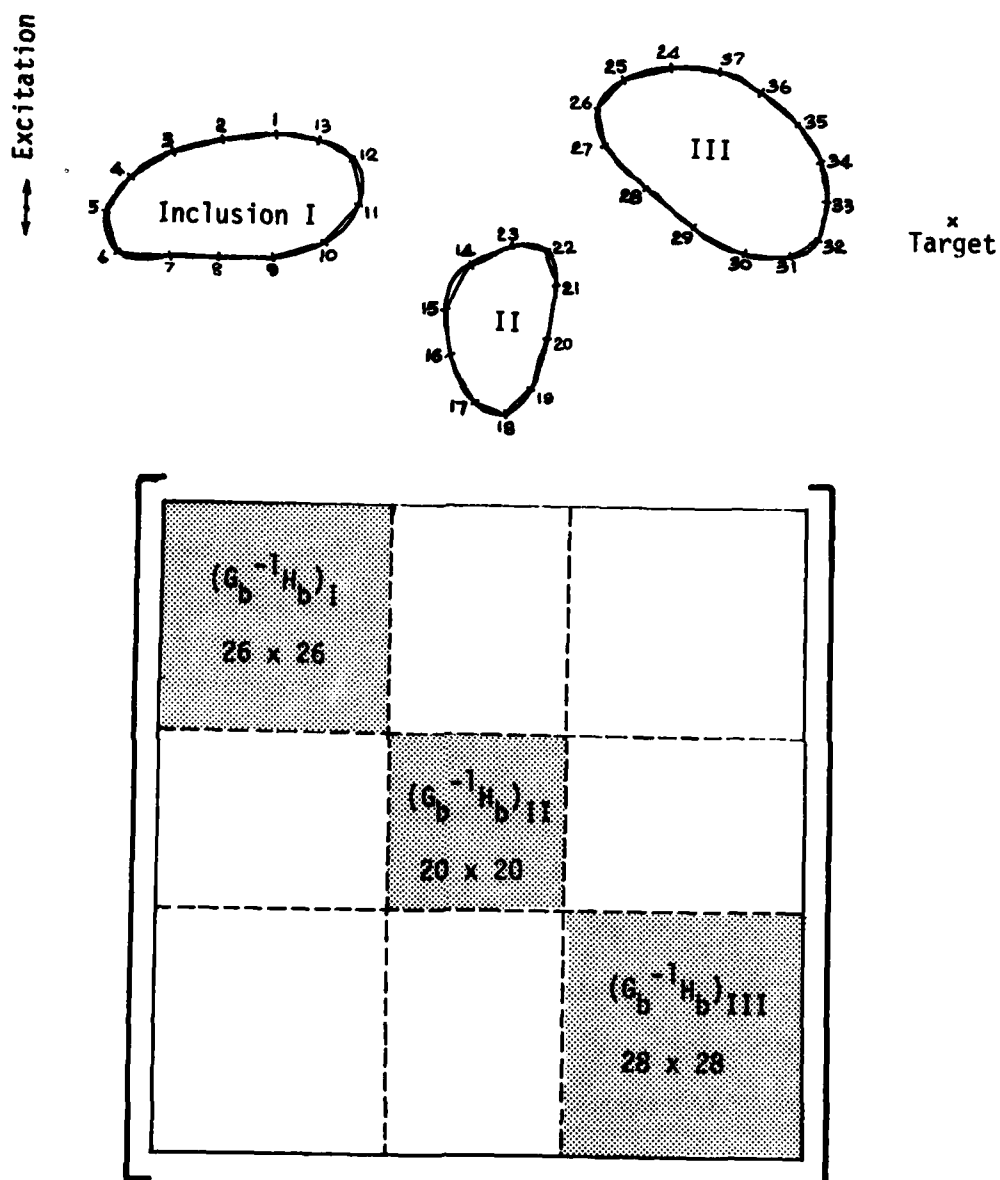
Figure 4.3 - Multi-Inclusion Model and Structure of Matrix $G_b^{-1}H_b$

In the above equation, $[G_{k\ell}]_{ji}$ and $[\bar{H}_{k\ell}]_{ji}$ are the integrals as defined in (4.16), but in this case they relate the interior point k with each mid-node on the boundary elements. $(\hat{u}_o)_j^k$ is the free field displacement component at the interior point k due to the excitation force, which can be readily calculated from (4.3). $\hat{u}_\ell$ and $\hat{t}_\ell$ are known boundary displacements and tractions that have already been computed from (4.25) and (4.24).

It should be noted that the final solution $\hat{u}_j^k$ resulting from (4.26) is only the frequency response for a unit concentrated harmonic excitation. It is also called a transfer function and has to be determined for several frequencies of excitation in order to get the time response from frequency domain analysis.

4.2 FREQUENCY DOMAIN ANALYSIS

The frequency domain approach involves expressing the applied loading in terms of harmonic components, evaluating the response of the system to each component, and then superimposing the harmonic responses to obtain the total response.

Any periodic function p(t) can be expressed in a Fourier series as

$$p(t) = \sum_{n=-\infty}^{\infty} c_n e^{(in\omega_1 t)} \qquad (4.27)$$

where

$$c_n = \frac{1}{T_p} \int_0^{T_p} p(t) \, e^{(-in\omega_1 t)} \, dt \qquad (4.28)$$

in which T_p is a period of the loading function, ω_1 is the fundamental frequency and n is an integer.

Defining $U(\omega)$ as a frequency response for a unit concentrated harmonic excitation, or a transfer function, it is possible to express the response of the system to each harmonic component of the loading function which represents each term of the Fourier series. Then, from the principle of superposition, the total response of the system to the forcing function $p(t)$ can be written as

$$u(t) = \sum_{n=-\infty}^{\infty} U(n\omega_1) \, c_n \, e^{(in\omega_1 t)}$$

A nonperiodic loading can also be represented by the Fourier series by considering that the loading function has a period T_p that extends to infinity. It is necessary to reformulate the Fourier series expression so that it extends over an infinite time range. Let

$$\frac{1}{T_p} = \frac{\omega_1}{2\pi} \equiv \frac{\Delta\omega}{2\pi}$$

$$n\omega_1 = n\Delta\omega \equiv \omega_n$$

$$c_n \equiv \frac{1}{T_p} c(\omega_n) = \frac{\Delta\omega}{2\pi} c(\omega_n)$$

With the above notation, the Fourier series (4.27) and (4.28) becomes

$$p(t) = \frac{\Delta\omega}{2\pi} \sum_{n=-\infty}^{\infty} c(\omega_n)\, e^{(i\omega_n t)} \tag{4.29}$$

$$c(\omega_n) = \int_{t=-T_p/2}^{t=T_p/2} p(t)\, e^{(-i\omega_n t)}\, dt \tag{4.30}$$

When $T_p \rightarrow \infty$, the frequency increment becomes an infinitesimal ($\Delta\omega \rightarrow d\omega$), and the discrete frequencies ω_n become a continuous variable ω. Therefore, the Fourier series (4.29) becomes the following Fourier integral

$$p(t) = \frac{1}{2\pi} \int_{\omega=-\infty}^{\infty} c(\omega)\, e^{(i\omega t)}\, d\omega \tag{4.31}$$

in which the harmonic amplitude function is given by

$$c(\omega) = \int_{t=-\infty}^{\infty} p(t)\, e^{(-i\omega t)}\, dt \tag{4.32}$$

The two integrals of (4.31) and (4.32) are known as a Fourier transform pair. Equation (4.31) is the representation of an arbitary loading as an infinite sum of harmonic components, where $(1/2\pi) \cdot c(\omega)$ defines the amplitude per unit ω of the load component at frequency ω. Multiplying (4.31) by the transfer function $U(\omega)$ yields the amplitude per unit ω of the response components at frequency ω. The total response can then be obtained by summing these response components over the entire frequency range, leading to the equation for the analysis of response through the frequency domain,

$$u(t) = \frac{1}{2\pi} \int_{\omega=-\infty}^{\infty} U(\omega) \, c(\omega) \, e^{(i\omega t)} \, d\omega \qquad (4.33)$$

In order to make a practical use of the frequency domain method described above, it is necessary to formulate the Fourier transform pair (4.31) and (4.32) so that they can be calculated numerically. A discrete Fourier transform (DFT) expression is, therefore, derived with the assumption that the input function is periodic of period T_p in order to replace the infinite time integral with the finite sum. The period T_p also serves to define the frequency increment and the lowest frequency that may be considered in the analysis, thus

$$\omega_1 = \Delta\omega = \frac{2\pi}{T_p}$$

and

$$n\omega_1 = n\Delta\omega = \omega_n, \quad n = 0, 1, 2, \ldots \ldots \qquad (4.34)$$

The loading function of period T_p is then divided into N equal time increments Δt, and the function is defined for each of the discrete times t_m, i.e.

$$t_m = m\Delta t, \quad m = 0, 1, 2, \ldots \ldots \ldots \qquad (4.35)$$

With (4.34) and (4.35), the exponential term in (4.29) becomes

$$e^{(i\omega_n t_m)} = e^{(in\Delta\omega m\Delta t)} = e^{(2\pi i \frac{nm}{N})}$$

and then, (4.29) takes the discrete form

$$p(t_m) = \frac{\Delta\omega}{2\pi} \sum_{n=0}^{N-1} c(\omega_n) \, e^{\left(2\pi i \frac{nm}{N}\right)} , \quad m = 0, 1, 2, \ldots, N-1 \qquad (4.36)$$

Accordingly, the discrete form for an amplitude function $c(\omega_n)$ is

$$c(\omega_n) = \Delta t \sum_{m=0}^{N-1} p(t_m) \, e^{\left(-2\pi i \frac{nm}{N}\right)} , \quad n = 0, 1, 2, \ldots, N-1 \qquad (4.37)$$

Equations (4.36) and (4.37) are the DFT pairs correspond to the continuous transform of (4.31) and (4.32). For the above DFT, the highest frequency to be considered is $(N-1).\Delta\omega$.

The fast Fourier transform (FFT) is an efficient method for evaluating DFT based on the numerical algorithm by Cooley and Tukey (1965). Basically, the FFT makes use of the harmonic nature of the exponential. By setting N to be a power of 2 (i.e., 2, 4, 8,....1024, 2048,..etc.) with integer 'm' and 'n' written in a binary form, the total computation and data storage is drastically reduced. There are many forms of FFT available which differ in the details of computer coding, and the one used in this work takes advantage of a complex conjugate symmetry. Thus, for the real input function of length N, the routine will return only half of the transform (from zero to highest frequency) as complex arrays of length (N/2)+1 and vice versa for the inverse FT.

In using the FFT, the values of basic parameters involved (number of sampling points N, time increment Δt and period T_p) have to be selected such that a compromise is reached between the accuracy of results and the cost of computations. These investigations will be presented in Chapter 5.

In summary, the frequency domain analysis can be obtained by:
(1) obtaining the Fourier transform of the loading function, (2) multi-
plying this Fourier transform by the transfer function of the system, and
(3) obtaining the inverse Fourier transform of the product to get the
response in the time domain.

4.3   NOTES ON COMPUTER IMPLEMENTATION

4.3.1   Integration

To form matrices G and H in the formulation in Section 4.1, the
integration of the *fundamental solution over the elements as defined in*
(4.16) needs to be carried out. The integration corresponding to the
node 'k' (where the virtual load is applied) and element 'ℓ' has no prob-
lem as long as k $\neq$ ℓ. The integration can be done numerically using a
four-point standard Gaussian quadrature integration (3×3 points are used
in the 3-D case). When the node 'k' belongs to element 'ℓ' (or k = ℓ),
numerical problems arise due to the presence of a singular point (at r =
0) in the integral domain. In this case, the integral $\bar{H}_{\ell\ell}$ is zero due to
the orthogonality of the normal 'n' and distant 'r'. The integral $G_{\ell\ell}$,
however, needs different treatment. In the three-dimensional case, a
series expansion of the exponential function was used and the integral
was computed analytically (Dominguez, 1978). In the two-dimensional

case, the numerical integration was still used, but the result is improved by introducing a correction.

The approach to compute the correction starts with the investigation of the function $\hat{U}_{ji}$ as shown in (4.3), which is expressed in terms of modified Bessel functions as in Equations (4.7) and (4.8). By expanding the modified Bessel functions $K_n(Z)$ into an infinite series (see Abramowitz and Stegun, 1965), the limit forms of these functions are taken as Z approaches zero (for this case, notes that $Z = i\omega r/c$, where c can be either c_s or c_p)

$$
\begin{align}
K_0(Z) &= -\ln(\tfrac{Z}{2}) - \gamma \\
K_1(Z) &= \frac{1}{Z} \\
\frac{1}{Z} K_1(Z) &= \frac{1}{Z^2} + \frac{1}{2} \ln(\tfrac{Z}{2}) \\
K_2(Z) &= \frac{2}{Z^2} - \frac{1}{2}
\end{align}
\tag{4.38}
$$

In the above expressions, γ is an Euler's constant which has no singularity problem in numerical integration and can be taken out. Using the relationship in (4.38), the limit form of ψ and χ as r approaches zero can be written as

$$
\psi = -\ln(\tfrac{1}{2} \frac{i\omega r}{c_s}) - \frac{1}{2} \ln(\tfrac{1}{2} \frac{i\omega r}{c_p})
\tag{4.39}
$$

$$
\chi = \frac{1}{2}[(c_s/c_p)^2 - 1]
\tag{4.40}
$$

From the above equation, it can be seen that, when $\hat{U}_{ji}$ is integrated numerically, the only term that contains errors due to singularity is $\psi\delta_{ij}$. Therefore, only G_{11} and G_{22} in the result need corrections. The correction which has to be added to G_{11} and G_{22} is the difference between integrating (4.39) analytically and numerically. The analytical integration of (4.39) can be written as

$$\int_{\Gamma} \psi \, d\Gamma = \int_{-\ell/2}^{\ell/2} \psi \, dr = \frac{\ell}{2} \left[\{1 - \ln(\frac{i\omega\ell}{4c_s})\} + \frac{c_s^2}{c_p^2} \{1 - \ln(\frac{i\omega\ell}{4c_p})\} \right] \quad (4.41)$$

in which ℓ is the length of the boundary element under consideration.

4.3.2   Direction of Normal and Node Arrangement

The problem studied involves formulations for both cavities and inclusions, which are the internal and external surfaces respectively. In both cases, the outer normal vector η, which is necessary in defining the direction of the tractions, is directed outward from the body. The sequences of nodal points k, ℓ in each element need to be defined in a manner consistent with the direction of the outer normal for that particular element. The numbering schemes for the 2-D and 3-D cases used in this study are shown in Figure 4.4. In the computer program, the input sequence of nodes are designed to follow the scheme for cavity. The computer program was written in such a way that when the formulation for inclusions is needed, it will reverse the nodal sequence temporarily so that the outer normal η will be in the opposite direction.

48
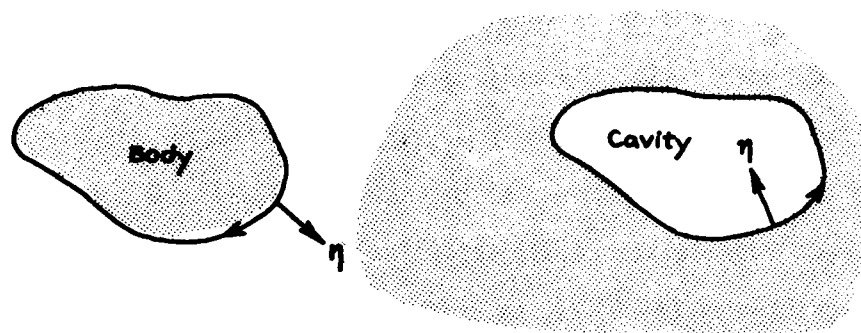
Two Dimensional Model
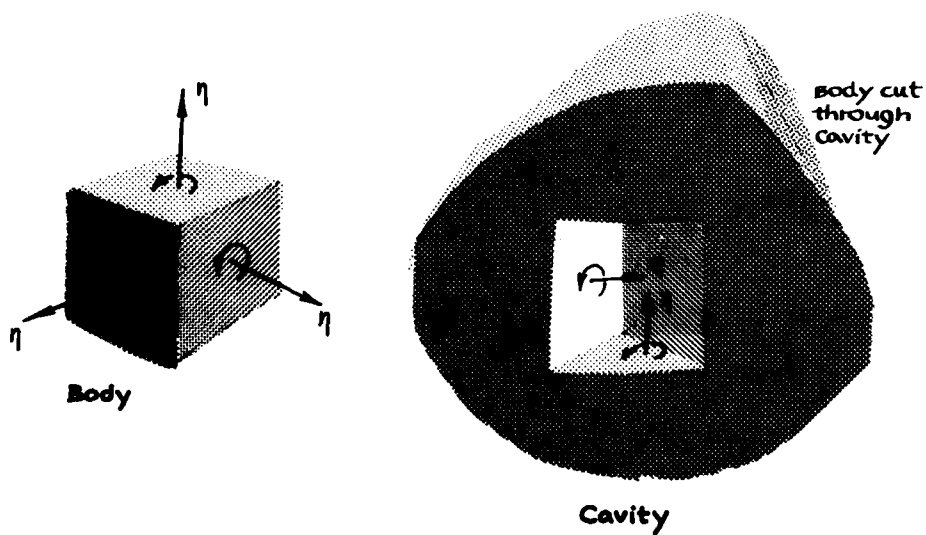
Three Dimensional Model

Figure 4.4 - Node Numbering Scheme for External and Internal Surfaces

4.4 DAMPING

The internal dissipation of energy in the soil is believed to be due to internal friction rather than to viscoelastic properties. Constant viscous damping produces an energy loss per cycle that increases linearly with frequency. A hysteretic damping, on the other hand, produces an energy loss per cycle that is frequency independent, but depends on the amplitude of the strains. Experimental evidence (Hardin, 1965) indicates that the second case is closer to the true behavior of soils. In order to maintain the linearity of the solution, the amplitude dependence is dropped, using what is normally called a linear hysteretic damping. In the frequency domain analysis, this type of damping is reproduced by assuming a complex modulus of the form $G(1+2iD)$, where D is the damping ratio. The terms corresponding to internal soil damping are then included in the complex stiffness matrix.

CHAPTER 5

PRELIMINARY INVESTIGATIONS

Since finite element and boundary element models are both discrete, the results are expected to deviate to some extent from the theoretical solution (if it is available) depending upon the nature of the model. The accuracy of the results can be improved by making the discrete model become as close as possible to the continuous one. This can usually be done by choosing a very small value of the discrete parameters such as time increment, size of element, etc. Of course, this approach is not always practical due to the computational costs. Therefore, it is necessary to investigate and choose a suitable value of these parameters so that a compromise is reached between accuracy and cost of computation.

In this chapter, only some of the important parameters involved in both finite element and boundary element formulations are investigated using a problem similar to one of those presented in Chapter 6. This is a case of free field wave propagation (no inclusions involved). The target is 4 ft. from the excitation point where one complete cycle of sinusoidal force is applied in a direction perpendicular to the principal axis of wave propagation, i.e., only a shear wave is considered. The frequency of excitation f_s is 100 cps. The medium has a shear wave

velocity of 100 fps, unit weight of 100 pcf, a Poisson's ratio of 0.25, and no material damping.

It had been mentioned in Suddhiprakarn (1983) that it is simpler and more reliable to interpret the results if the motions are presented in terms of a displacement rather than a velocity or an acceleration trace. Therefore, all results shown in this work will be in the form of displacement versus time. It should also be noted that, for this chapter, the results are still presented with units and dimensions. In the next chapters, the dimensionless form will be used.

5.1   FINITE ELEMENT

Because the appropriate value of the time step of integration used in the finite element model can be easily determined using the methods outlined in Section 3.4, they will not be discussed here. The only preliminary investigation needed for the finite element method in this work is to determine the size of the domain used in the model in order to represent properly an infinite medium.

Figure 5.1 shows the finite element model with the size expressed relative to the distance 'd' between the point of excitation 'A' and the target 'B'. In this case, the boundaries may have effects on the motion at both the excitation point and the target. There are three reflected waves involved in this case: the first one is a shear wave reflected from point 'D' at the left boundary passing 'A' to the target 'B', the second one is also a shear wave reflected from the right bounda-
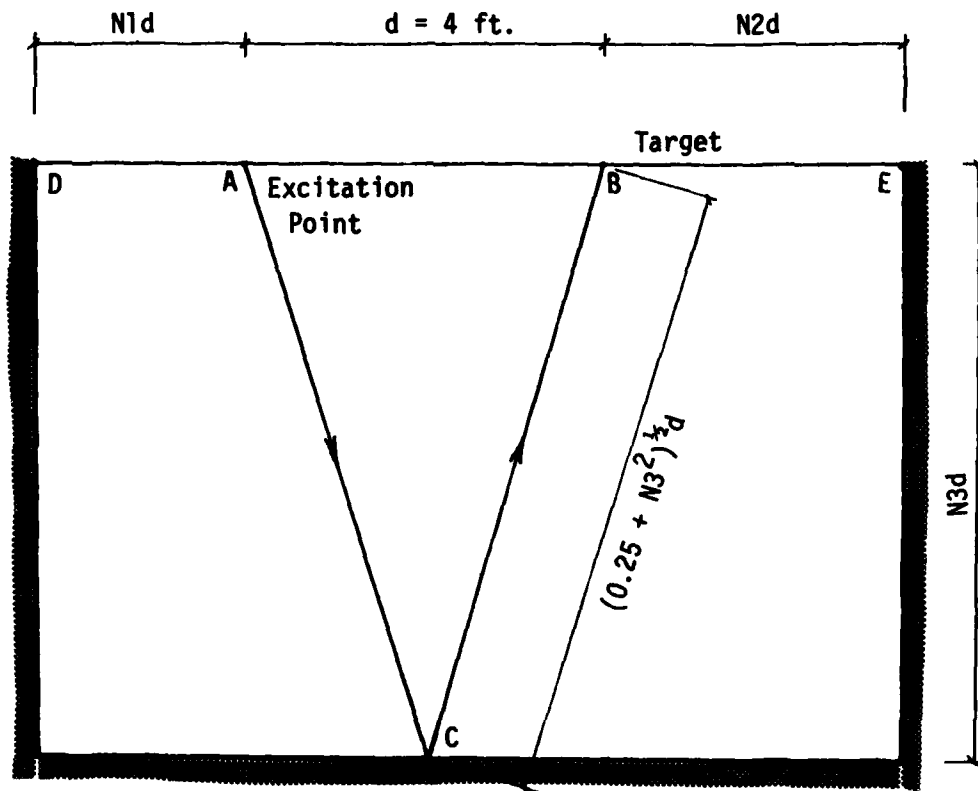
Soil Properties: $\nu = 0.25$

$\gamma = 100$ pcf

$c_s = 100$ fps

Frequency of Excitation = 100 Hz

Figure 5.1 - Finite Element Model Representing an Infinite Medium

ry at 'E' back to the target 'B', and the third one is a compression wave that takes the shortest route to the bottom boundary at point 'C' and reflects back to the target point 'B'.

Although the restraining effect and the reflected wave effects both happen together, it is possible to differentiate between them because the time involved in the travelling of reflected waves can be estimated. Once the arrival time of reflected waves is put beyond the time span of our interest, the difference in the results if any exists, will be caused solely by the restraining effects from the boundaries.

In this section, the effects from each boundary are investigated separately. By keeping the other two boundaries far away to ensure that they cause no effects, the boundary under consideration can be located in such a way that there is no further significant changes in the result when this boundary is moved away from the travelling path of the direct wave.

The effect from the left, right and bottom boundaries are shown in Figures 5.2, 5.3, and 5.4 respectively. In each figure, there are four separate plots of displacement versus time for different locations of the boundary under study. All notations related to the size of the domain (N1, N2, and N3 in this case) are defined in Figure 5.1. The theoretical arrival time for the plane shear wave, the compression wave, the reflected shear wave, and the reflected compression wave are denoted by the vertical lines marked S, P, SR, and PR respectively. In all results, there is an early motion occurring at the time of arrival of the com-
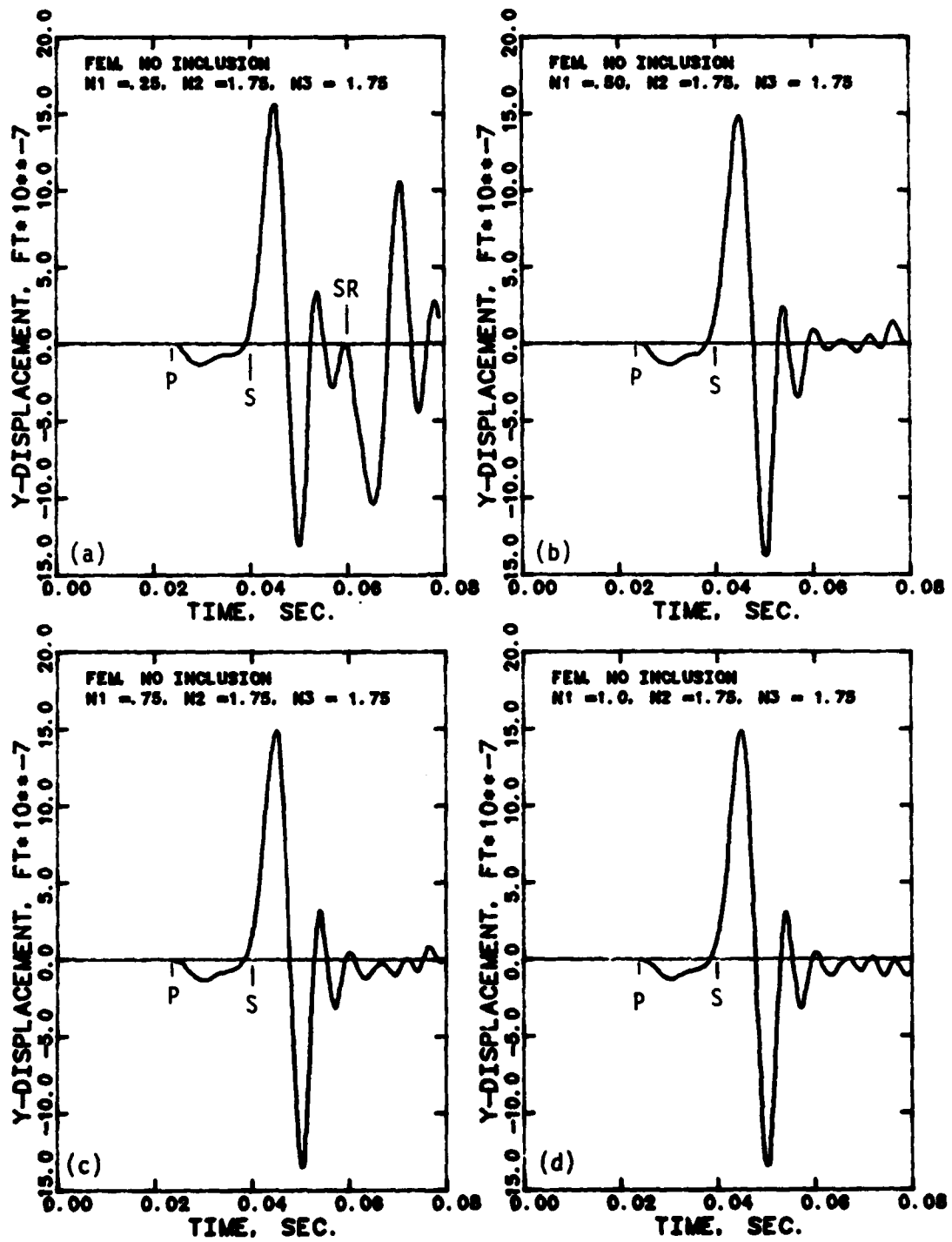
54

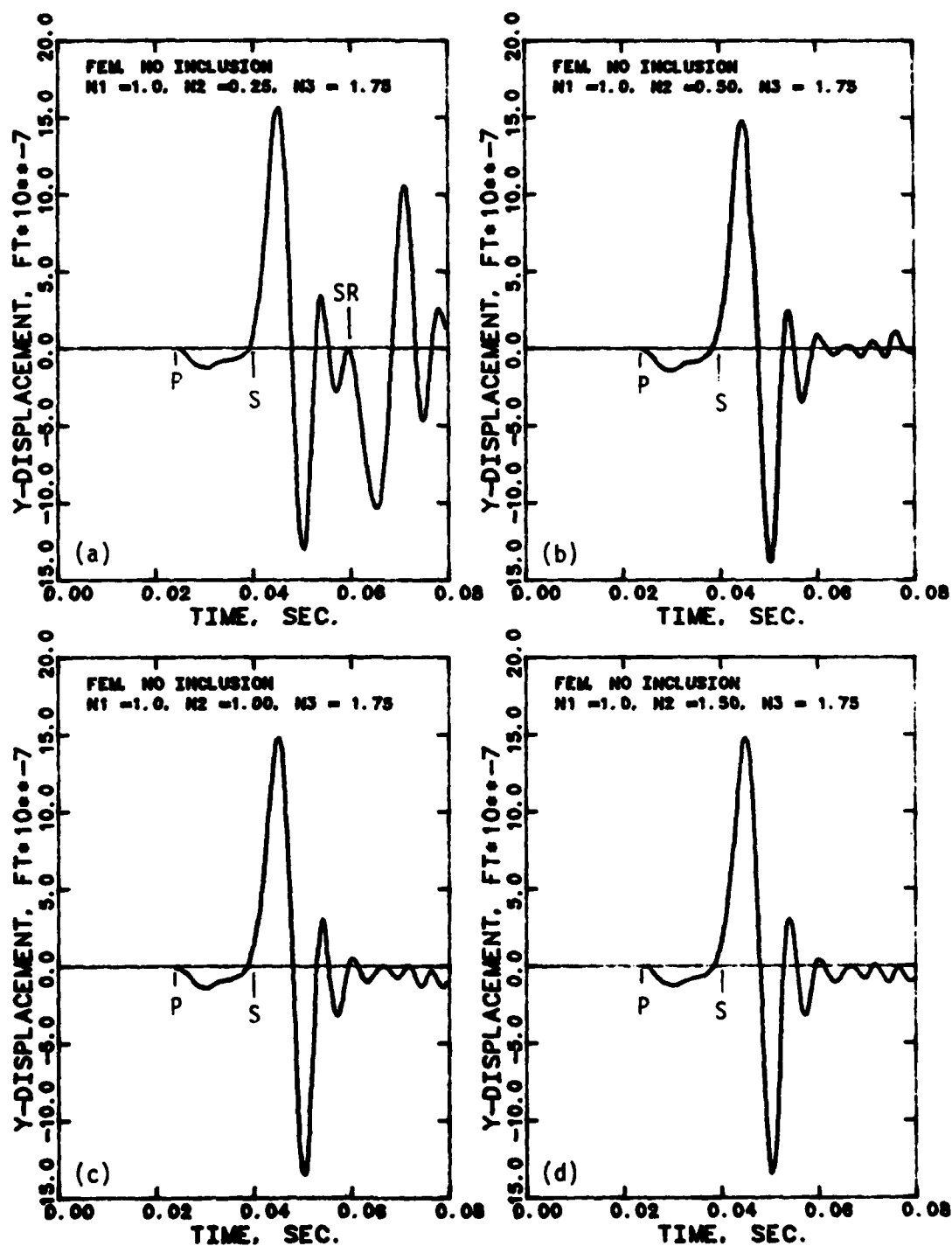Figure 5.2 - Effects of the Left Boundary on the FEM Result

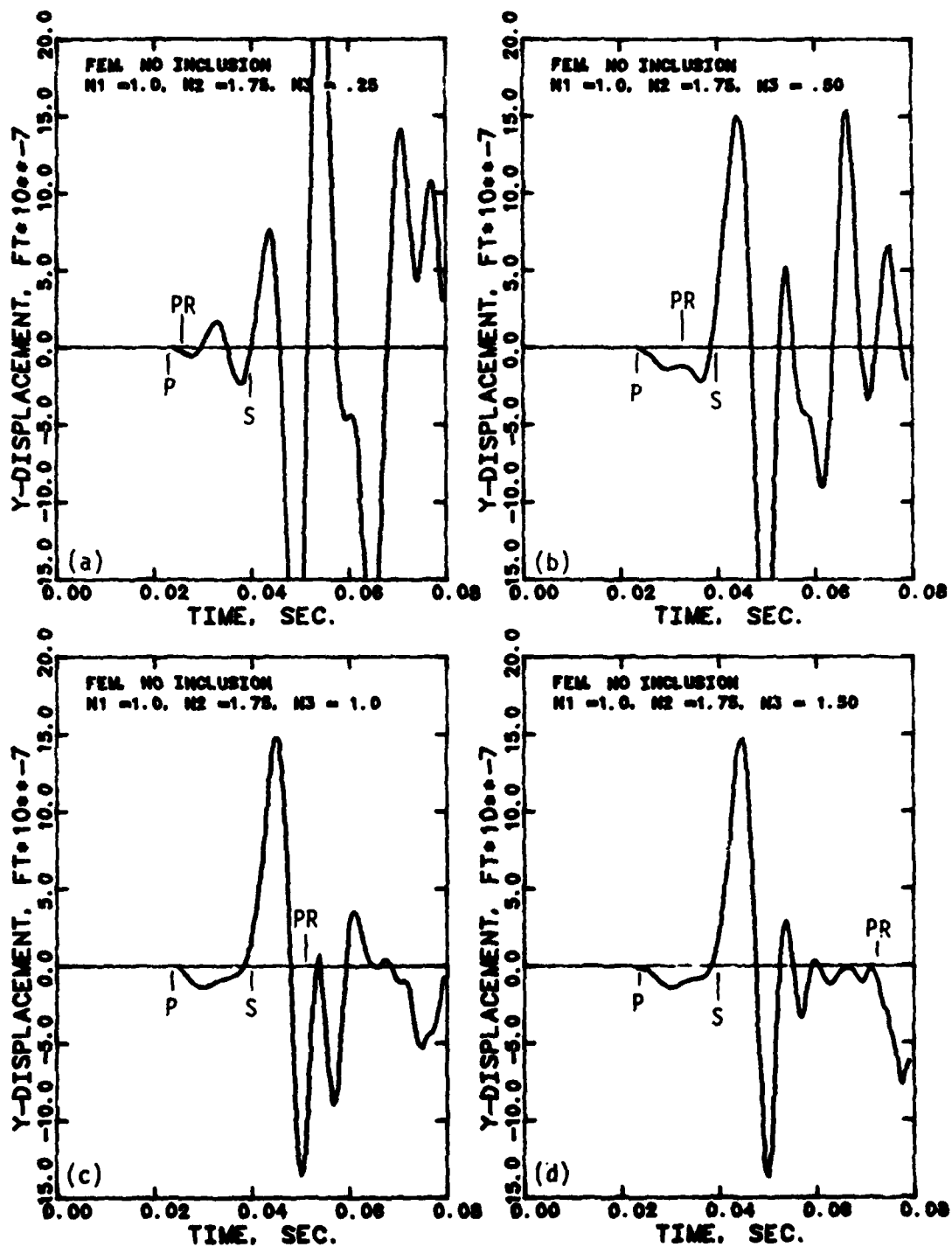Figure 5.3 - Effects of the Right Boundary on the FEM Result

56

Figure 5.4 - Effects of the Bottom Boundary on the FEM Result

pression wave which is due to the nature of the point force excitation (see Suddhiprakarn, 1983).

In Figure 5.2, the effects of the left boundary are investigated by seting N2 and N3 constant at 1.75. The results for the case N1 of 0.25, 0.50, 0.75, and 1.0 are shown in Figures 5.2a, 5.2b, 5.2c, and 5.2d respectively. The first thing to note is that the shapes of the displacement curves before the arrival of the reflected wave are the same for all four cases. The only difference is that the amplitude is slightly larger in the case when the left boundary is closer to the point of excitation, especially in the case N1 = 0.25. For N1 greater than 0.50, the amplitude remains constant.

In Figure 5.2a, the arrival of the shear wave reflected from the left boundary is evident by a starting downward motion of quite large amplitude. This is in contrast to the case of the direct wave which starts with an upward motion conforming to the excitation force. The opposite nature of the direct and reflected shear waves is reasonable if one considers the zero displacements at the fixed boundaries.

For N1 of 0.50 and higher as in Figures 5.2b, 5.2c, and 5.2d, the arrival time of the reflected shear wave is outside the time span presented and only the restraining effect from the boundary shows up. It is readily seen that, without the interference of the reflected wave, the motions of all three cases in Figures 5.2b to 5.2d is practically the same except that Figure 5.2b shows a slightly larger amplitude of the negative peak. In the cases of N1 = 0.75 and 1.00, the displacements are identical except for the decaying part of the motion after t = 0.06 sec.

which oscillates more uniformly in the case of N1 = 1.00. This motion could continue for a long time especially in a system without material damping like this one; therefore, it should not be a major factor in choosing N1 to be used as long as the significant part of the motion is accurate enough. For this case, the value of N1 = 1.00 seems to give a satisfactory result.

Using N1 = 1.00 and keeping N3 constant at 1.75, the effects of the right boundary can be studied in the same manner. The results for the cases N2 of 0.25, 0.50, 1.00, and 1.50 are shown in Figures 5.3a, 5.3b, 5.3c, and 5.3d respectively. The results from Figures 5.3a and 5.2a are almost identical, which shows that the shear waves reflected from the left and the right boundary have the same effects. By comparing Figure 5.3 with Figure 5.2, it is apparent that the effects of the right boundary show the same pattern discussed in the case of the left boundary. Figure 5.3c and Figure 5.3d, for N2 of 1.0 and 1.5 respectively, show very similar results except for the last cycle of the decaying portion which is considered unimportant. The further increase of N2 from 1.50 (as in Figure 5.3d) to 1.75 (as in Figure 5.2d) does not improve the results. From these results, it appears that the suitable value for N2 would range from 1.0 to 1.75.

In Figure 5.4, the effects of the lower boundary are investigated. This time the left and right boundaries are far away (N1 = 1.0, N2 = 1.75). Figures 5.4a, 5.4b, 5.4c, and 5.4d show the results for the cases of N3 equals to 0.25, 0.50, 1.0, and 1.50 respectively. In all four cases, the reflected compression waves arrive at the target within

the time span presented. This compression wave is also reflected from the top boundary which is not shown in Figure 5.1 since the model takes advantage of symmetry and antisymmetry as mentioned before. In Figure 5.4a where N3 is 0.25 (which means that the dimension N3.d in Figure 5.1 is the same as the wavelength), the motion is extremely complicated by the reflected compression wave which arrives even earlier than the direct shear wave. In Figure 5.4b where N3 is increased to 0.50, the reflected compression wave is still ahead of the direct shear wave but the motion in this case is slightly better. For N3 of 1.0 and 1.50 as shown in Figures 5.4c and 5.4d respectively, the reflected compression wave arrives after the direct shear wave and the motions are more accurate except after the arrival of the reflected compression wave which still affects the motion. The comparison of Figure 5.4d and Figure 5.2d, with N1 equals to 1.50 and 1.75 respectively, show that the motion before the arrival of the reflected compression wave is identical, and the same conclusion can also be drawn from Figures 5.4c and 5.4d. This indicates that the major factor to be considered on selecting the value of N3 is to keep the reflected compression waves beyond the time span of interest and for this case, a value of N3 of 1.75 would be appropriate.

In summary, to represent an infinite domain by the finite element model, as shown in Figure 5.1, the main consideration is to keep the reflected waves out of the time span under consideration. This is usually good enough for a bottom boundary (and a top boundary as well). For the right and left boundaries, they still need to be extended slightly farther so that the motion in the decaying zone remains practically the

same. For the case in this chapter, the value of N1, N2, and N3 of 1.0, 1.50, and 1.75, respectively, seem to be a good compromise between accurate results and minimum cost of computation.

5.2 BOUNDARY ELEMENT

The preliminary studies on the boundary element model presented in this chapter deal almost entirely with the parameters used for the fast Fourier transform except for the first subsection which discusses the methods to handle the problem of the transfer function at zero frequency.

5.2.1 Transfer Function at Zero Frequency

As mentioned in Chapter 4, in a frequency domain analysis, a solution or a transfer function has to be solved for different frequencies of a unit point excitation from zero to the highest frequency required in the fast Fourier transform. A problem arises when attempting to solve the displacements from the formulation shown in Equations (4.25) and (4.26) at zero frequency, because the term ϕ and x are singular at $\omega = 0$ as can be seen from Equations (4.5) to (4.8). This causes the Green's function $\hat{U}_{ji}$ and $\hat{T}_{ji}$ to be discontinuous at zero frequency.

Figure 5.5 is the typical shape of the transfer function versus frequency curve in our problem. The transfer functions plotted on the
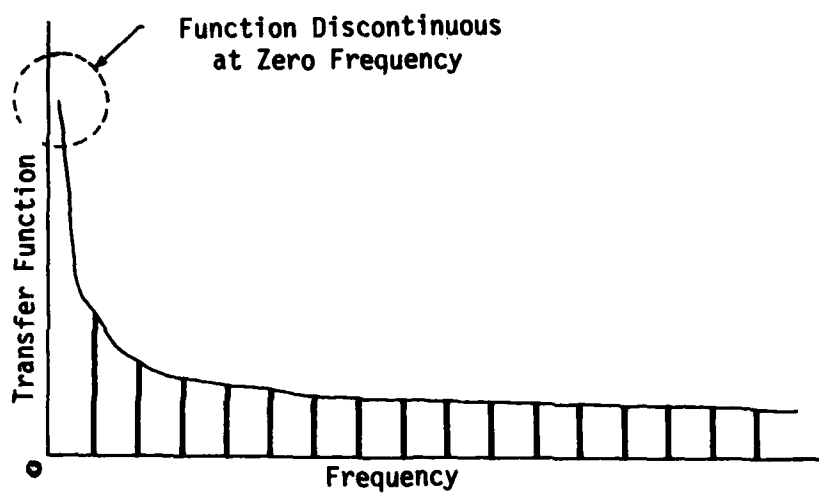
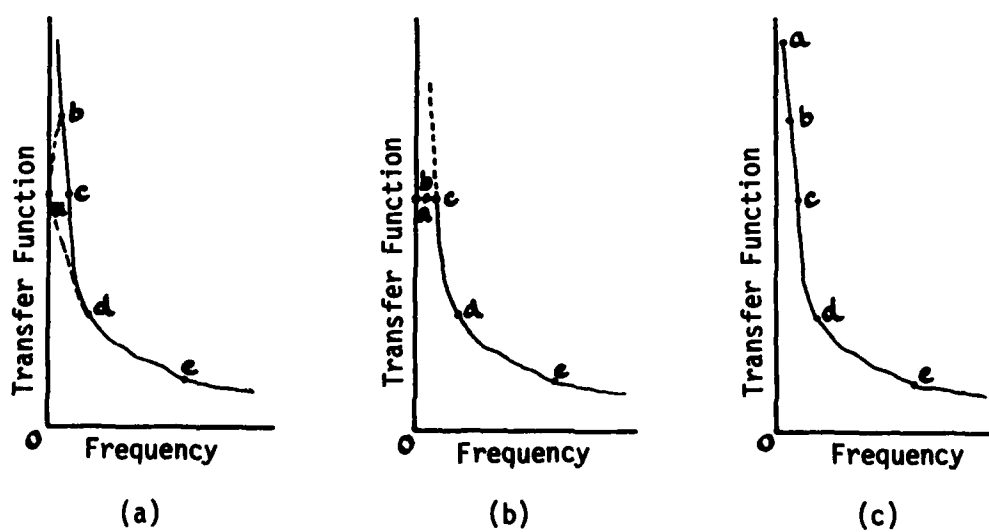Figure 5.5 - Typical Plot of Transfer Function versus Frequency

Figure 5.6 - Treatment of Transfer Function at Zero Frequency

y-axis are the absolute values since they are complex quantities. At large frequencies, the curve is almost horizontal, then it slopes up gradually when the frequency keeps decreasing. At small frequencies, the tranfer function increases rapidly and approaches infinity as the frequency approaches zero as shown in the figure.

Three methods were tried to handle this problem, and they are shown in Figure 5.6. The first case shown in Figure 5.6a is using the static solution at zero frequency instead of the dynamic solution as in Equations (4.3) and (4.4).

Since the dynamic solution does not approach the static one when the frequency approaches zero, the curve of the transfer function near zero frequency can have different shape depending upon the size of the frequency increment Δf. Two possible shapes are shown in Figure 5.6a as either 'ade' for large Δf, or 'abcde' for small Δf.

In the second case, the static solution is used as an upper bound as shown in Figure 5.6b. In this case, the shape of the transfer function curve is independent of Δf. In the third case, the dynamic solution is used throughout, but at zero frequency, an assumed value that is small relative to Δf is used instead of zero to avoid numerical problem. The transfer function in this case is also independent of Δf except that the starting point of the curve will depend on the value assumed for zero frequency.

The above three methods are compared by analysing the free field wave propagation problem. For the range of the Fast Fourier transform parameters that are going to be used in this work, the solutions from all

three approaches are identical and will not be presented here. The reason for these same results is that the transfer functions in all three cases only differ at a few points near a zero frequency. These few points, in spite of their large values, contribute very little to the Fourier transform.

If the first or the second method above is going to be used and the problems other than a free field case need to be analysed, the static solution has to be incorporated consistently into the different parts of the computer program, such as the calculation of the matrices G and H. This involves extra works which is unnecessary since the third approach seems to produce equally good results without any significant changes in the computer program. Therefore, the third approach will be used throughout this work.

5.2.2 Fast Fourier Transform Parameters

The basic concept of the Fourier transform and a frequency domain analysis were discussed in Section 4.2. The analysis in the frequency domain involves three basic steps: (1) Obtaining the Fourier transform of the loading function, (2) Multiplying this Fourier transform by the transfer function of the system, and (3) Obtaining the inverse Fourier transform of the results of step (2) to get the time response. The parameters involved in the fast Fourier transform (FFT) will be discussed by following these three logical steps.

In step (1), to obtain the FFT of a nonperiodic loading function, the period of this loading function, which is considered to be infinite in a classical Fourier transform, has to be assumed as a finite value T_p. The loading function used in this study is shown in Figure 5.7a. It is apparent that the loading function shown will represent exactly a single cycle sinusoidal force if the period T_p is extended to infinity. This is, of course, impossible numerically. In practice, however, it is acceptable to select a period T_p sufficiently large so that the effects of the spurious repetitive loading (shown as the dotted curve in Figure 5.7a) are negligible.

In FFT, this continuous loading function is, then, sampled at discrete time interval Δt throughout the period T_p as shown in Figure 5.7a. The total number 'N' of the sampling points and the time increment Δt will decide the value of the period T_p. Furthermore, they will also determine the frequency increment Δf, the maximum frequency f_{max}, and the number of frequency points N_f at which the transfer function has to be calculated. The relationship of these parameters can be written as

$$T_p = N \Delta t$$

$$\Delta f = \frac{1}{T_p}$$

$$f_{max} = \frac{1}{2\Delta t} \tag{5.1}$$

$$N_f = \frac{N}{2} + 1$$

$T_p = N \cdot \Delta t$

$\Delta f = \dfrac{1}{T_p}$

$f_{max} = \dfrac{1}{2\Delta t}$

$N_f = \dfrac{N}{2} + 1$
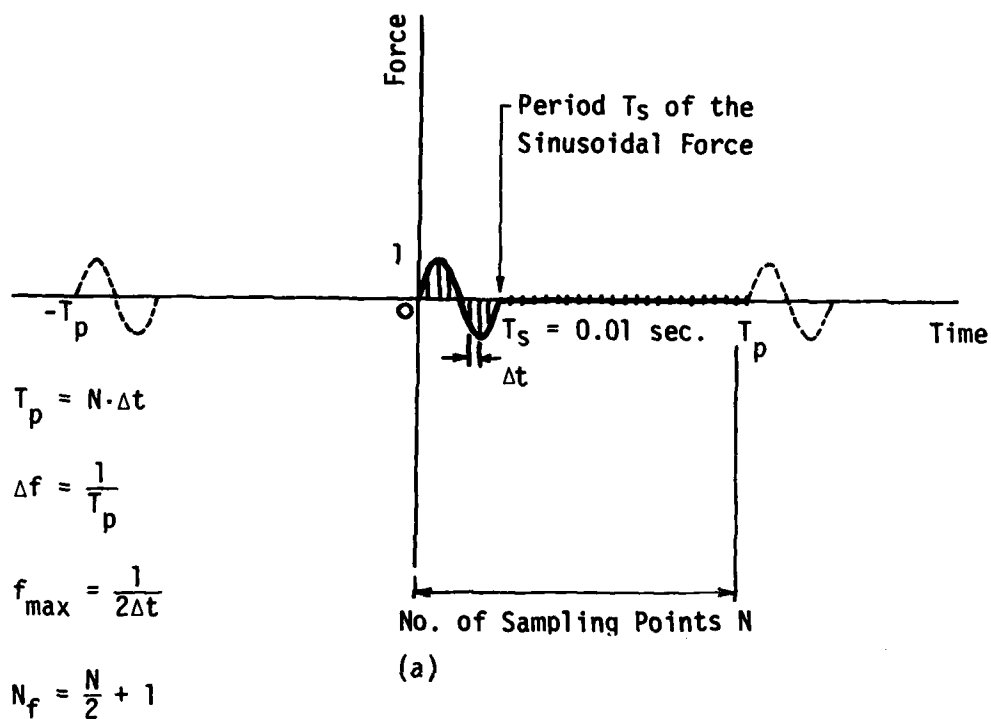
Effect of 'N'

N	Δt sec.	T_p sec.	T_p/T_s
1024		0.512	51.2
512	0.0005	0.256	25.6
256		0.128	12.8
128		0.064	6.4

(b)

Effect of 'Δt'

N	Δt sec.	T_p sec.	T_p/T_s
2048	.001	2.048	204.8
	.00025	0.512	51.2

(c)

Figure 5.7 - Parameters in Fast Fourier Transform

It should be noted that the number of sampling points N has to be a power of '2' as mentioned in Section 4.2 for the FFT algorithm.

It can be seen from the expressions above that the fundamental parameters involved are only N and Δt from which the other parameters can be obtained. Therefore, investigations will be made first for N and Δt.

(a) Effects of N Different values of N shown in Figure 5.7b are used with the value of Δt fixed at 0.0005 seconds. The period T_p for each case relative to the period T_s of the sinusoidal part of the loading function are also tabulated. The results for each value of N are shown in Figures 5.8a to 5.8d. In Figures 5.8a and 5.8b where N is 1024 and 512 respectively, there is no difference in the results. When N is reduced to 256 as in Figure 5.8c (where T_p/T_s is now 12.8), the positive and negative peaks are still the same as in the first two figures but the beginning part of the curve starts to show a very small negative value instead of zero. It indicates that the period T_p is not large enough, and consequently, the effects of the repetitive loading (shown as a dotted curve on the left in Figure 5.7a) become significant. The result, however, is still acceptable unlike the case of N = 128 shown in Figure 5.8d in which the beginning part of the curve shows larger deviations from zero (even though the other part of t..e result, still, seems to be satisfactory).

Figure 5.8d also shows that the curve terminates before the end of the time scale; therefore, the time span under study has to be considered as well in choosing the value of N and Δt.
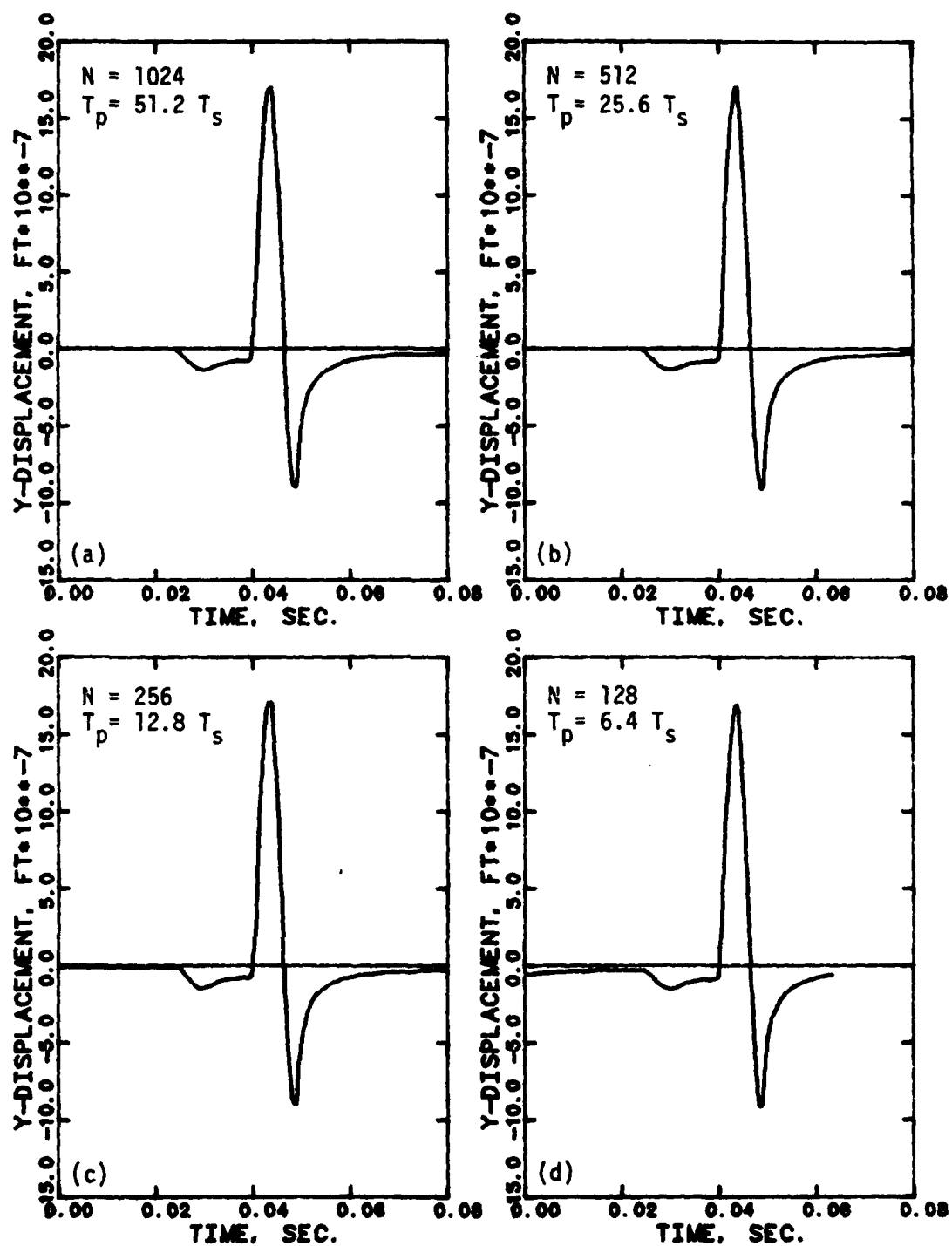
Figure 5.8 - Effects of the Number of Sampling Point 'N'

All in all, when the number of the sampling points N decreases such that the period T_p is closer to the period T_s of the sinusoidal part of the loading function, the effects of the repetitive loading start to show up. In other words, the quiet duration between point T_s and T_p in Figure 5.7a has to be long enough so that the transient part from the previous loading cycle completely disappears.

Studies were also conducted for the case of closer distances between the excitation point and the target, and different period T_s. The results, though not presented here, show that acceptable accuracy is obtained if the ratio T_p/T_s is not lower than a value of about 10.

(b) Effect of Δt Different values of Δt are investigated with the value of N fixed at 2048. The only two cases presented are tabulated in Figure 5.7c together with the corresponding values of T_p. In both cases, the period T_p is long enough so that no transient from the previous cycle appears. The results for the case Δt of 0.00025 seconds and 0.001 seconds are shown in Figures 5.9a and 5.9b respectively. The general shape of the curve is pretty much the same in both cases except that for the larger Δt, the resolution of the curve may not be sufficient to reproduce some sharp peaks as shown in Figure 5.9b.

Up to this point, the only conclusions that can be drawn about the selection of Δt is that it should be sufficiently small in order to get smooth results. In addition, a small value of Δt is also necessary to reproduce accurately the loading function. On the other hand, Δt
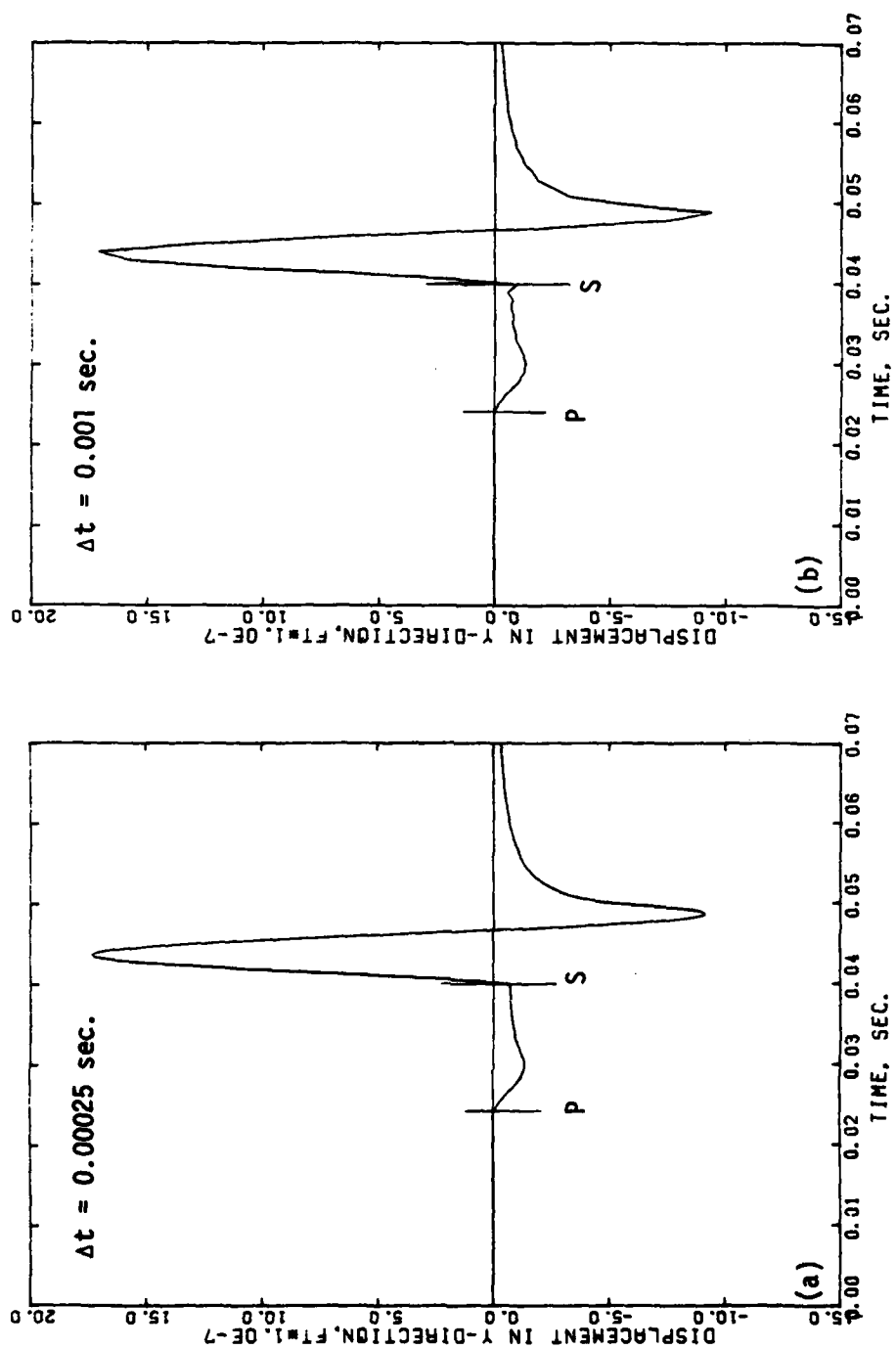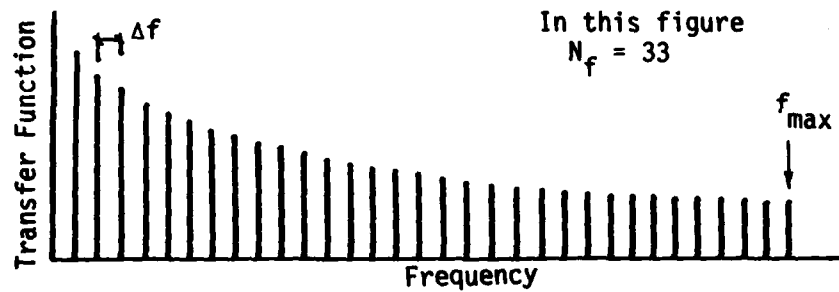
Figure 5.9 - Effects of the Time Increment Δt

should not be so small that it reduces the value of the period T_p causing the transient to show up again.
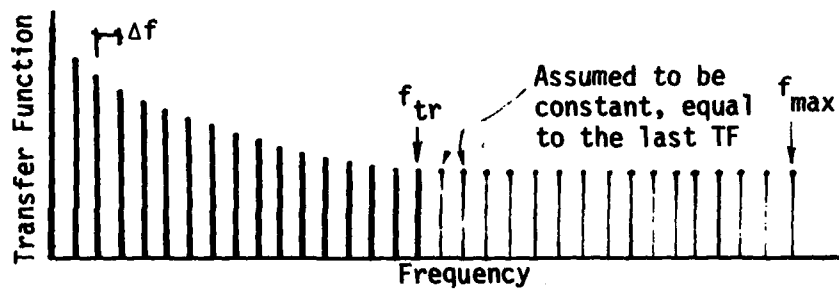
In step (1), the N points sampled from the loading function are real quantities in the time domain. After taking a Fourier transform, the results consist of N_f complex quantities in the frequency domain, from zero to the highest frequency f_{max}, with an increment of Δf. In step (2), each of these complex points is then multiplied by the values of the transfer function determined at each corresponding frequency.

Since the calculation of the transfer function is time consuming especially for the case with inclusions, it is usually not possible to compute the transfer function at every required frequency if the computation cost has to be kept within a practical limit. Normally, only some of the values of the transfer function need to be calculated while the remaining ones can be defined in different way depending on the procedure used. In this study, two procedures: truncation, and interpolation are investigated. Both procedures involve the parameters f_{max}, Δf, and N_f shown in Equation (5.1).

(c) **Effects of truncation** Figure 5.10a shows typical transfer functions at each frequency increment Δf, from zero to the highest frequency f_{max}. In the truncation procedure, the transfer functions are calculated at each frequency increment Δf up to the truncated frequency f_{tr}, beyond which they are assumed to be constant for case 1, and are defined as zero for case 2, as shown in Figures 5.10b and 5.10c respectively.
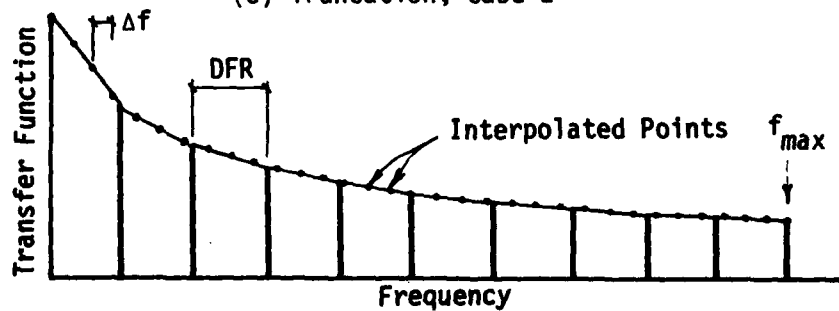
Transfer Function

Δf

In this figure
$N_f = 33$

f_{max}

Frequency

(a) All Points Calculated

Transfer Function

Δf

f_{tr}

Assumed to be
constant, equal
to the last TF

f_{max}

Frequency

(b) Truncation, Case 1

Transfer Function

Δf

f_{tr}

f_{max}

Frequency

(c) Truncation, Case 2

Transfer Function

Δf

DFR

Interpolated Points

f_{max}

Frequency
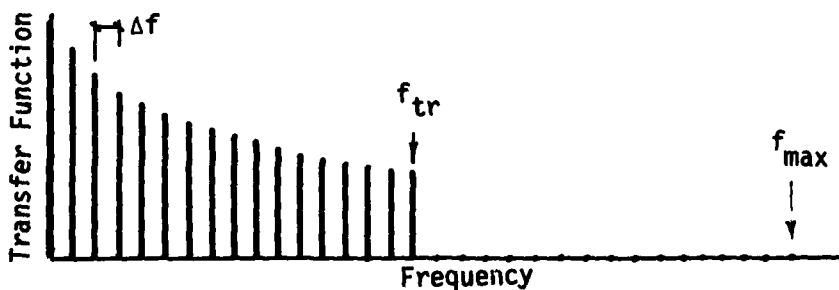
(d) Interpolation

Figure 5.10 - Truncations and Interpolation of the
Transfer Function

Using the truncation procedure case 1, the results for different value of f_{tr} are shown in Figures 5.11a to 5.11d. In each case, the relative value of f_{tr} with respect to f_{max} and f_s (the frequency of the sinusoidal part of the loading function) are also shown. In Figure 5.10a, the transfer functions are calculated at every point without any truncation, resulting in a very smooth curve. In Figure 5.11b where f_{tr} equals $1/2f_{max}$ $(5f_s)$, there are some noticeable vibrations at the beginning of the curve and the overall result is slightly less smooth than in Figure 5.11a; however, the result is still acceptable. In Figure 5.11c, where f_{tr} equals $1/4f_{max}$ (and $2.5f_s$), many irregularities are apparent although the peak value is still accurate. In Figure 5.11d, the results for two different values of f_{tr} are plotted together, the solid curve corresponding to $f_{tr} = 1/8f_{max}$ and the dotted curve to $1/16f_{max}$. In both cases the curves are extremely irregular and the results lack sufficient accuracy.

The corresponding set of results using the truncation procedure case 2 are shown in Figure 5.12. As before, Figure 5.12a shows the result without any truncation just for comparison. By comparing the results between the truncation case 1 and case 2 for each corresponding value of f_{tr}, it is apparent that the results from both cases are the same except the beginning part of the curve which is now flatter in the truncation case 2, even when f_{tr} is as low as $1/4f_{max}$ (Figure 5.12c). In Figure 5.12d, even though the high frequency components are not enough to produce accurate results, the curves still show more uniform motions at the beginning part comparing with those of Figure 5.11d.
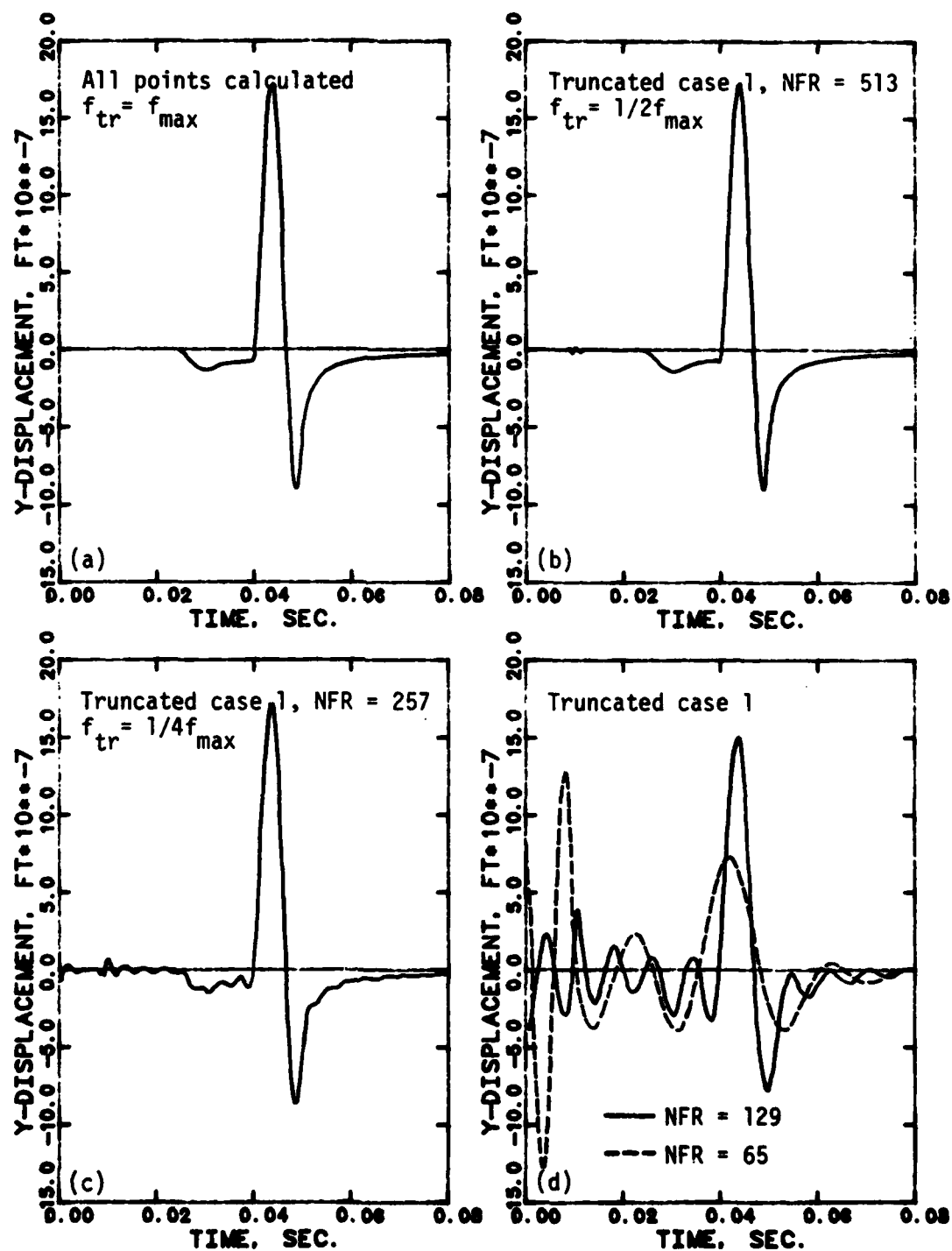
Figure 5.11 - Effects of Truncation, Case 1
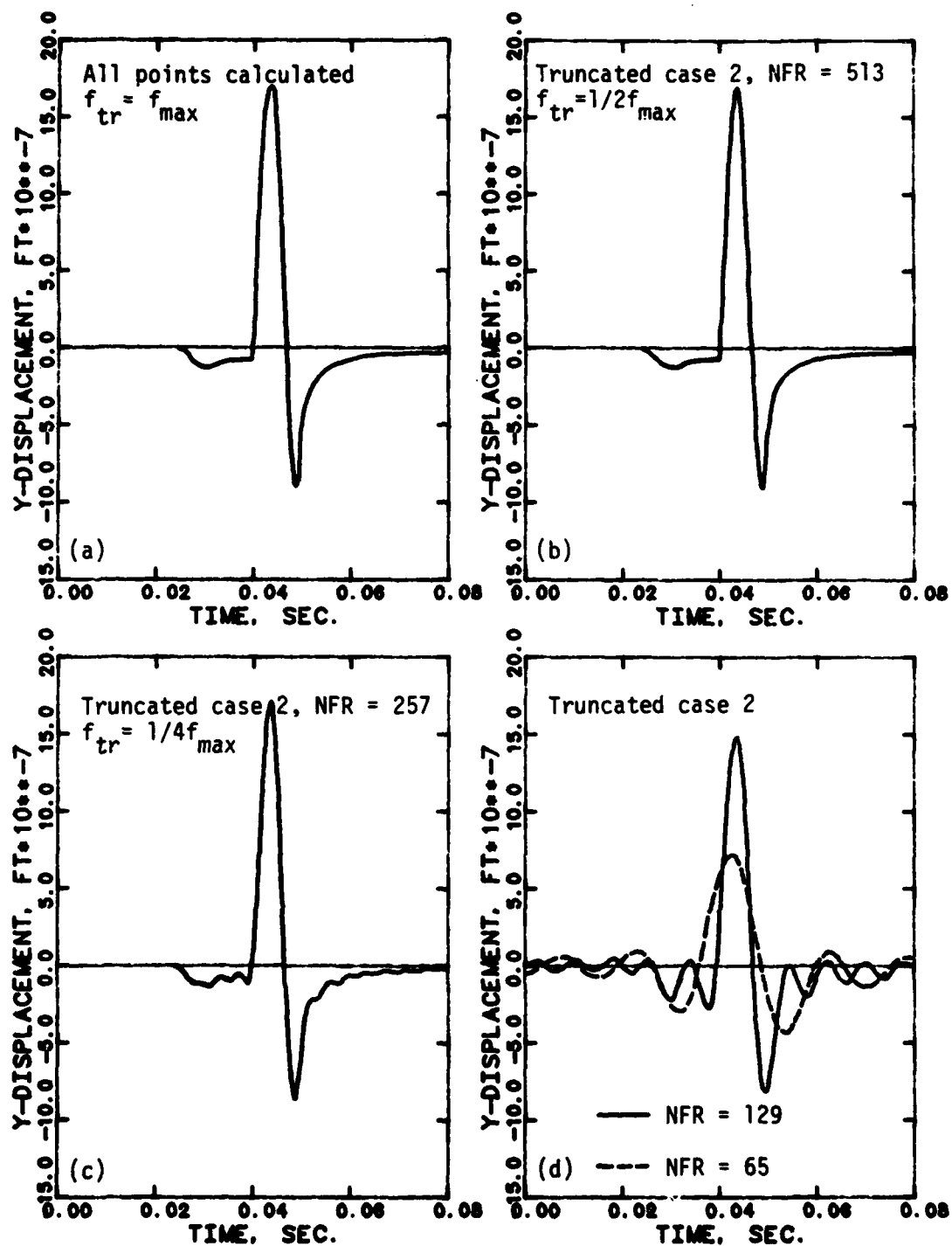
74

Figure 5.12 - Effects of Truncation, Case 2

The results of these studies indicate that to obtain a reasonable accuracy, making zero the transfer functions after f_{tr} would be a better choice than assuming constant values. When the calculated transfer functions are used, the results (Figure 5.12) indicate that the transfer functions at higher frequencies have small effects on the results. The frequency beyond which transfer functions become less effective is believed to be related to the frequency of the sinusoidal excitation f_s, and this was confirmed by further studies not shown here using different values of f_s and f_{tr}. All these studies show that the result will be accurate enough as long as f_{tr} is more than five times f_s.

(d) Effects of Interpolation The interpolation procedure, represented graphically in Figure 5.10d, involves the calculation of the transfer functions from zero to the highest frequency, but at a frequency increment different from Δf defined in Equation (5.1). The frequency increment used in the interpolation method, denoted as 'DFR', is arbitrarily chosen, larger than Δf, and not necessarily a multiple of Δf; therefore, the number of frequencies at which the transfer functions are calculated (NFR) is less than N_f and these frequencies may not coincide with the frequencies where the transfer functions are required. The transfer function at each required frequency is determined using a linear interpolation as shown in Figure 5.10d.

Different combinations of the number of frequencies NFR and the frequency increment DFR were investigated. All combinations were chosen such as to cover the complete range of frequencies from zero to f_{max}, and

the results are shown in Figures 5.13a to 5.13d. In Figure 5.13a when NFR in 1001 and DFR is 1, the results are almost the same as in the case of Figure 5.12a where no truncation is used; therefore, both results are smooth with a slightly lower peak in the case of Figure 5.13a. When DFR increases to 2, and NFR is reduced to 501 as in Figure 5.13b, the shape of the curve is the same but the peak is lower. This decrease in the peak amplitude is more pronounced when less interpolation points are used as evidenced in Figures 5.13c and 5.13d. In the latter figure, the shape of the curves is also badly deformed.

Although the shapes of the displacement curves in the case of interpolation are almost the same throughout (except when DFR is large), the amplitude of the peak is reduced in comparison to the results from the truncation procedure that use a comparable number of points for the calculation of the transfer function (see Figures 5.13b and 5.12b for example). It appears ,therefore, that truncation of the transfer function provides, for the same computational effort, a better solution than interpolation.

5.2.3   Summary on Parameters of the Frequency Domain Analysis

For the frequency domain analysis to be useful, the mumber of points at which the transfer function is calculated should be within the range of 100 to 200 in order to maintain the cost of computation as low as possible. The method of truncation case 2 seems to be the best method
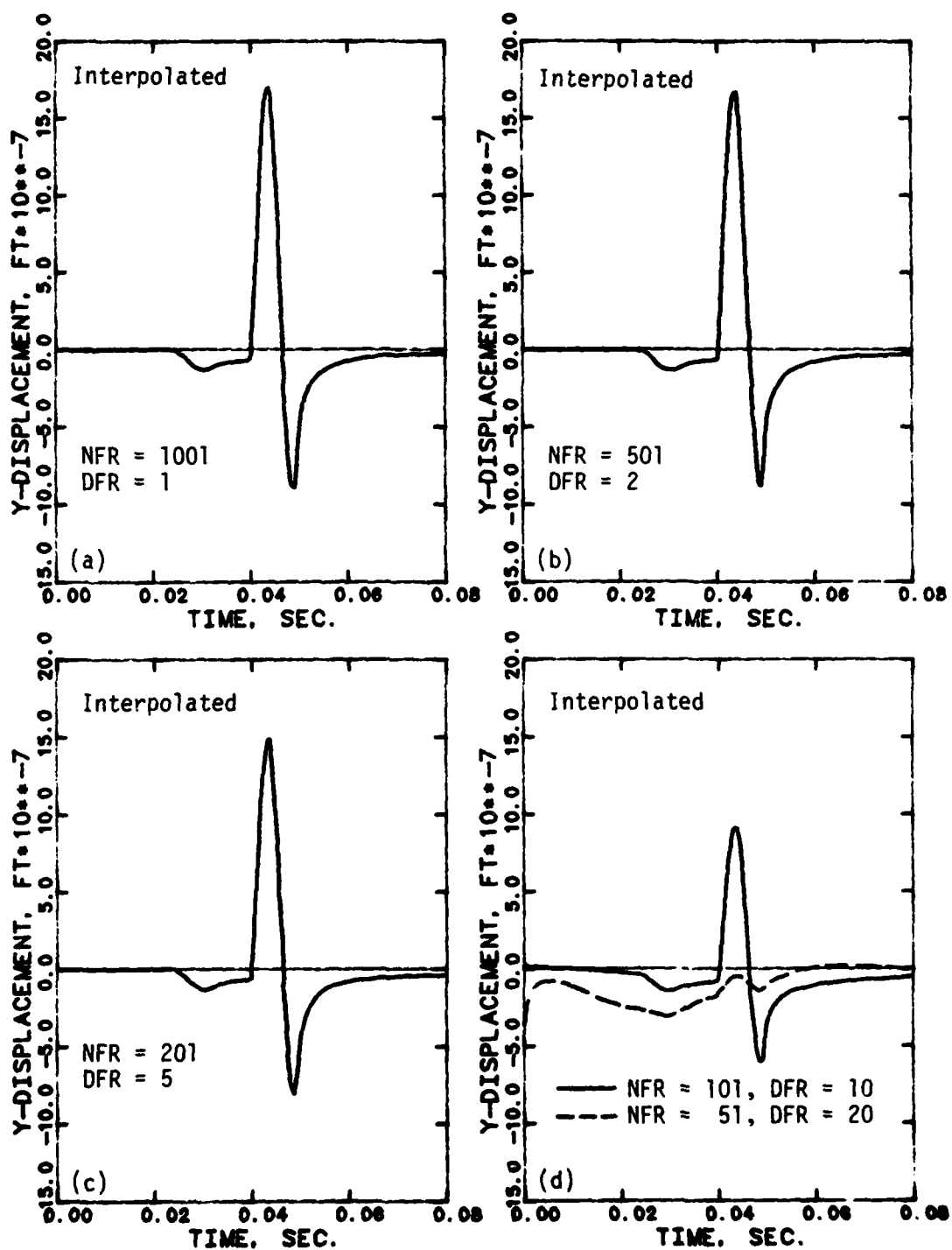
Figure 5.13 - Effects of Interpolation

1.0

1.1

1.25

2.8

3.2

3.6

4.0

2.5

2.2

2.0

1.8

1.4

1.6
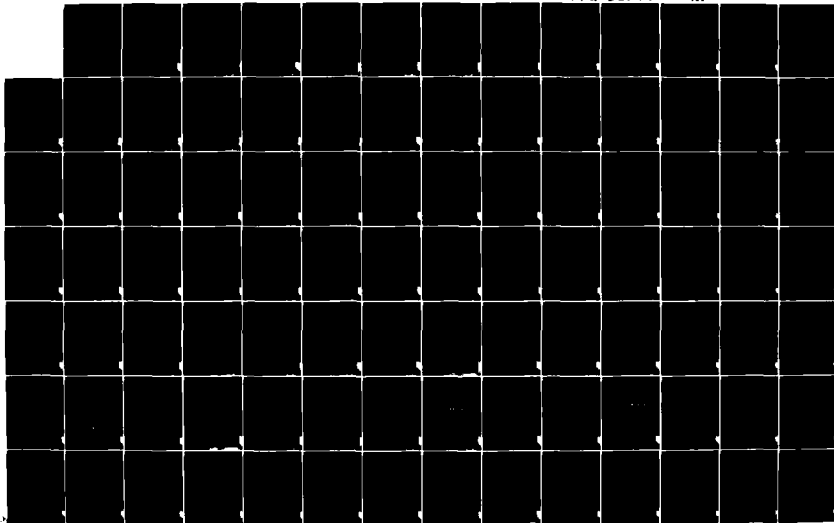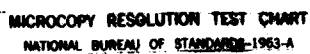
MICROCOPY RESOLUTION TEST CHART
NATIONAL BUREAU OF STANDARDS-1963-A

to keep the number of points within this range without sacrificing the accuracy of the results.

From the above considerations, the following conclusion can be drawn

1. At zero frequency, where a singularity problem occurs, it is easier and more consistent to compute the transfer function at a very small frequency instead of using the correct static values.

2. The truncation method case 2 proves to be the most efficient way to reduce the number of the transfer functions that need to be calculated.

3. The time increment Δt should be small enough to give smooth results with well-defined peaks, and to reproduce accurately the loading function.

4. The combination of Δt and the number of sampling points N should result in a period T_p that is long enough to provide sufficient quiet duration beyond the sinusoidal part of the loading function so that the effects of the repetitive loading disappear. The period T_p should be more than ten times T_s (the period of the sinusoidal part of the loading function). In addition, the combination of Δt and N should produce a total time long enough to cover the time span of interest.

5. The truncated frequency f_{tr} should be selected such that there are
    enough high frequency components in the Fourier transform to
    reproduce the wave frequency. For this study, f_{tr} should be more
    than five times f_s the frequency of the sinusoidal part of the load-
    ing function.

These preliminary studies were intended to determine the effect
of various parameters on the accuracy of the frequency domain solution
using the FFT. Two additional points that must be considered are the
distance from the excitation to the target, and the size of the boundary
elements. Clearly if one wants to determine the time of arrival of the
first wave at the target with an error less than n percent, the time step
Δt should not be larger than $(n/100).d/c$ where d is the distance, and c
the wave propagatio. velocity. To reproduce properly the transfer func-
tion at a frequency f, the size of the boundary elements, similarly to
the part made for the finite element mesh, should not be larger than $\lambda/4$
to $\lambda/8$ where λ is the wavelength c/f.

CHAPTER 6

EFFECT OF AN INCLUSION ON ATTENUATION

The studies of wave attenuation were performed by observing the peak amplitude and the shape of the displacement versus time curve at various distances from the point of excitation. Analyses were made (both in two and three dimensions) for the case with inclusions. For the boundary element model developed in this work, all four physical properties of soil and inclusions--which are shear wave velocity, mass density, Poisson's ratio, and damping ratio--can be varied in any combination as required. By approximating the curved surface with several straight elements, different shapes and sizes of inclusions can be modeled with sufficient accuracy. In addition, the cluster of inclusions can be arranged in any configuration. The only limitation is in the total number of boundary elements due to the size of the resulting matrix that can be handled in core by the computer.

The possible combination of the parameters involved is so large that a complete parametric study is virtually impossible. Only a few typical cases for the shear wave will, therefore, be studied in this work. In this chapter, results of comparative studies between the free field case and the case with a square inclusion (a cube for the

three-dimensional case) having different sizes in relation to the wavelength λ. In each case, different values of soil damping are used.

As presented in Stokoe et al (1980), the finite element method (FEM) was implemented for the wave propagation problem in the triaxial cube containing soil and rigid inclusions, The method is more appropriate because of the finite domain, while the boundary element method (BEM), on account of a need to discretize the outer surface of the cube as well, is very expensive for that particular problem. On the other hand, for an infinite medium as in this work, the FEM is not as economic and flexible as the BEM; therefore, it is used only to compare the results it provides with those of the boundary element solution. The comparison of results is presented in the first section of this chapter with all results involving the attenuation of the shear wave in the free field.

All results are presented in dimensionless form. The notation, unless defined where it is used, will be shown in the list of symbols. The most frequently used forms are a dimensionless displacement uG/F and a dimensionless time $c_s t/d$, where u is the displacement at the target, G is the shear modulus of the soil, F is the peak amplitude of the excitation (force per unit length for the 2-D case), c_s is the shear wave velocity of the soil, t is the elapsed time, and d is the distance between the source and the target. In this way, the theoretical time of arrival of the shear wave in the free field corresponds to a value of one.

6.1 FREE FIELD ATTENUATION

Due to the limited capability of the finite element model, comparison of the results from the FEM and the BEM can be made only for the two dimensional case without material damping as will be presented in the following subsection.

6.1.1 Two-Dimensional Case with the FEM Results

The displacement versus time at different distance ratio d/λ, using the FEM and the BEM are shown in Figures 6.1 and 6.2 respectively. For the finite element result shown in Figure 6.1, the size of the domain used cannot be further enlarged to accommodate the whole range of d/λ without a substantial increase in the computation cost. Consequently, the reflected waves will be allowed to appear in the time span presented (after the completion of the direct wave) provided that they do not affect the arrival time and peak amplitude. Only the case of d/λ = 10, where both the target and the point of excitation are too close to the boundary, the result seems to be unreliable and will not be used.

The results from both FEM and BEM show the small early motion starting at the arrival time of the plane p-wave. The peak amplitude of these early motions attenuates very fast, as can be seen from both figures. At a large value of d/λ when the cylindrical wavefront can be approximated as a plane, these early motions are barely discernible.
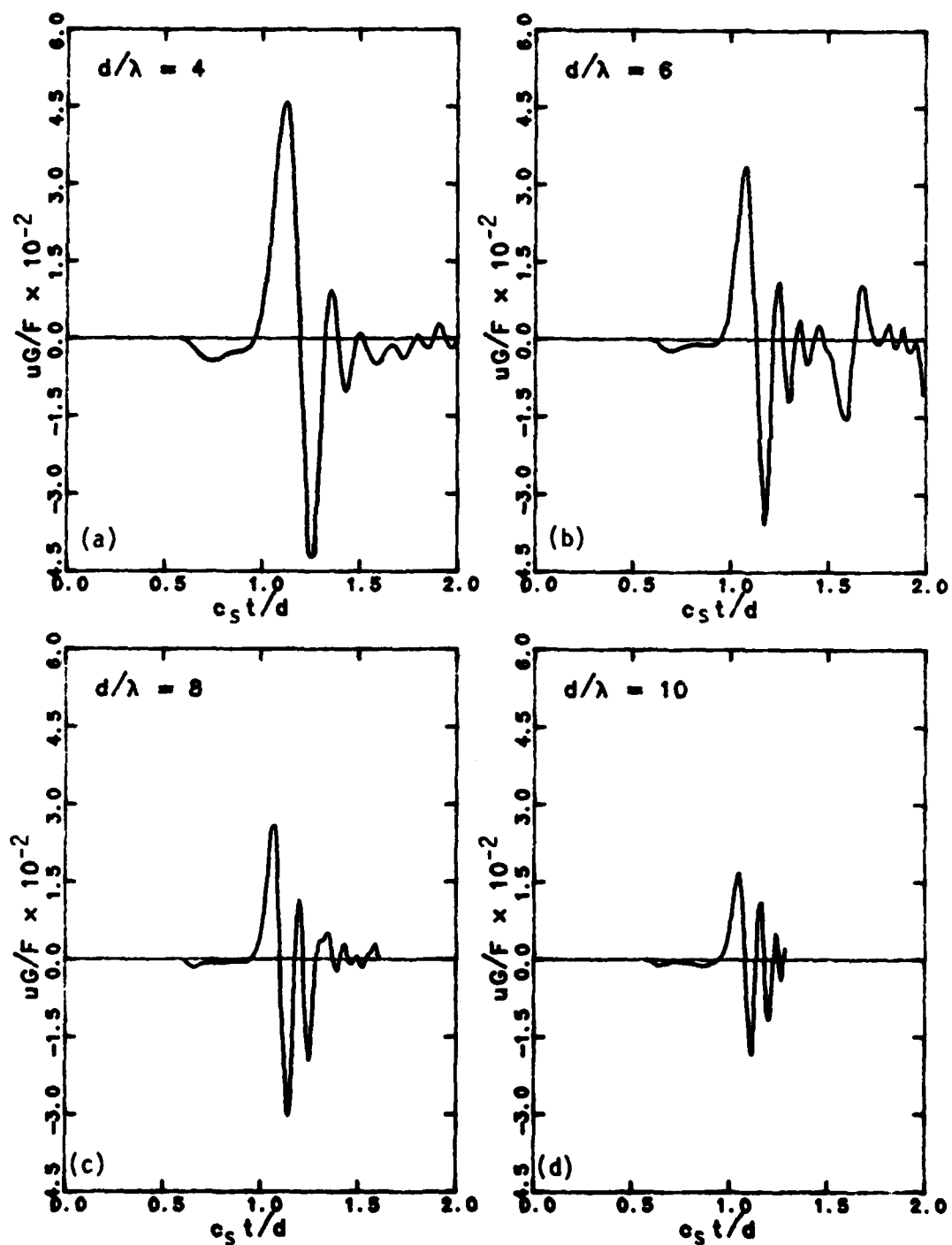
Figure 6.1 - 2-D FEM Free Field Displacement, D = 0.0

84
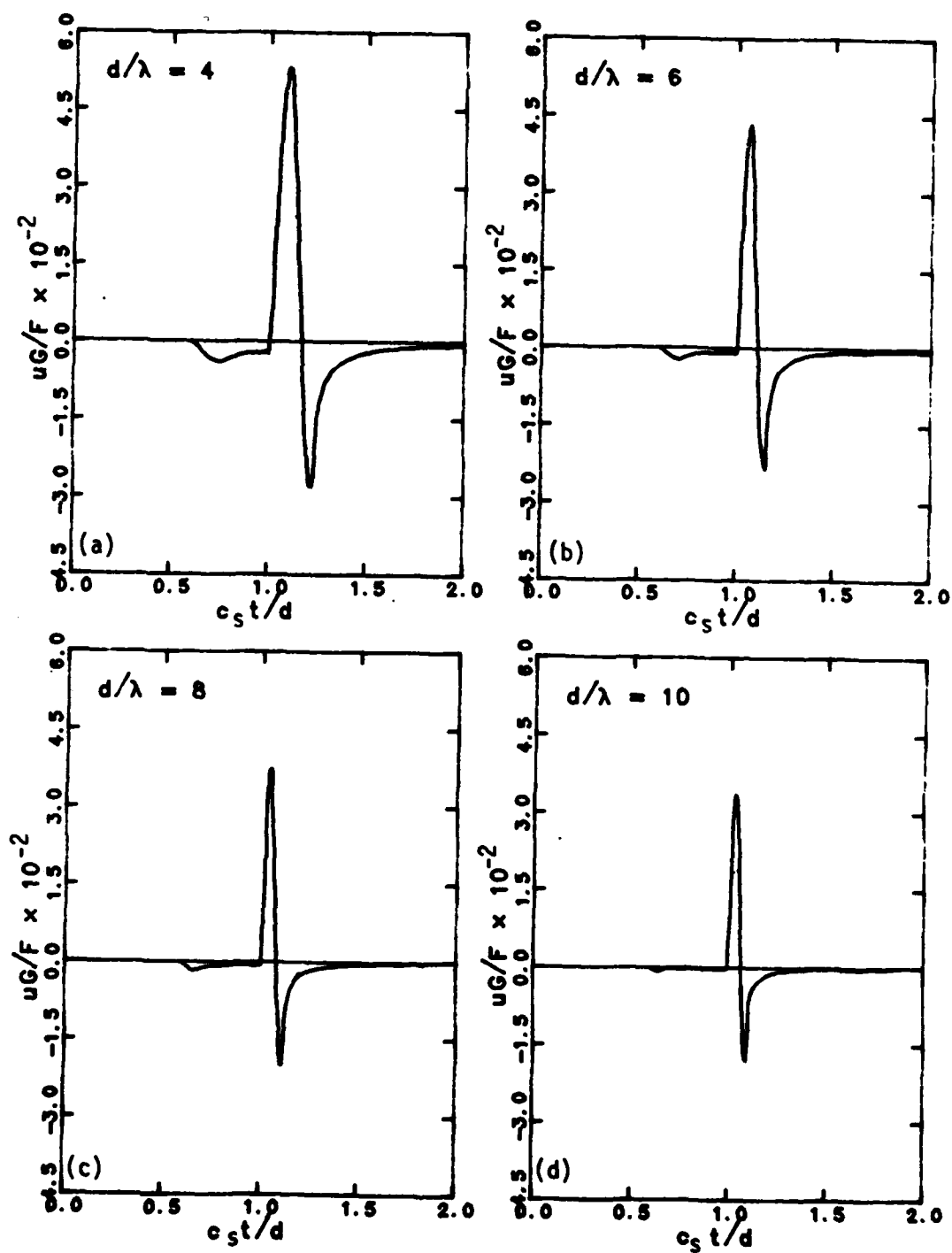
Figure 6.2 - 2-D BEM Free Field, Two-Point Source, D = 0.0

The difference between the results from both methods is clearly seen from Figures 6.1 and 6.2. The first point to note is that the amplitude of the positive peak from the FEM is lower and attenuates at a faster rate than that from the BEM. Both positive and negative peaks in the FEM results are almost the same in magnitude and occur slightly after the corresponding peaks in the BEM results whose negative peak is approximately one half of the positive one. Secondly, the motion after the loading cycle in the BEM decreases asymptotically while in the FEM, the motion is oscillatory with a decay in amplitude with time similar to what could be expected from a lightly damped single degree of freedom system. Finally, the overall shape of the displacement versus time curve from the FEM is smoother. This is evident especially at the point of the first arrival of the S-wave where the displacement from the FEM solution increases less abruptly.

It should be noted that the two-point excitation, simulating the condition in the finite element model, is used in the BEM result shown in Figure 6.2 so that results from both methods can be more reasonably compared. Any differences resulting from the use of either a single point or a two-point excitation should be more evident in the results with target points closer to the source. Figures 6.3 and 6.4 show the BEM results for such close range targets (d/λ from 0.5 to 1.0) using a two-point and a single point excitation respectively. Only a close look at the case of lowest d/λ reveals that the displacement amplitude in the case of a two-point excitation is slightly lower. The difference is, however, very small and it can be concluded that, for d/λ of 0.5 and lar-
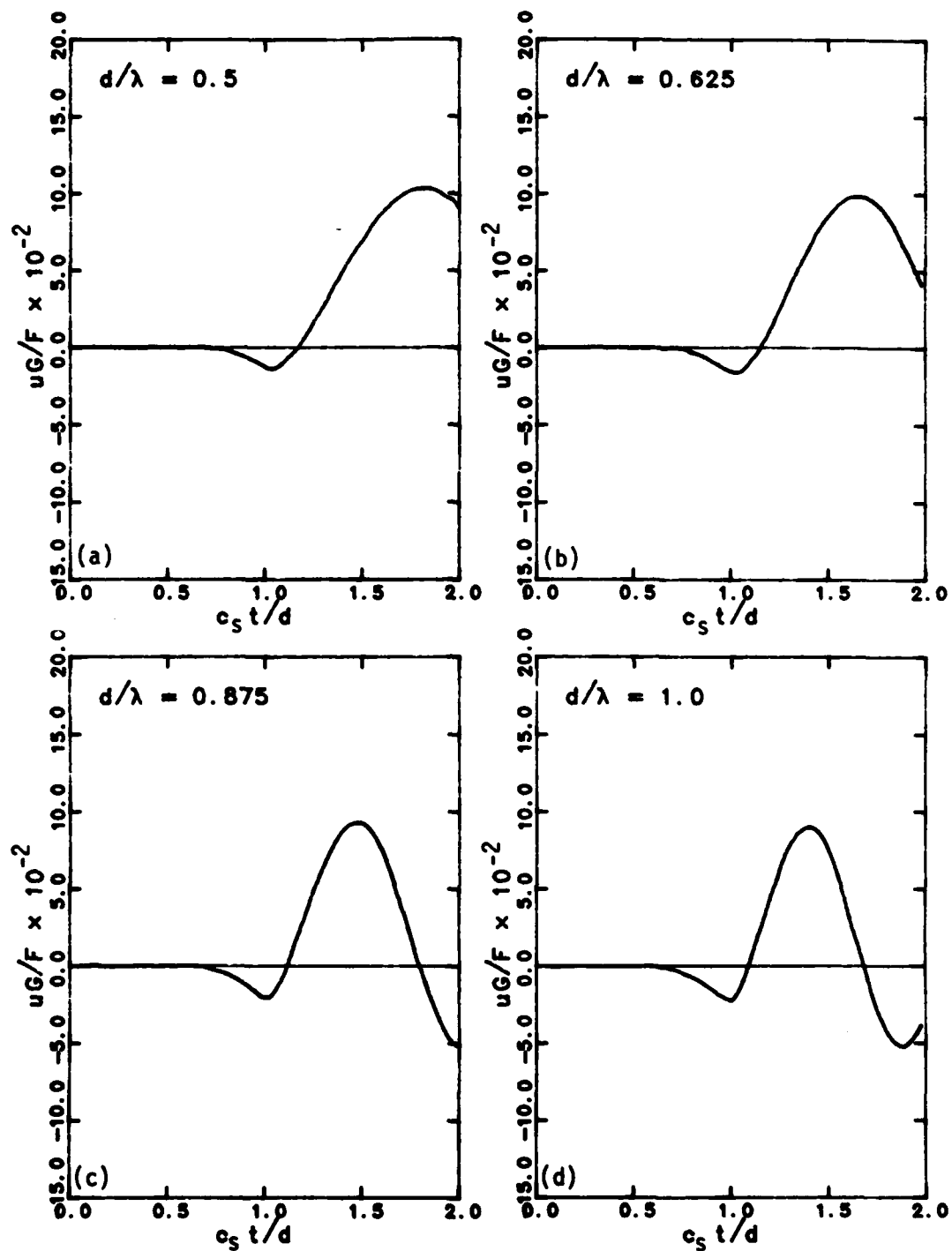
Figure 6.3 - 2-D BEM Free Field, Two-Point Source, Short Range, D = 0.0
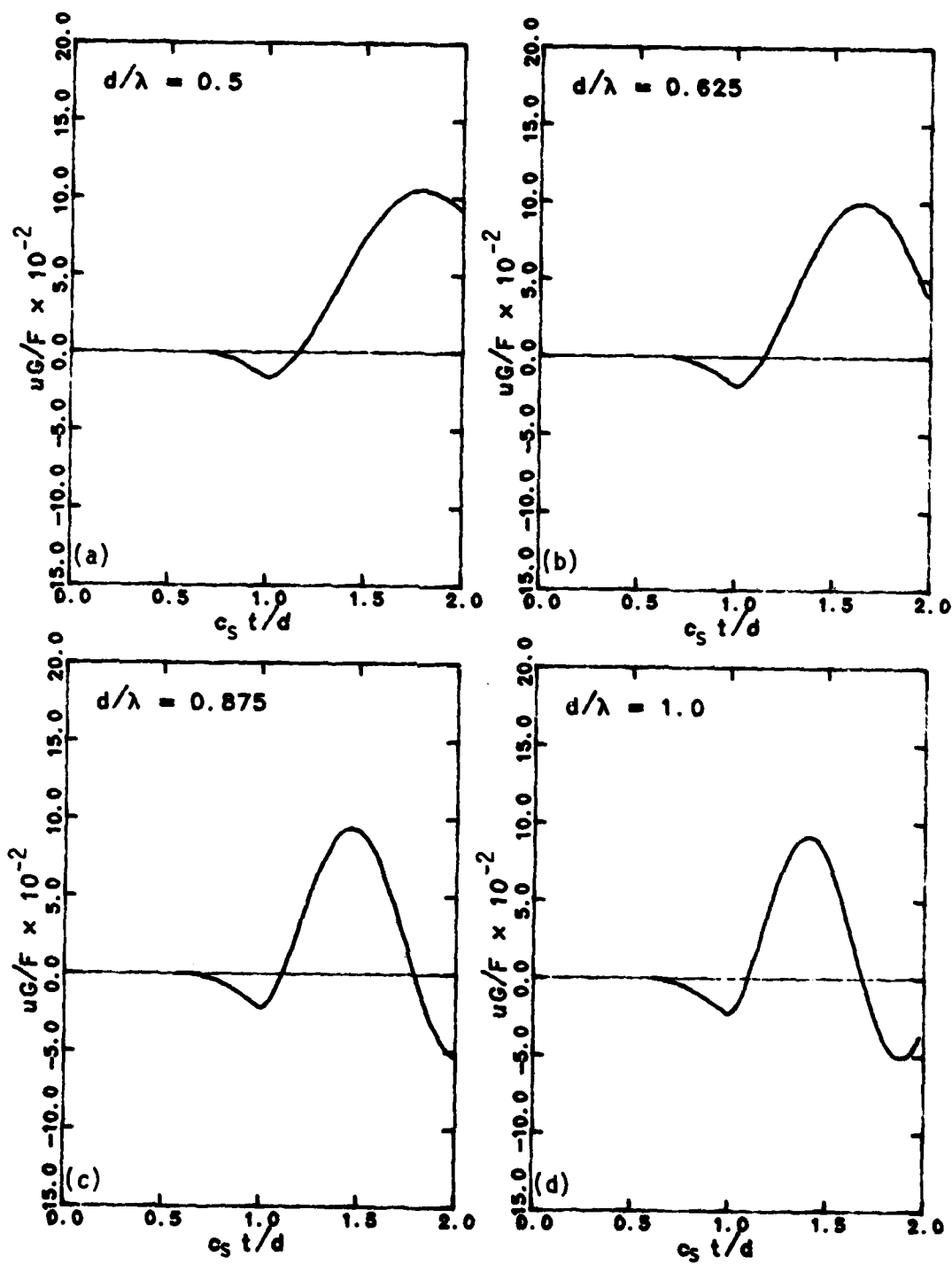
Figure 6.4 - 2-D BEM Free Field, Single Point Source, D = 0.0

ger, a single point and a two-point excitation give the same results. Therefore, a single point excitation as originally formulated will be used in all BEM analyses presented later.

Figure 6.5 shows the FEM results for the same close range targets which are still smoother than the BEM results shown in Figures 6.3 and 6.4. The interesting point is that the displacement amplitudes in this range are higher than the corresponding BEM results.

Figure 6.6 also shows the close range results from the BEM using a single point excitation as in Figure 6.4, but with soil damping ratio of 0.05. The peak amplitudes are noticeably lower than for the case without damping (Figure 6.4), and the curves are also smoother similarly to the FEM result.

Figures 6.7, 6.8, and 6.9 show the BEM results at long distance targets for the case of soil damping ratios D of 0.0, 0.02, and 0.05 respectively. By comparing Figure 6.7 to Figure 6.2 at the same d/λ, the insignificant effect of a two-point versus a single point excitation is confirmed. The soil damping also has the same effects of the results of the long distance targets as in the short range, i.e., the amplitude is lower with the smoother and rounder curves resembling the FEM results. This makes the estimation of the wave arrival time more difficult, unlike the case without soil damping in Figure 6.7 where the time of arrival of the wave is very well defined by the sharp rise toward the first positive peak. From all results above, it appears that the time of arrival of the wave decreases with increasing soil damping.
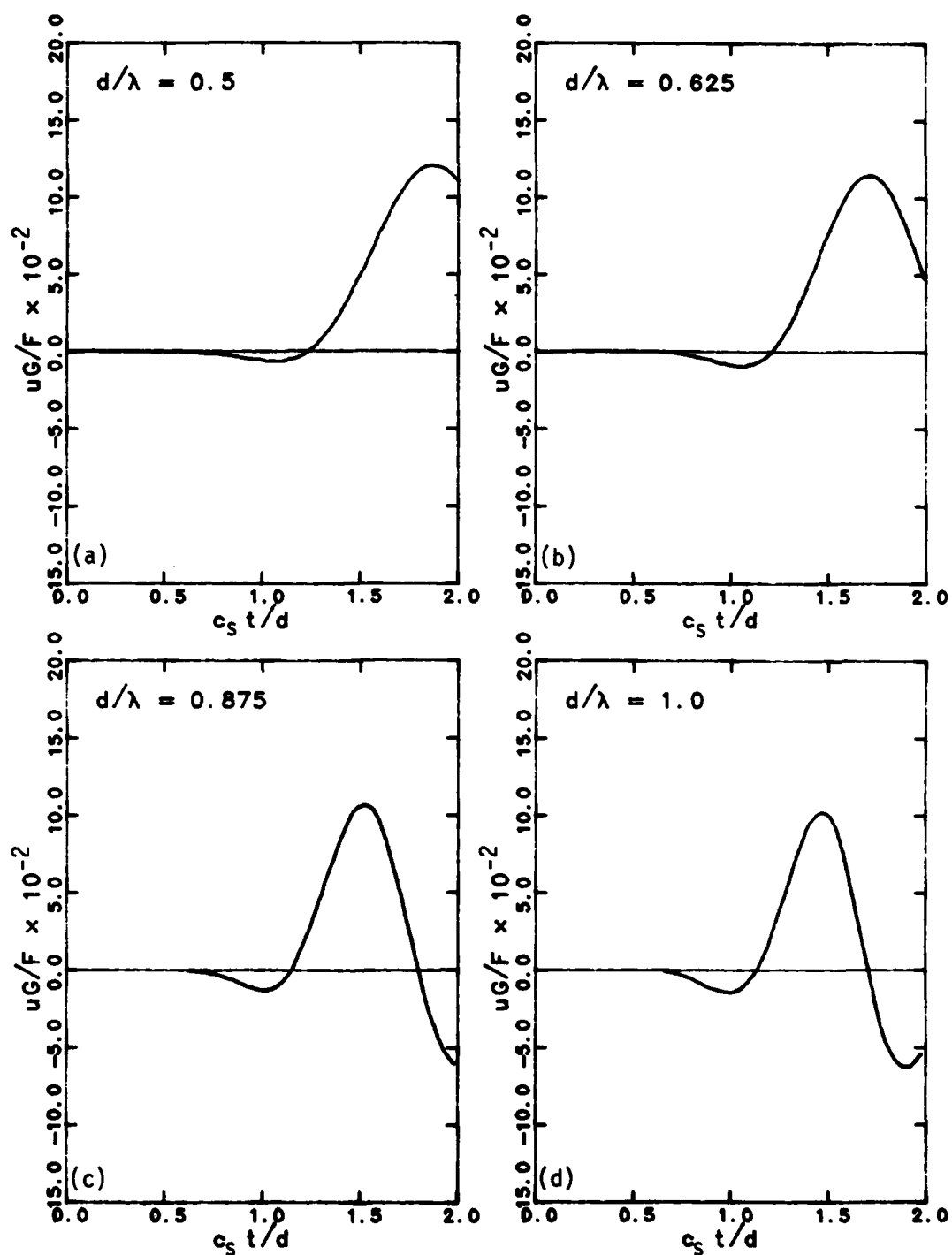
Figure 6.5 - 2-D FEM Free Field Displacement, Short Range, D = 0.0

90
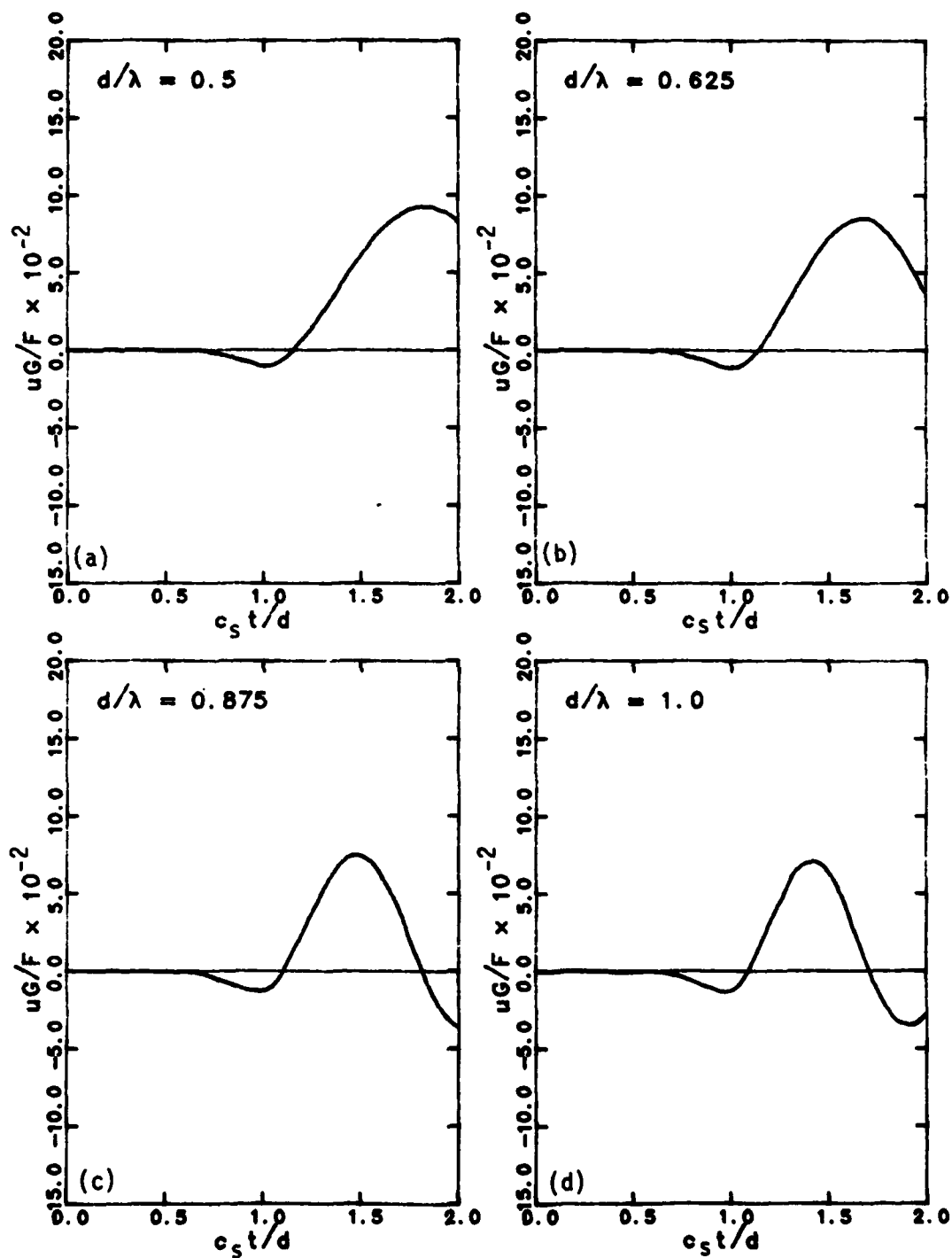
Figure 6.6 - 2-D BEM Free Field, Single Point Source, D = 0.05
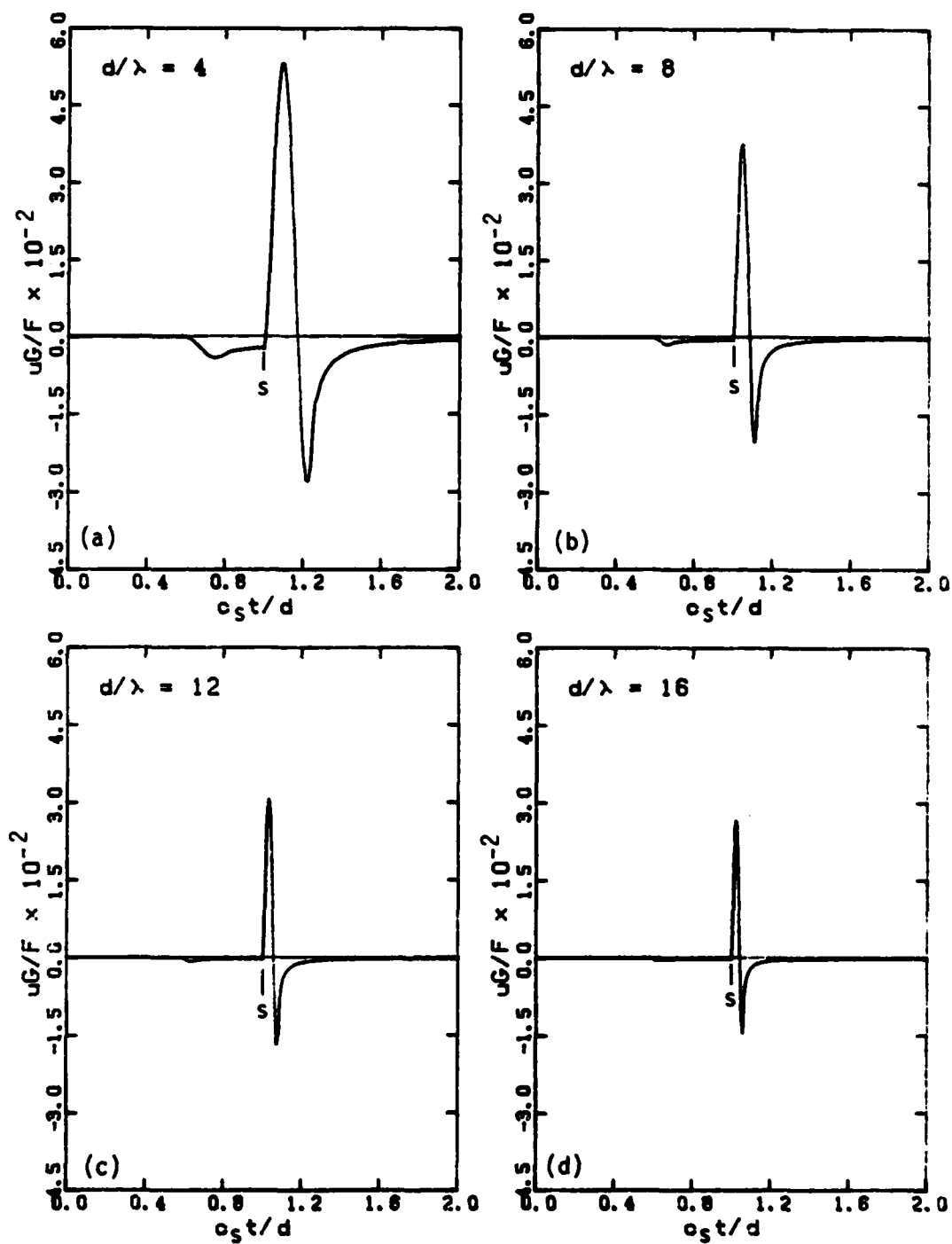
Figure 6.7 - 2-D BEM Free Field, D = 0.0
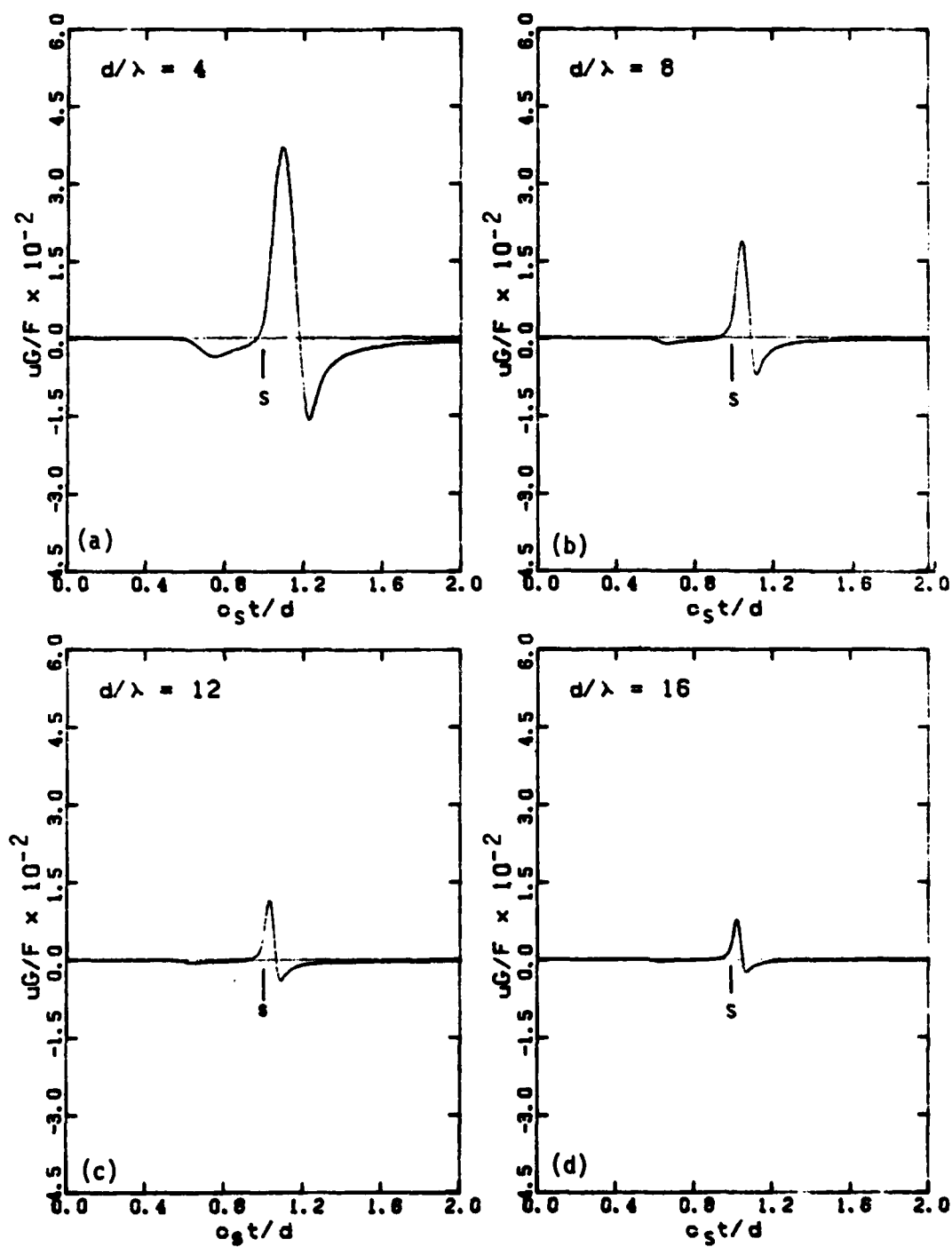
Figure 6.8 - 2-D BEM Free Field, D = 0.02
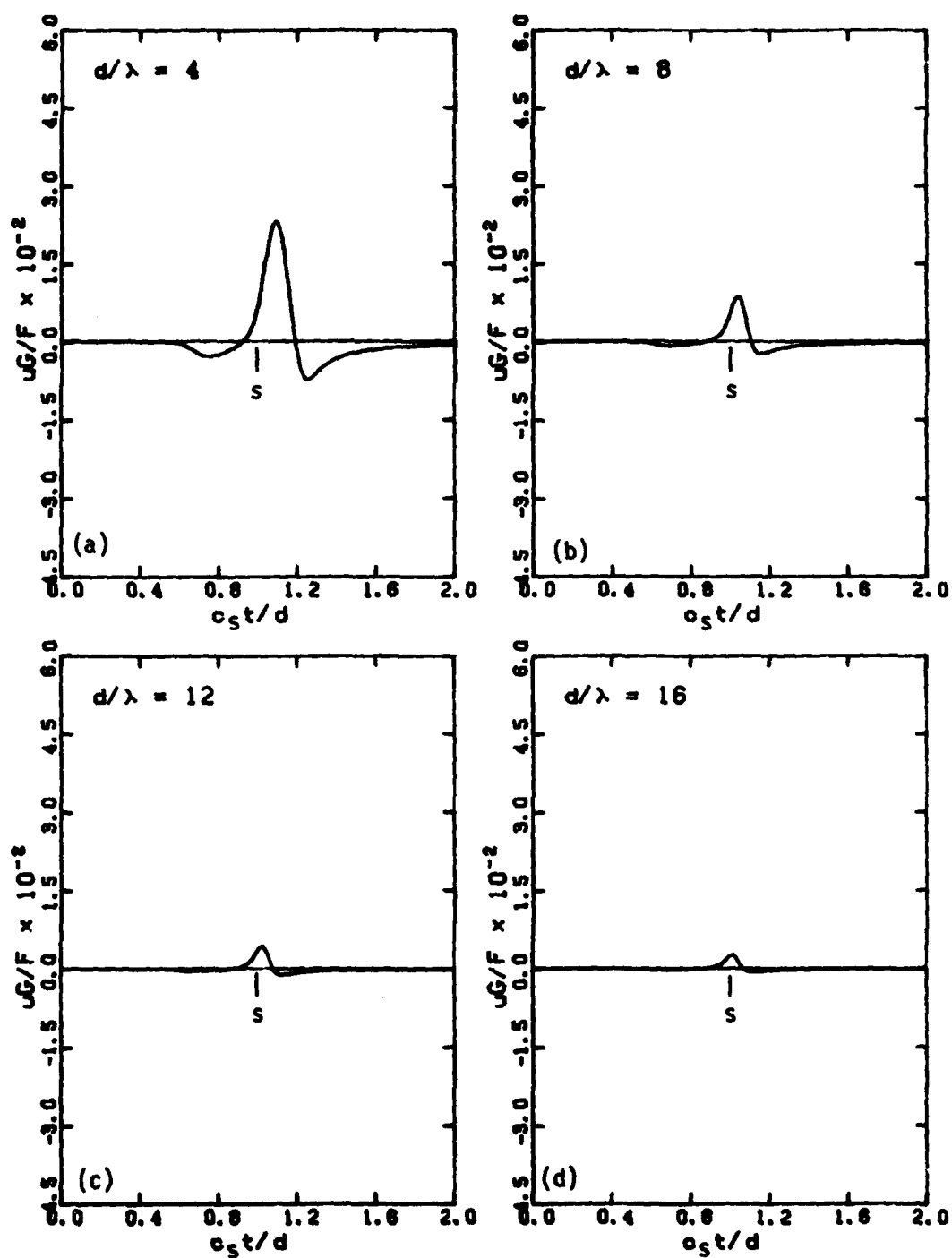
Figure 6.9 - 2-D BEM Free Field, D = 0.05

Using log-log scale, the amplitudes of the first positive peak
are plotted versus d/λ for different soil damping ratios, as shown in
Figure 6.10. The amplitudes from the FEM results (without damping) are
also plotted together in the same figure. For the BEM results, the plot
is a straight line with a slope equals to -1/2 when there is no soil
damping. This follows the geometrical damping law for the cylindrical
wavefront. This curve, however, deviates from a straight line as d/λ
decreases, a point which will be discussed later. In the cases with soil
damping, the waves attenuate at a faster rate as shown in the plots with
the lines curving downward. As the distance d becomes smaller, there are
less differences in the peak amplitudes among all cases.

Figure 6.10 also reveals another distinct character of a cylin-
drical wavefront. In the figure, the log-log plots of the attenuation
for all soil dampings have maximum curvature at a distance of approxi-
mately one wavelength (d/λ = 1). As the distance becomes smaller, all
plots show a reverse curvature and tend to approach each other. Further
investigations reveal that, in the case of a pure shear wave, as caused
by an antiplane excitation (SH-wave), there is no break in the curvature
and the plot for the case without damping is a straight line throughout.
The deviation from a straight line as d/λ becomes smaller in Figure 6.10
is, therefore, due to the combination of SV-and P-waves caused by an
inplane excitation.

Figure 6.10 shows further that the wave amplitudes from the FEM
solution attenuate faster than those from the BEM (both have no damping).
The amplitude from the FEM is slightly larger for d/λ below 2, and
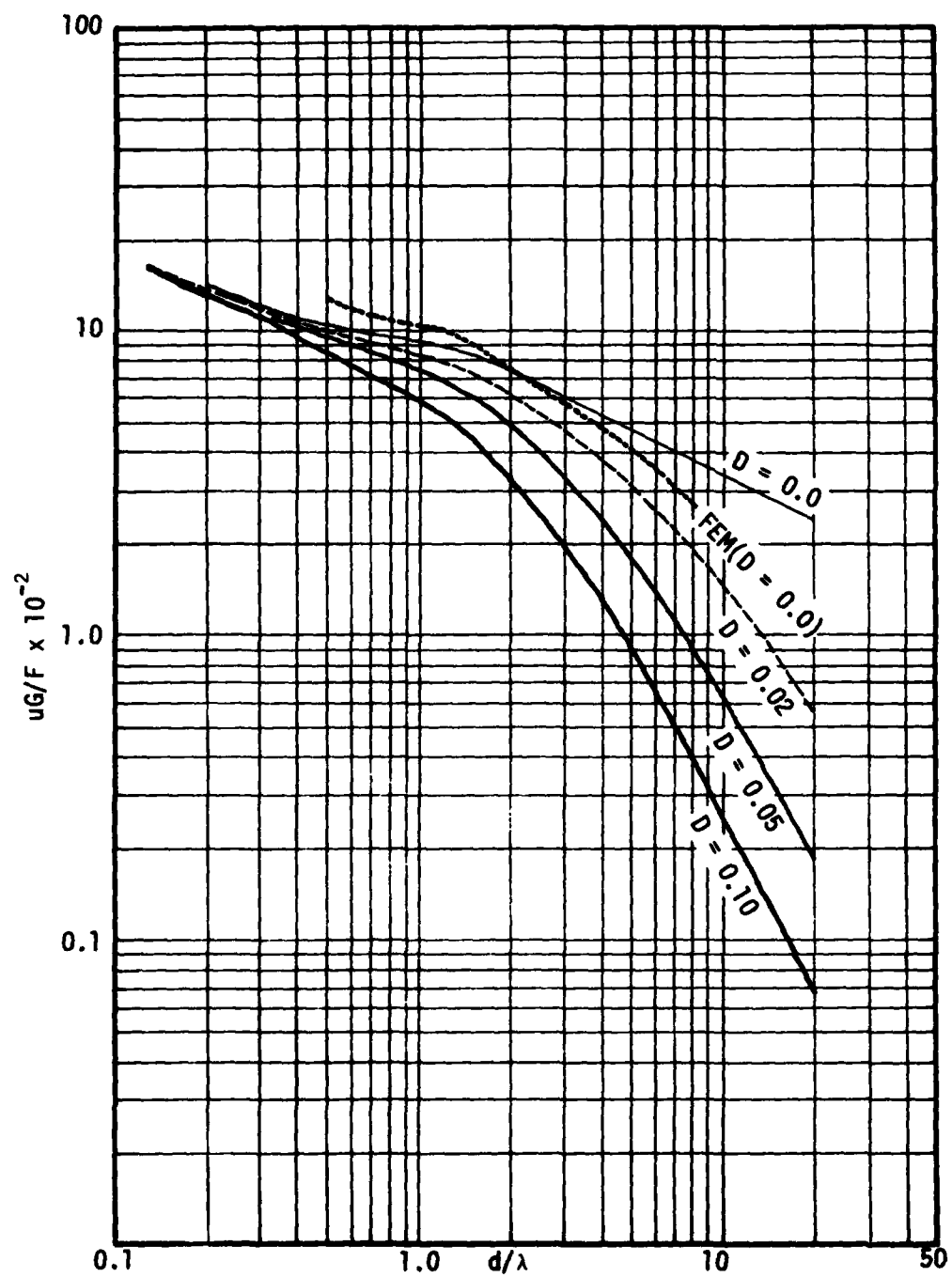
Figure 6.10 - 2-D Attenuation, Free Field

becomes smaller than the amplitude from the BEM for larger distances. The important point to note is that the plot of the FEM does not show any straight line portion as in the BEM even though there is no soil damping. From these results together with the curves of the displacement versus time presented earlier, it appears that the finite element model behaves like a system with a small amount of material damping on the order of 1 percent.
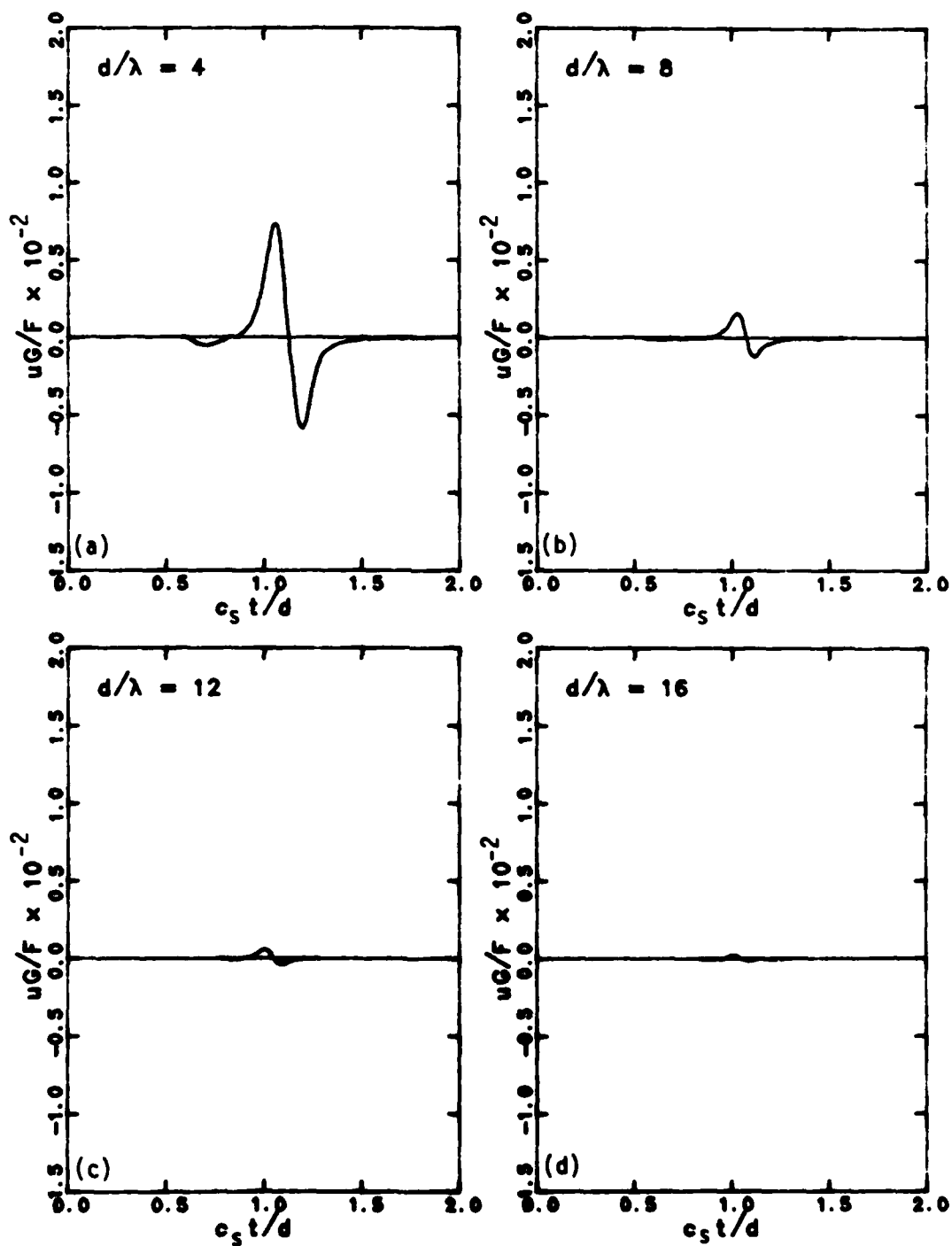
6.1.2 Three-Dimensional Case

The three-dimensional free field displacements for different values of d/λ are shown in Figures 6.11, 6.12, and 6.13 for $D = 0.0$, 0.02, and 0.05 respectively. All results show the early motion starting at the arrival time of the plane P-wave which attenuates very fast as the distance increases. In the case $D = 0.0$, the results show again a well-defined time of arrival of the wave while in the case with soil damping, the results become smoother, and it also appears that the arrival time of the S-wave decreases with increasing soil damping.

While the points mentioned above are all similar to those of the two-dimensional case shown in Figure 6.7 to Figure 6.9, the main differences between the two cases are obvious. In the three-dimensional case, the positive and the negative peaks are comparable in magnitude, and the displacement after a complete cycle is perfectly zero instead of decreasing asymptotically. The shape of the displacement curve in this case, therefore, retains closely the sinusoidal shape of the excitation
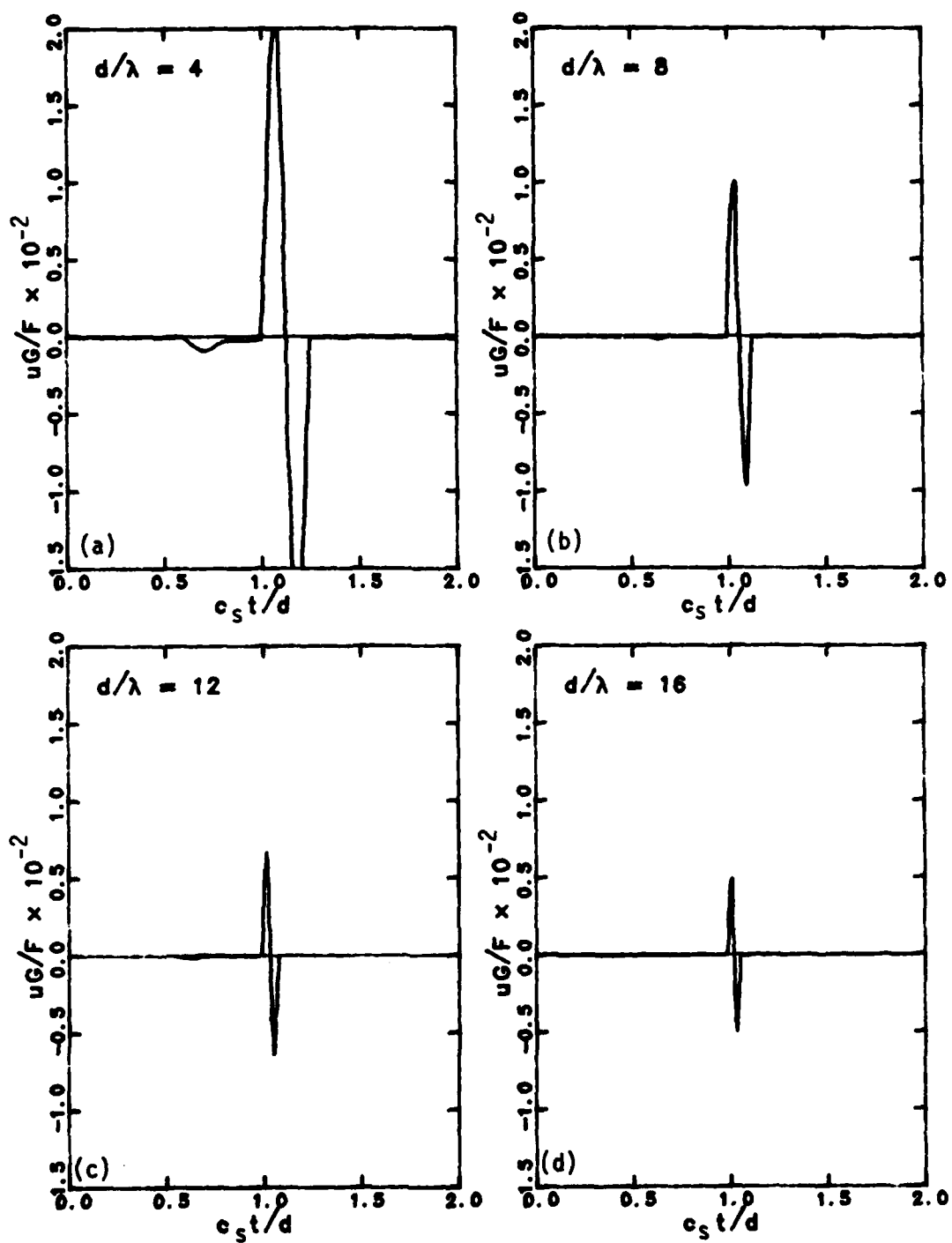
Figure 6.11 - 3-D BEM Free Field, D = 0.0
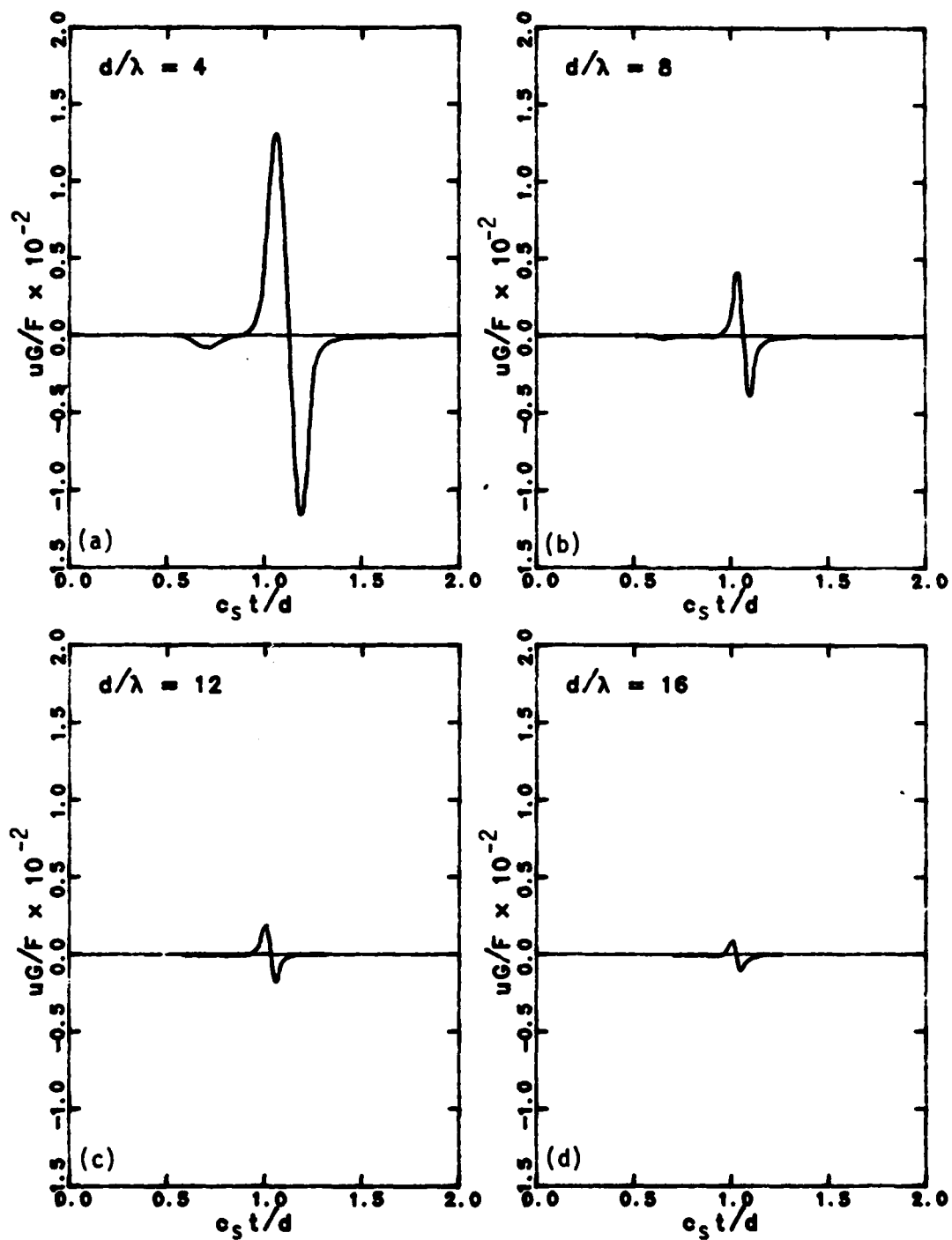
Figure 6.12 - 3-D BEM Free Field, D = 0.02

Figure 6.13 - 3-D BEM Free Field, D = 0.05

except for the early motion part which almost disappears at larger distances.

Figures 6.14 and 6.15 show the three-dimensional free field displacements at close range targets (d/λ from 0.5 to 1.0) for D = 0.0 and 0.05 respectively. They still reproduce a better sinusoidal shape of the excitation with more balanced negative and positive peaks than the two-dimensional case shown in Figures 6.4 and 6.5. In addition, the change in the direction of the motion seems to be more abrupt in the three-dimensional case as shown in the curve as a sharp rise at the S-wave arrival time in the case D = 0.0. All results from both two and three-dimensional cases also show that the period T of the motion slightly increases with the damping ratio of soil.

Figure 6.16 shows the attenuation curves for all soil damping in log-log scale. Similarly to the two-dimensional case in Figure 6.10, all results have the maximum curvature at d/λ = 1. The plots show a reverse curvature and tend to approach each other at small values of d/λ The only difference from the two-dimensional case is the steeper slope which indicates the faster rate of attenuation in the three-dimensional case. For D = 0.0 and d/λ larger than 2, the plot shows a straight line portion with the slope equal to -1. This agrees with the geometrical damping law for a spherical wavefront.

6.2   EFFECT OF AN INCLUSION ON ATTENUATION

Attenuation studies were conducted next with one square inclu-
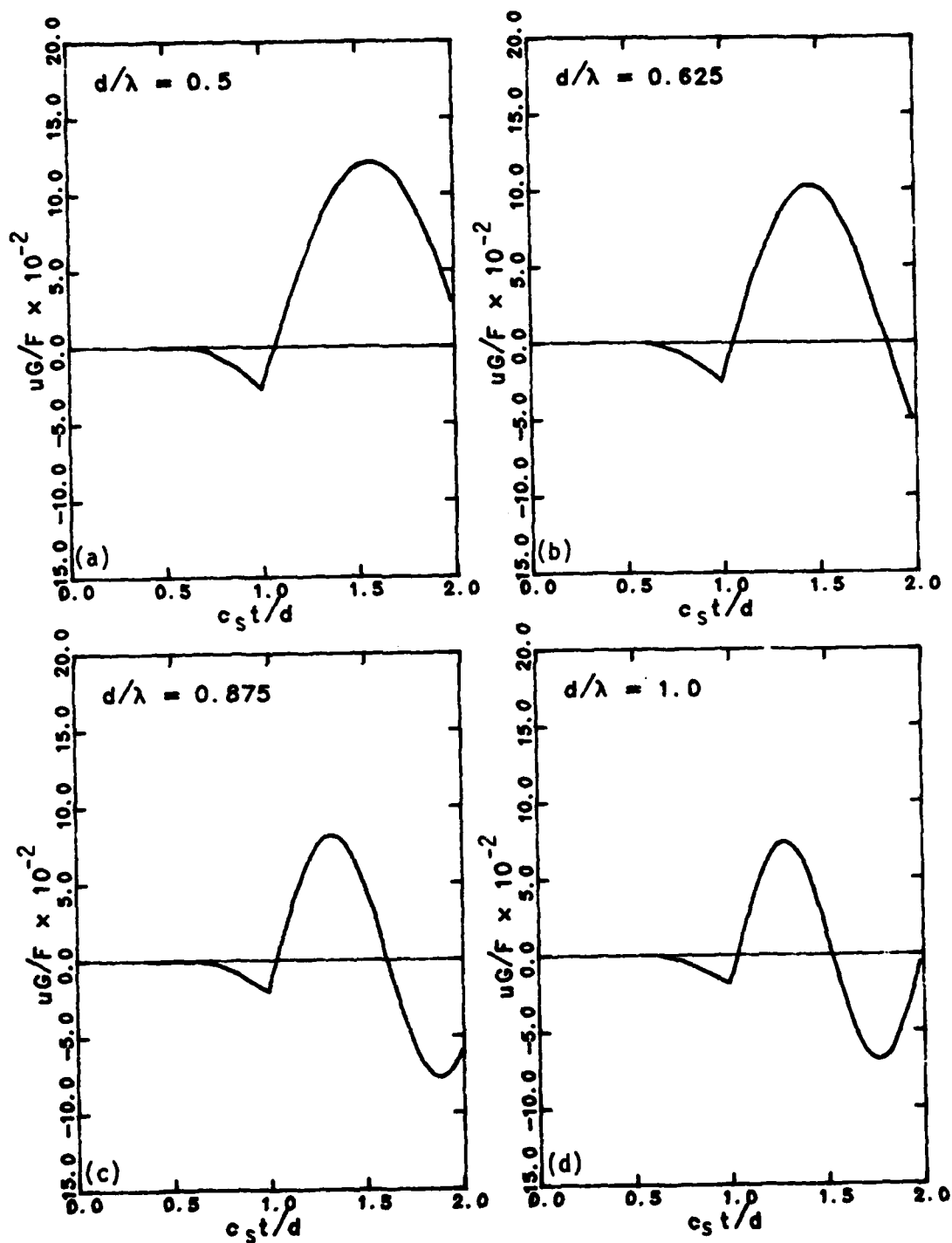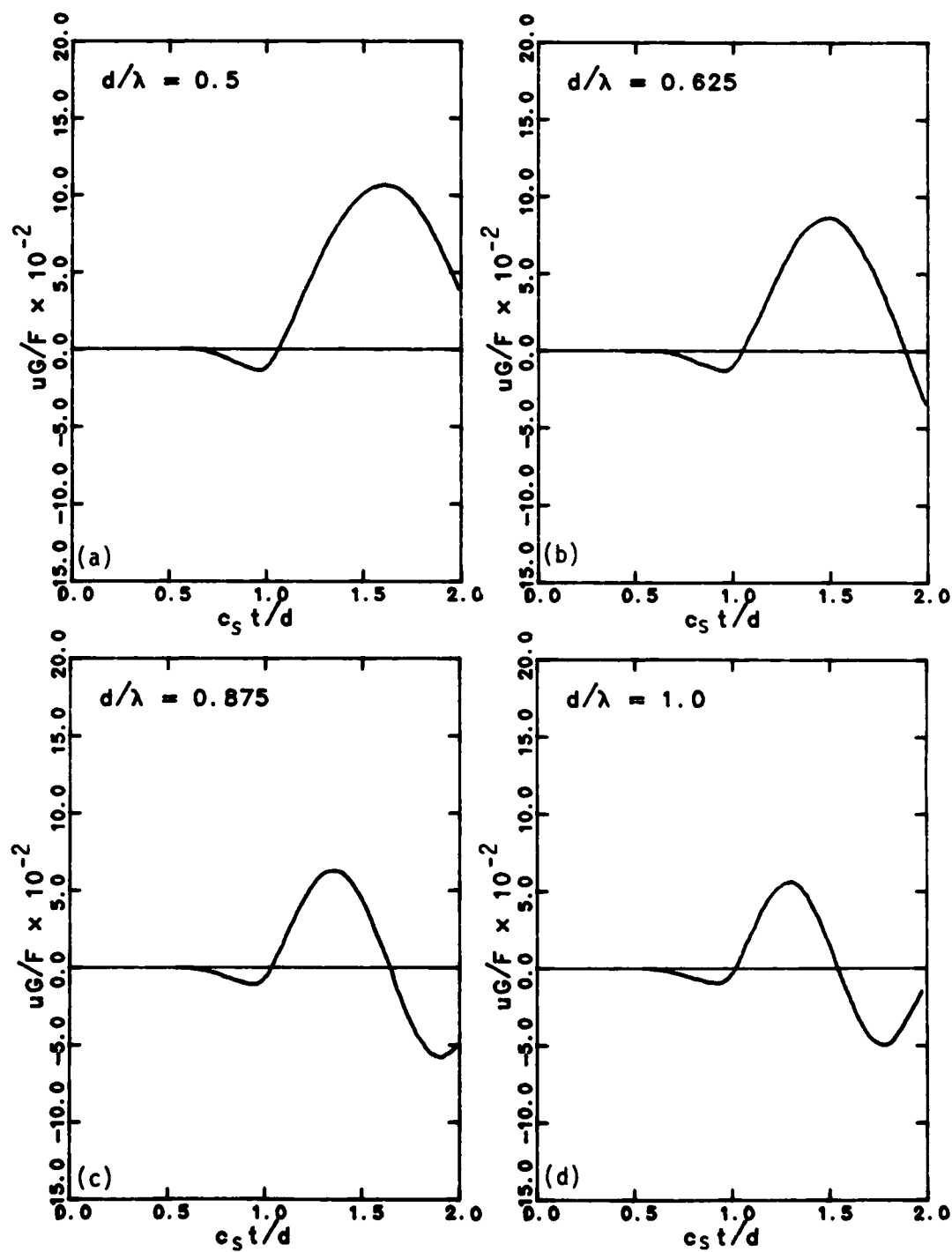
Figure 6.14 - 3-D BEM Free Field, Short Range, D = 0.0

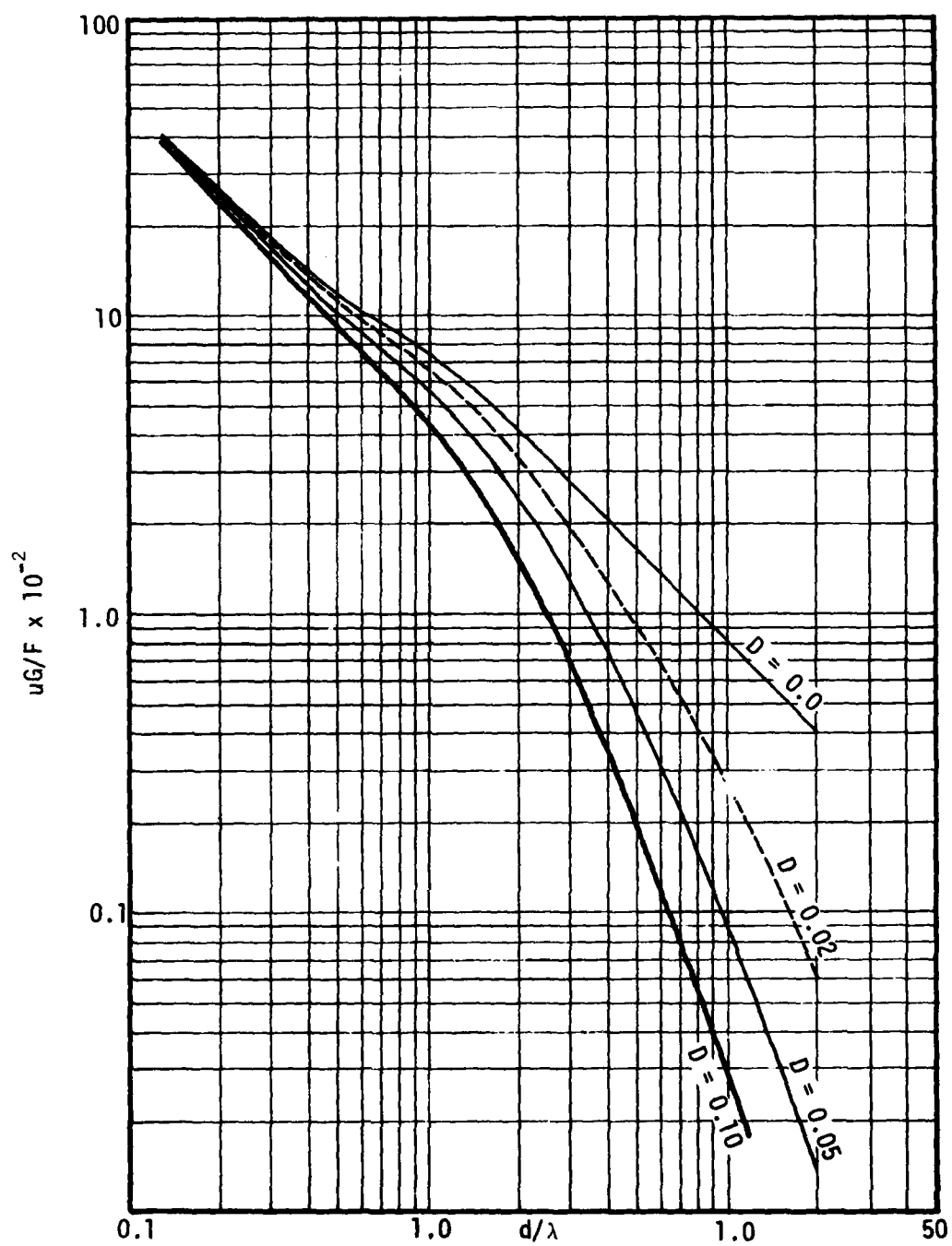Figure 6.15 - 3-D BEM Free Field, Short Range, D = 0.05

Figure 6.16 - 3-D Attenuation, Free Field

sion (cubic in the three-dimensional case) having side dimension 'a' located between the excitation point and the target. Preliminary analyses for small inclusions (a/λ up to 1/4) indicated that the results were insensitive to the position of the inclusion between the excitation and the target points. No studies were performed for the case of larger inclusions where the position of the inclusion may have some effects on the results. For all cases to be consistent, the inclusion was located at a fixed position varying the position of the target in order to obtain results for different values of d/λ from a single run. Various sizes of the inclusion relative to the wavelength λ were used. The inclusion had no damping and its properties (shown with subscript 'b') relative to soil were

$$c_{sb}/c_s = 10.0 \ , \ \rho_b/\rho = 1.0$$

where c_s is the shear wave velocity, and ρ is the unit mass.

6.2.1 Two-Dimensional Case

The displacements for the case of one square inclusion with size a/λ = 1/8, and soil damping ratios D of 0.0, 0.02, and 0.05 are shown in Figures 6.17, 6.18, and 6.19 respectively. Only a close comparison with the corresponding free field case can reveal a slightly smaller amplitude in this case. An inclusion of this size is too small in relation to the wavelength to have any significant effects. This can
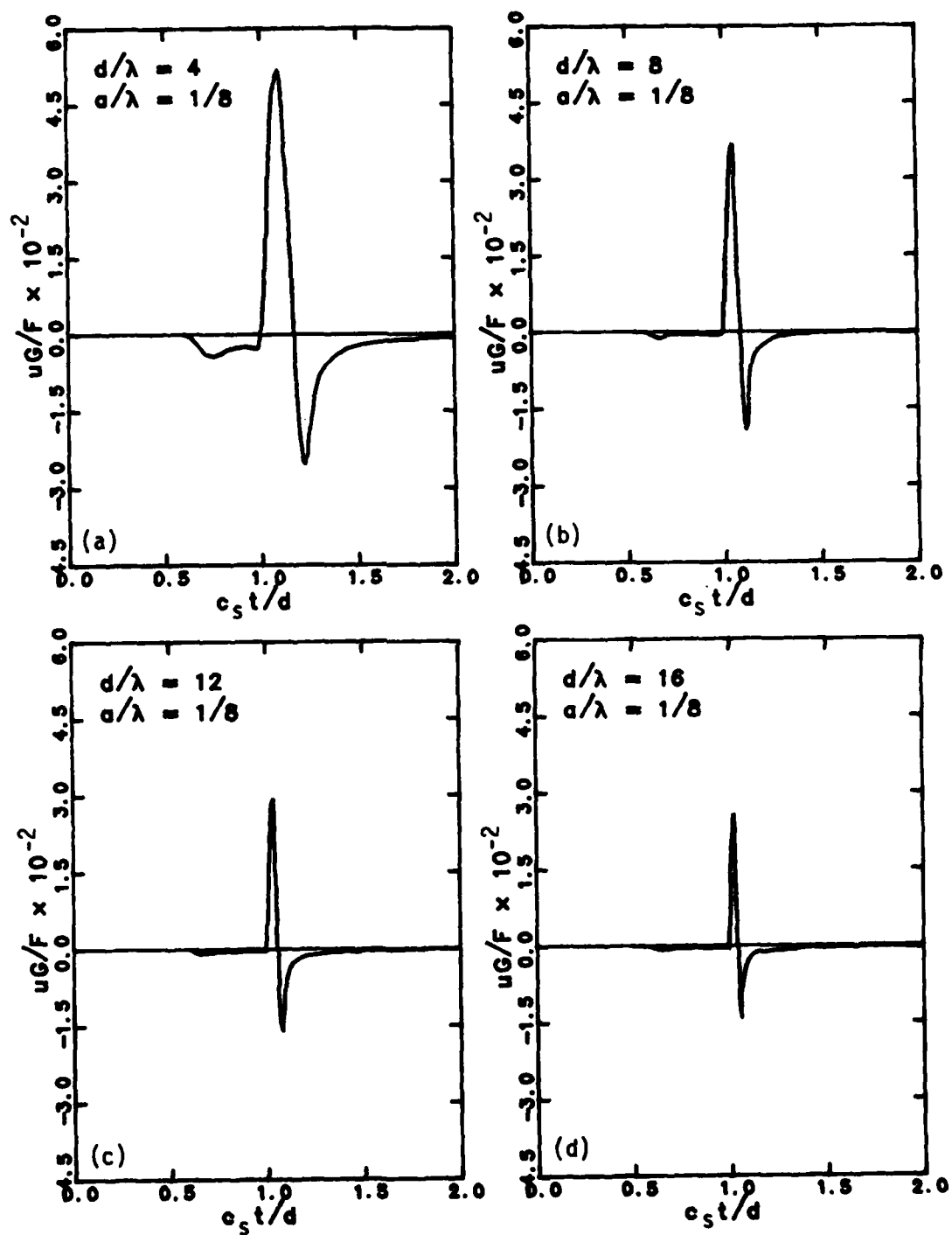
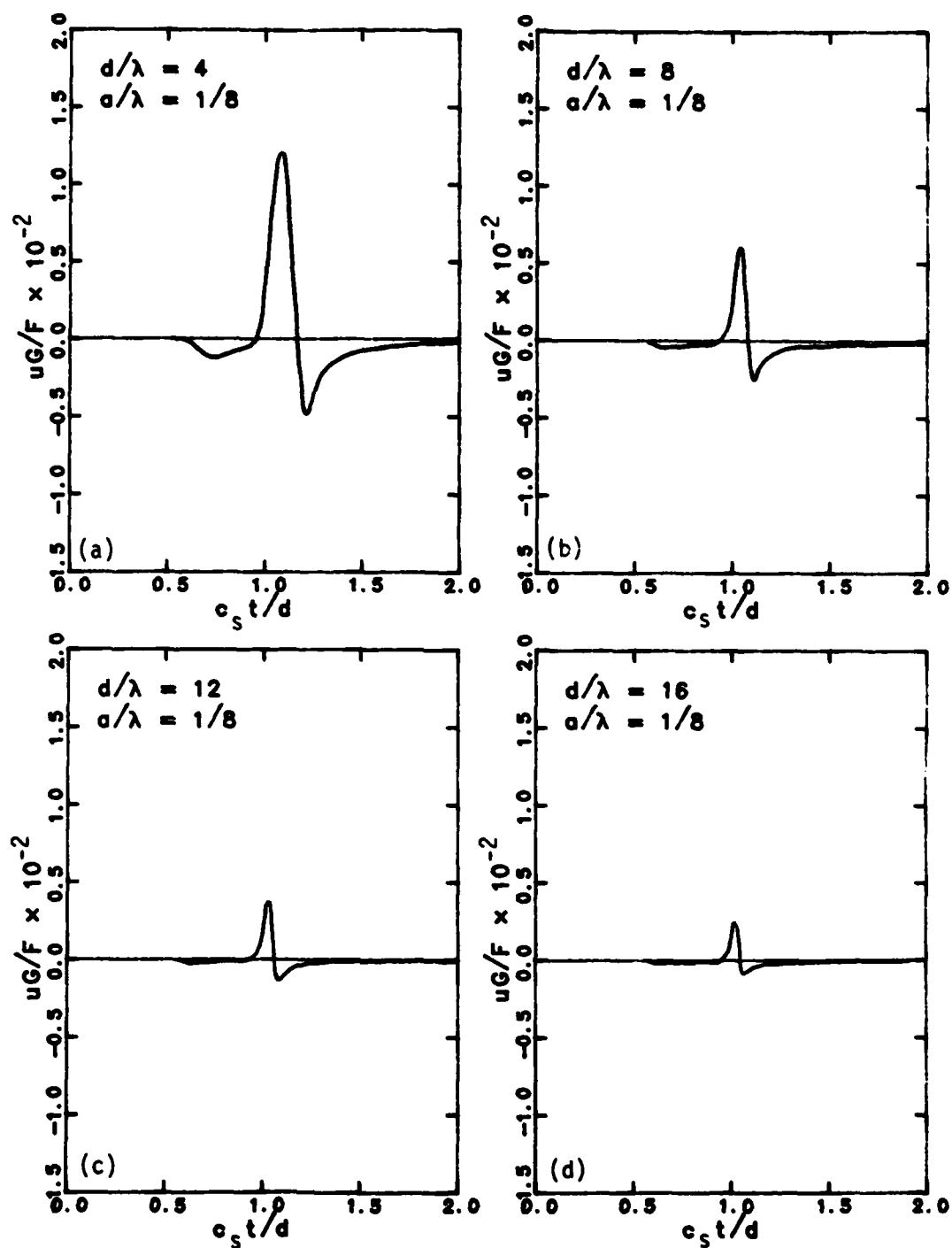Figure 6.17 - 2-D Displacement, One Inclusion, $a/\lambda = 1/8$, $D = 0.0$

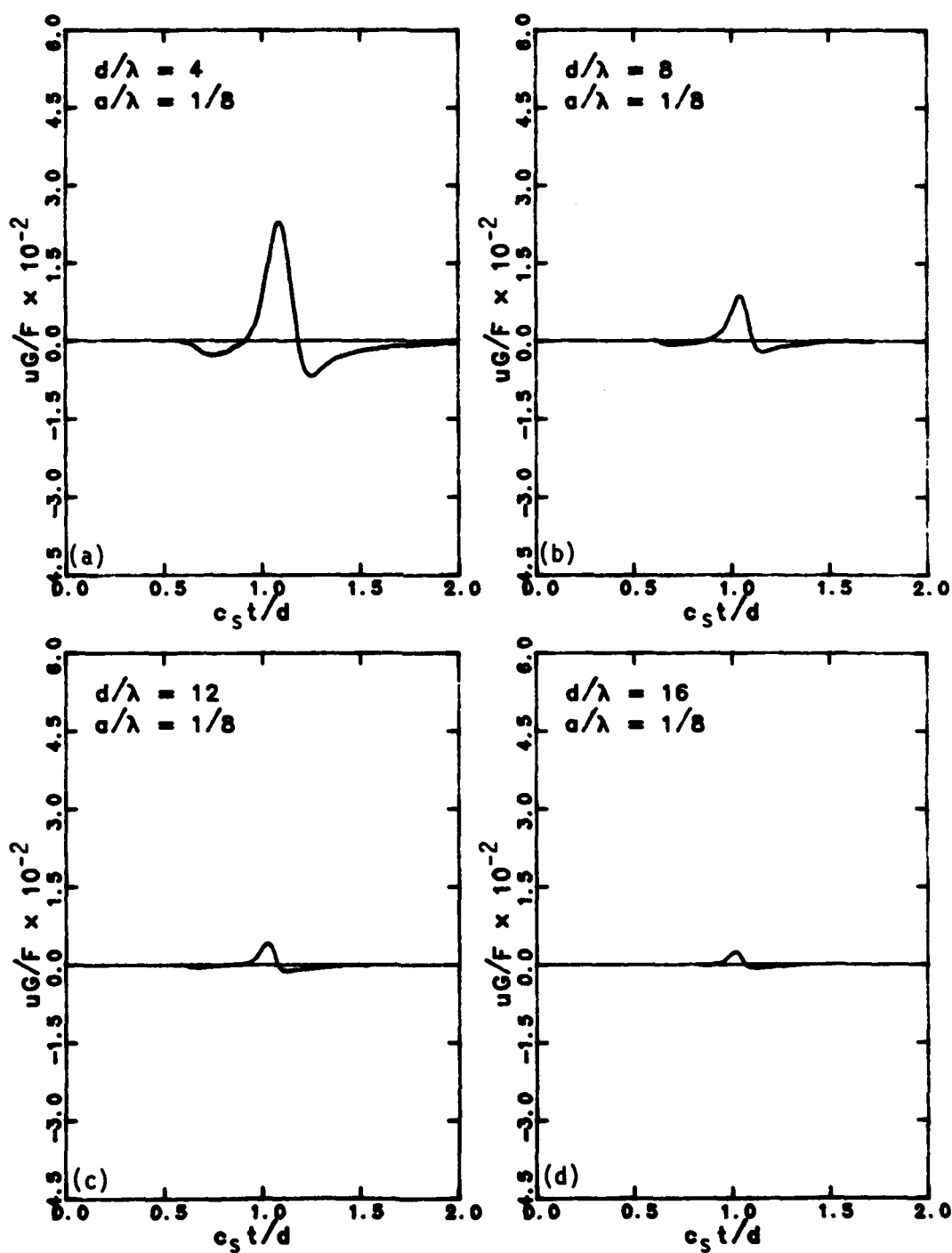Figure 6.18 - 2-D Displacement, One Inclusion, $a/\lambda = 1/8$, $D = 0.02$

Figure 6.19 - 2-D Displacement, One Inclusion, a/λ = 1/8, D = 0.05

also be seen in the results with soil damping and the attenuation curves shown in Figure 6.20 which are almost the same as in the free field case.

When the size of the inclusion is doubled ($a/\lambda = 1/4$), the shape of the displacement curves is still similar to those of the free field case but the amplitudes decrease. This can be seen in Figures 6.21, 6.22, and 6.23 for damping ratios of 0.0, 0.02, and 0.05 respectively. The soil damping still has the same effects of smoothening the motion and reducing the wave arrival time. The attenuation curves shown in Figure 6.24 still exhibit the same characteristics of wave attenuation as in the free field except that the amplitude is lower.

As the inclusion size is further increased ($a/\lambda = 1/2$), the over-all amplitudes are reduced even more as shown in Figures 6.25, 6.26, and 6.27 for $D = 0.0$, 0.02, and 0.05 respectively. Figure 6.28 shows that the attenuation curves in this case still have shapes similar to those of the free field but with lower amplitude.

When comparing the results from all sizes of inclusion, it can be noticed that displacement versus time curves are shifted more to the left as the inclusion getting larger. This indicates a faster wave velocity which is reasonable because, with a larger inclusion, the wave will travel less in soil and more in an inclusion which has higher shear wave velocity. The effects of the inclusion on the wave arrival time will be discussed in the next chapter.

A close comparison between the displacement versus time curves from each inclusion size also reveals that the period T of the motion
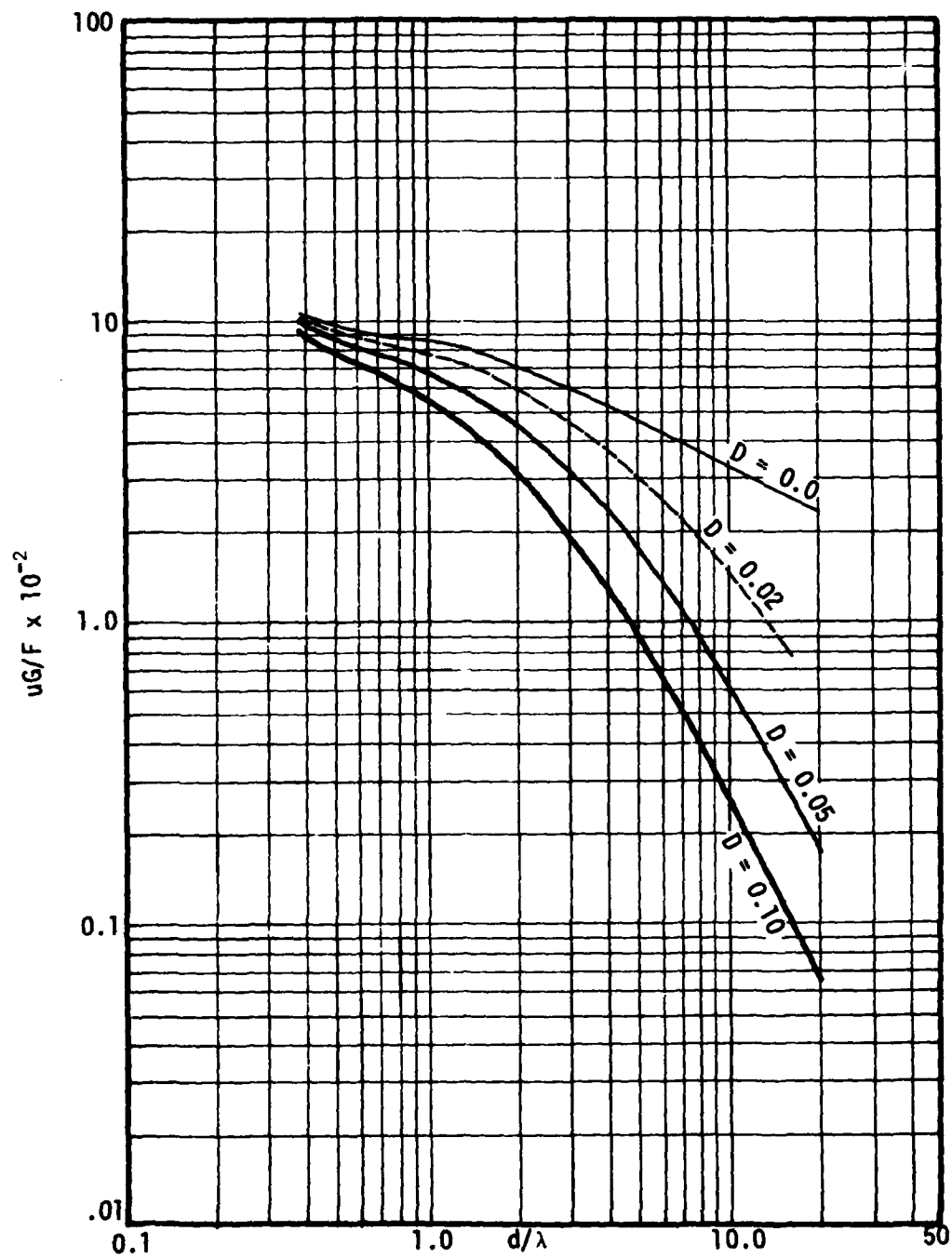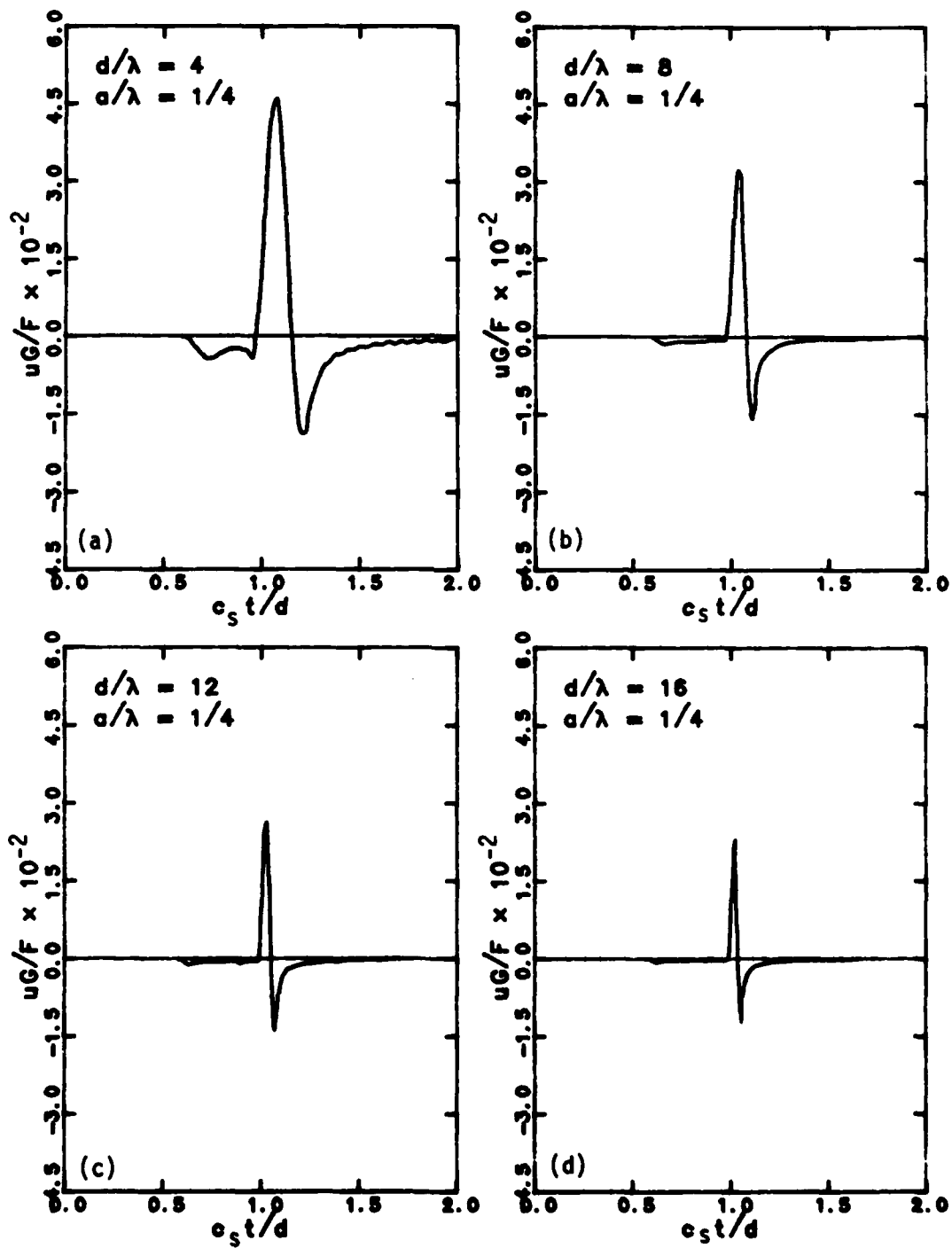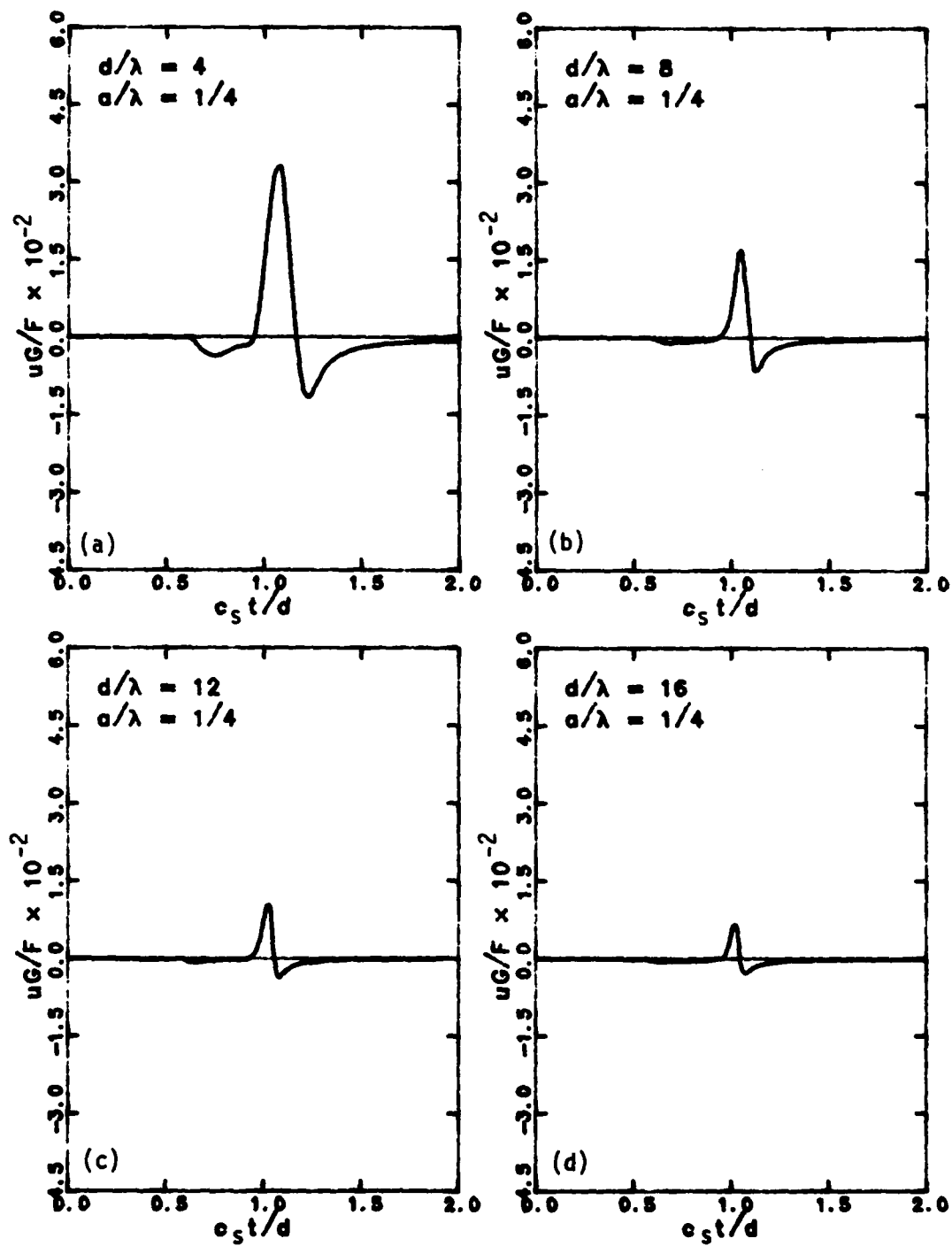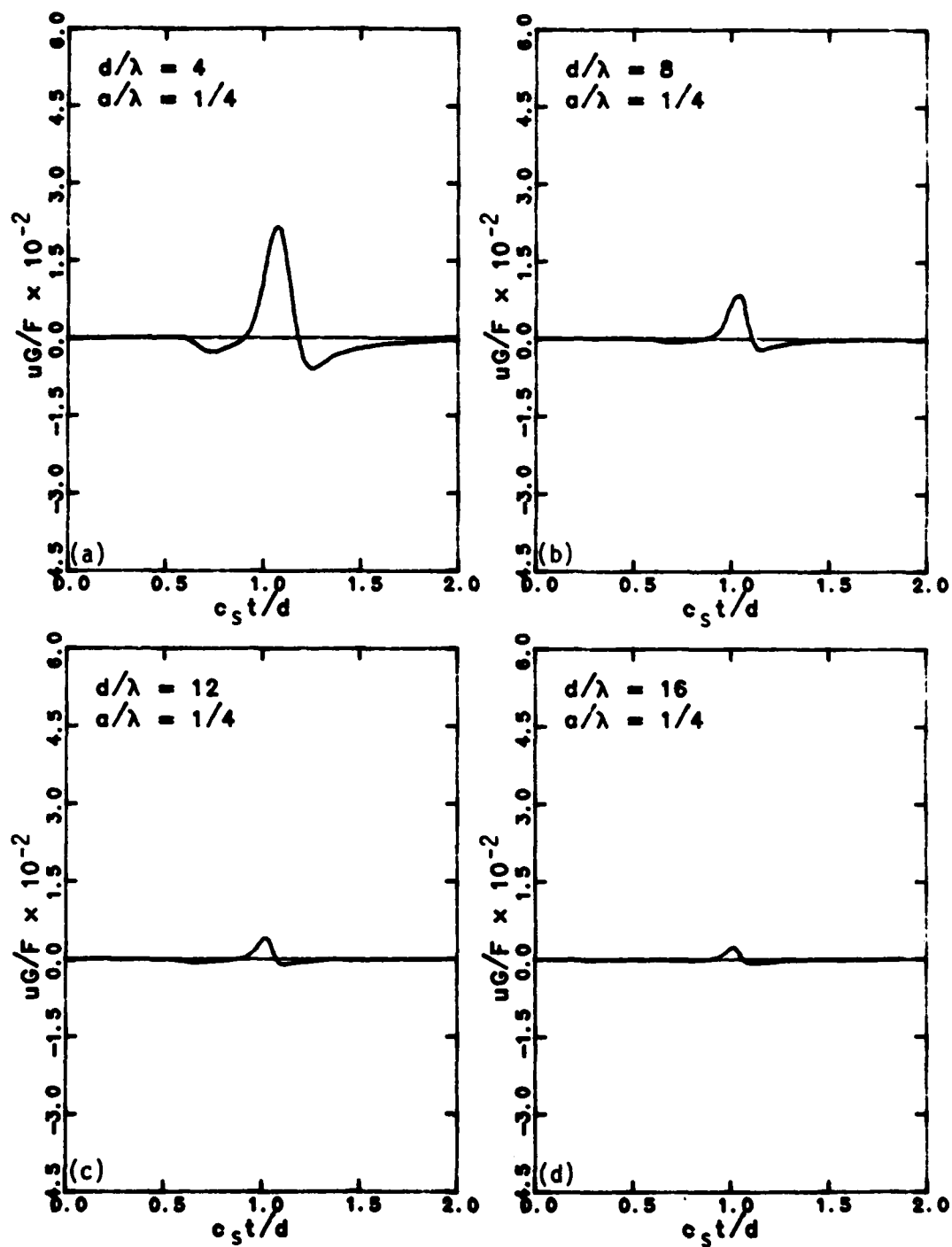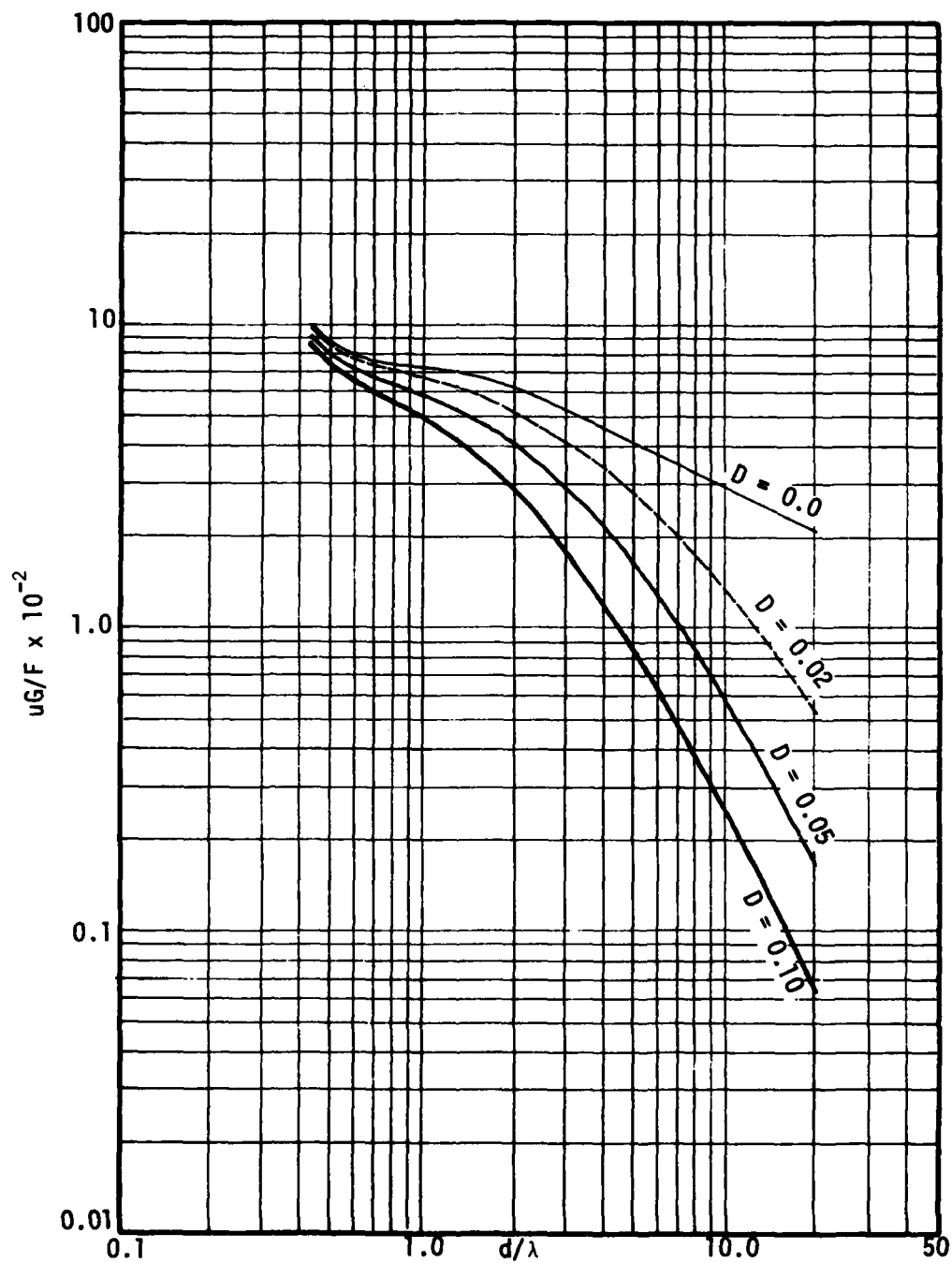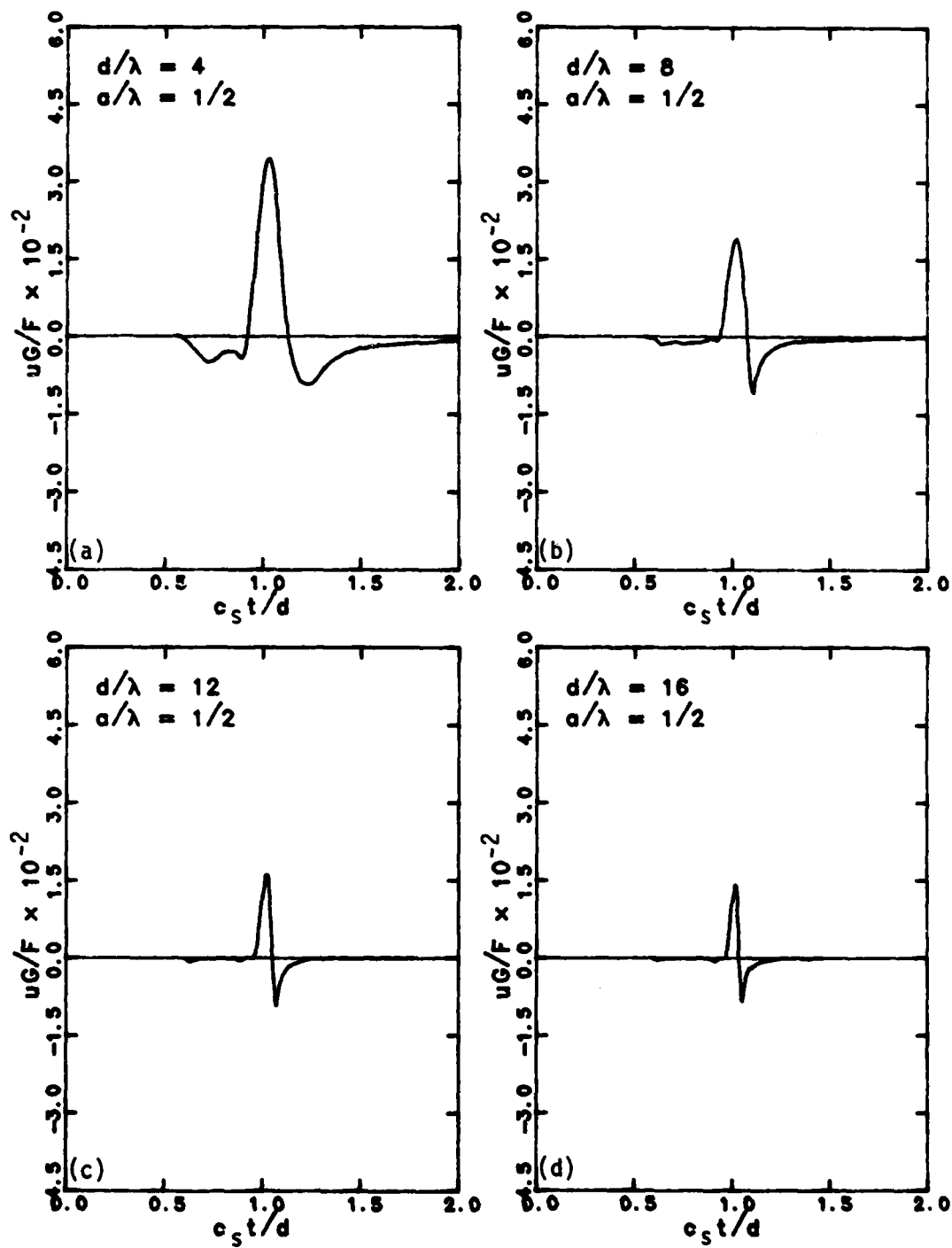
Figure 6.20 - 2-D Attenuation, One Inclusion, a/λ = 1/8

Figure 6.21 - 2-D Displacement, One Inclusion, a/λ = 1/4, D = 0.0

$d/\lambda = 4$
$a/\lambda = 1/4$

$uG/F \times 10^{-2}$

(a)

$c_s t/d$

$d/\lambda = 8$
$a/\lambda = 1/4$

$uG/F \times 10^{-2}$

(b)

$c_s t/d$

$d/\lambda = 12$
$a/\lambda = 1/4$

$uG/F \times 10^{-2}$

(c)

$c_s t/d$

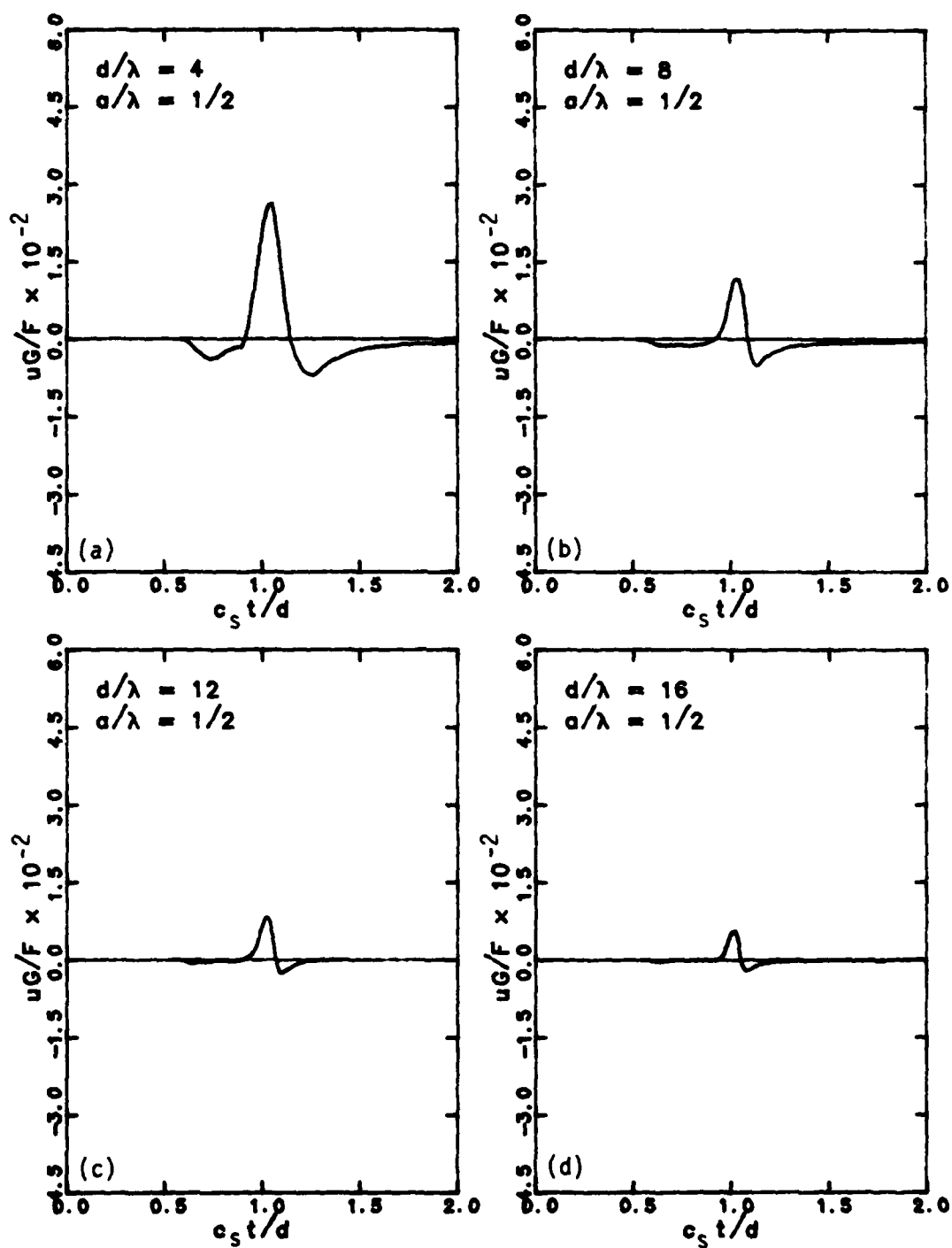$d/\lambda = 16$
$a/\lambda = 1/4$

$uG/F \times 10^{-2}$

(d)

$c_s t/d$

Figure 6.22 - 2-D Displacement, One Inclusion, $a/\lambda = 1/4$, D = 0.02

Figure 6.23 - 2-D Displacement, One Inclusion, a/λ = 1/4, D = 0.05

Figure 6.24 - 2-D Attenuation, One Inclusion, a/λ = 1/4

114

Figure 6.25 - 2-D Displacement, One Inclusion, $a/\lambda = 1/2$, $D = 0.0$

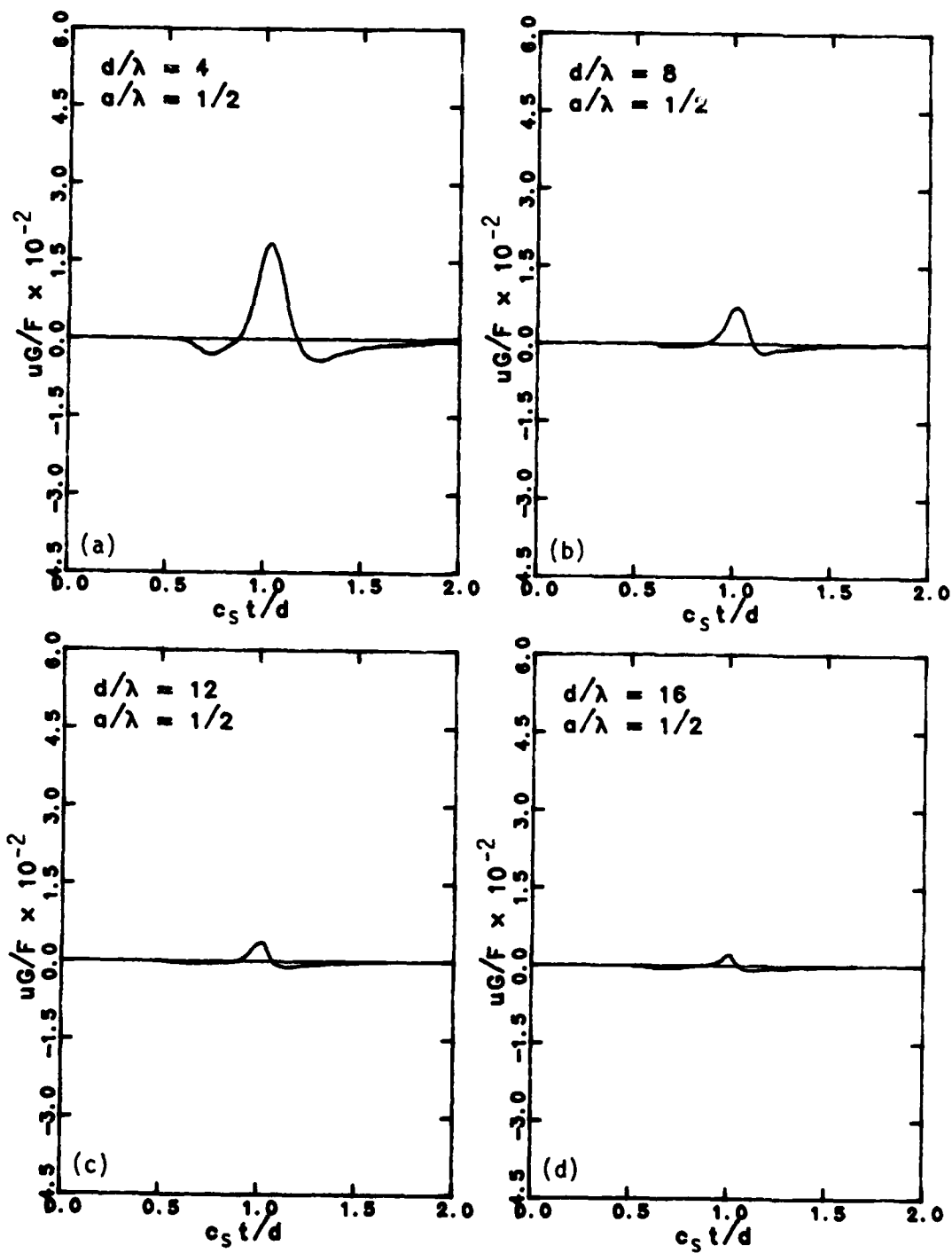Figure 6.26 - 2-D Displacement, One Inclusion, $a/\lambda = 1/2$, $D = 0.02$

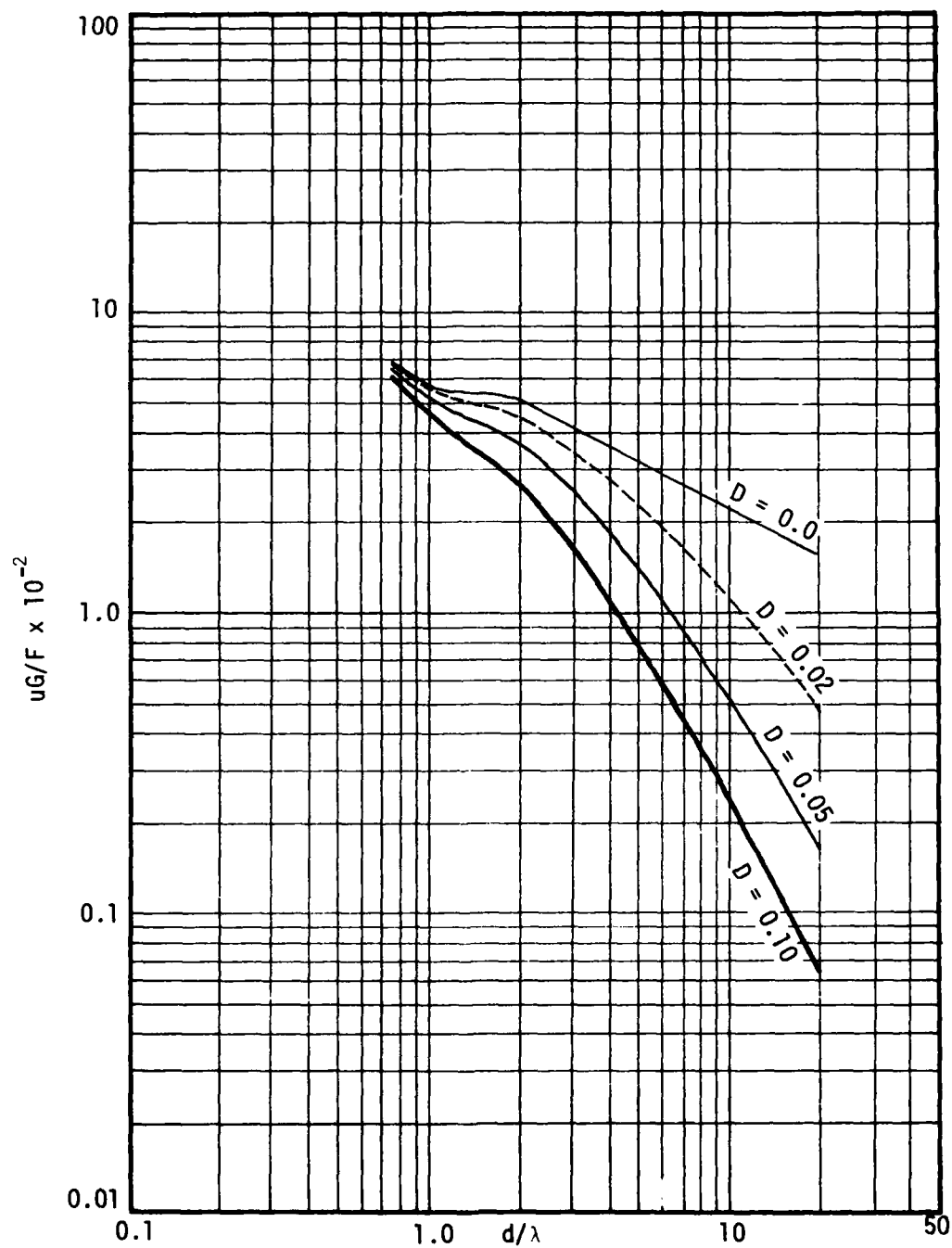Figure 6.27 - 2-D Displacement, One Inclusion, $a/\lambda = 1/2$, D = 0.05

Figure 6.28 - 2-D Attenuation, One Inclusion, $a/\lambda = 1/2$

slightly increases with the inclusion size and for each size, this period also increases with soil damping as in the free field.

The ratios of the peak amplitude between the case with an inclusion and the free field case are plotted against d/λ for all three sizes of inclusion (a/λ of 1/8, 1/4, and 1/2). These plots are shown in Figures 6.29, 6.30, 6.31, and 6.32 for the damping ratios D of 0.0, 0.02, 0.05, and 0.10 respectively. All plots show that the presence of an inclusion on the travelling path of the wave will reduce the wave amplitude. This reduction effect is more pronounced with larger inclusion size. When there is no soil damping the reduction in amplitude is almost constant in the range d/λ from 2 to 20. These reductions are about 35, 15, and 5 percent for a/λ of 1/2, 1/4, and 1/8 respectively as shown in Figure 6.29. As soil damping increases, the amplitude reduction decreases especially at large distance as shown in Figures 6.30 to 6.32. The amplitude ratios A/A_f approach the same value as d/λ increases. In all cases, the maximum reduction in amplitude occurs at the distance about 1.25 of the wavelength λ

6.2.2   Three-Dimensional Case

The displacement versus time curves for the case with one cubic inclusion having a side dimension to wavelength ratio $a/\lambda = 1/8$ are shown in Figures 6.33, 6.34, and 6.35 for damping ratios of 0.0, 0.02, and 0.05 respectively. In order to keep the computation cost within a reasonable limit, the truncation of the transfer function was made at a slightly
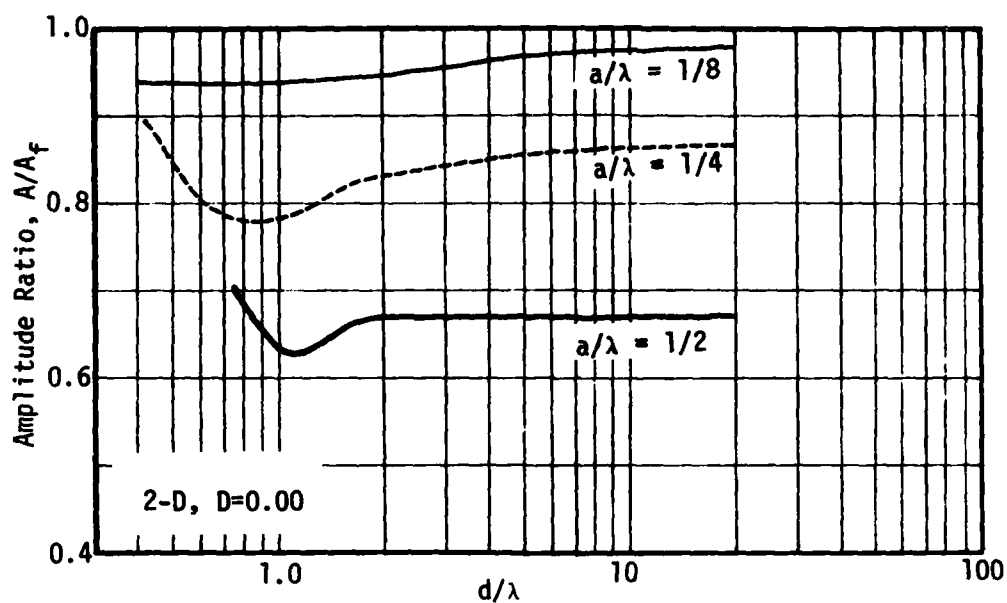
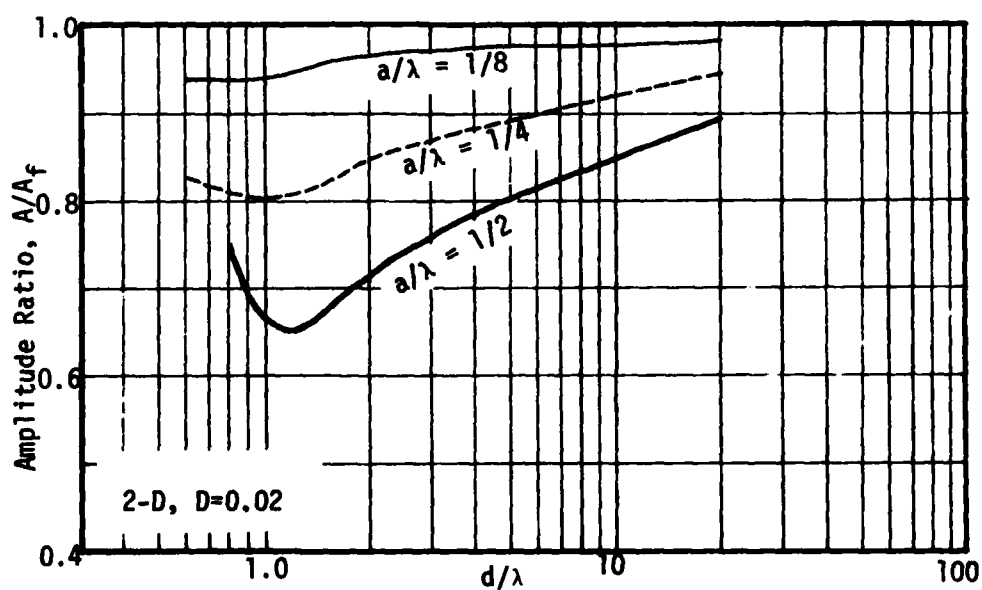Figure 6.29 - Amplitude Ratios between Cases with Inclusion and
Free Field, D = 0.00, 2-D

Figure 6.30 - Amplitude Ratios between Cases with Inclusion and
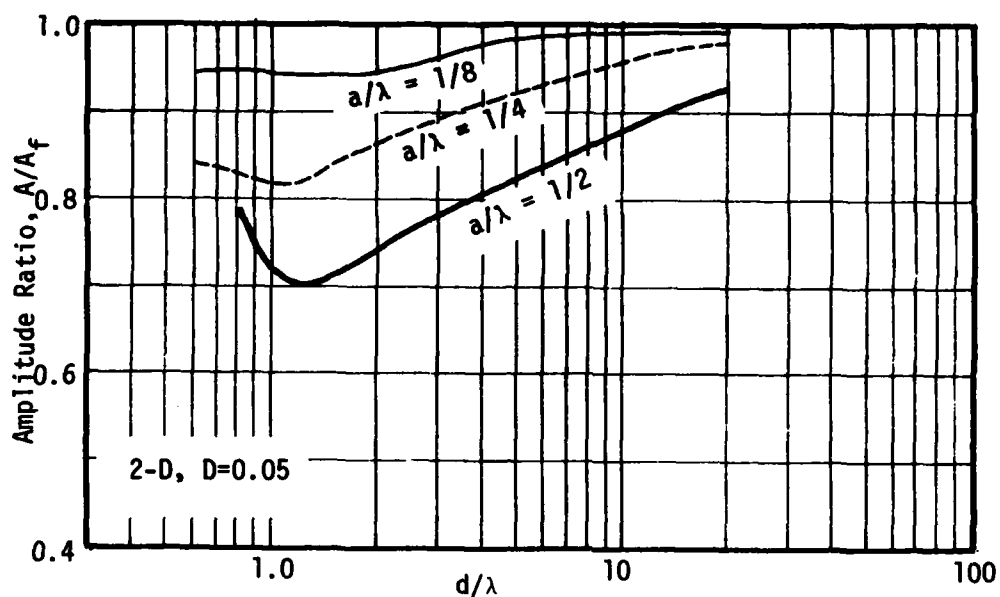Free Field, D = 0.02, 2-D

120

Figure 6.31 - Amplitude Ratios between Cases with Inclusion and
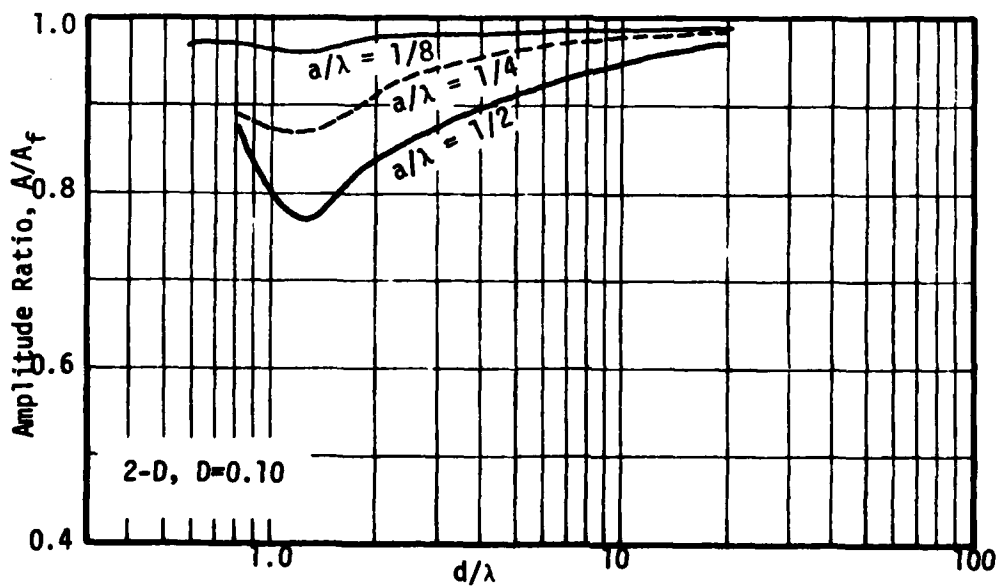Free Field, D = 0.05, 2-D

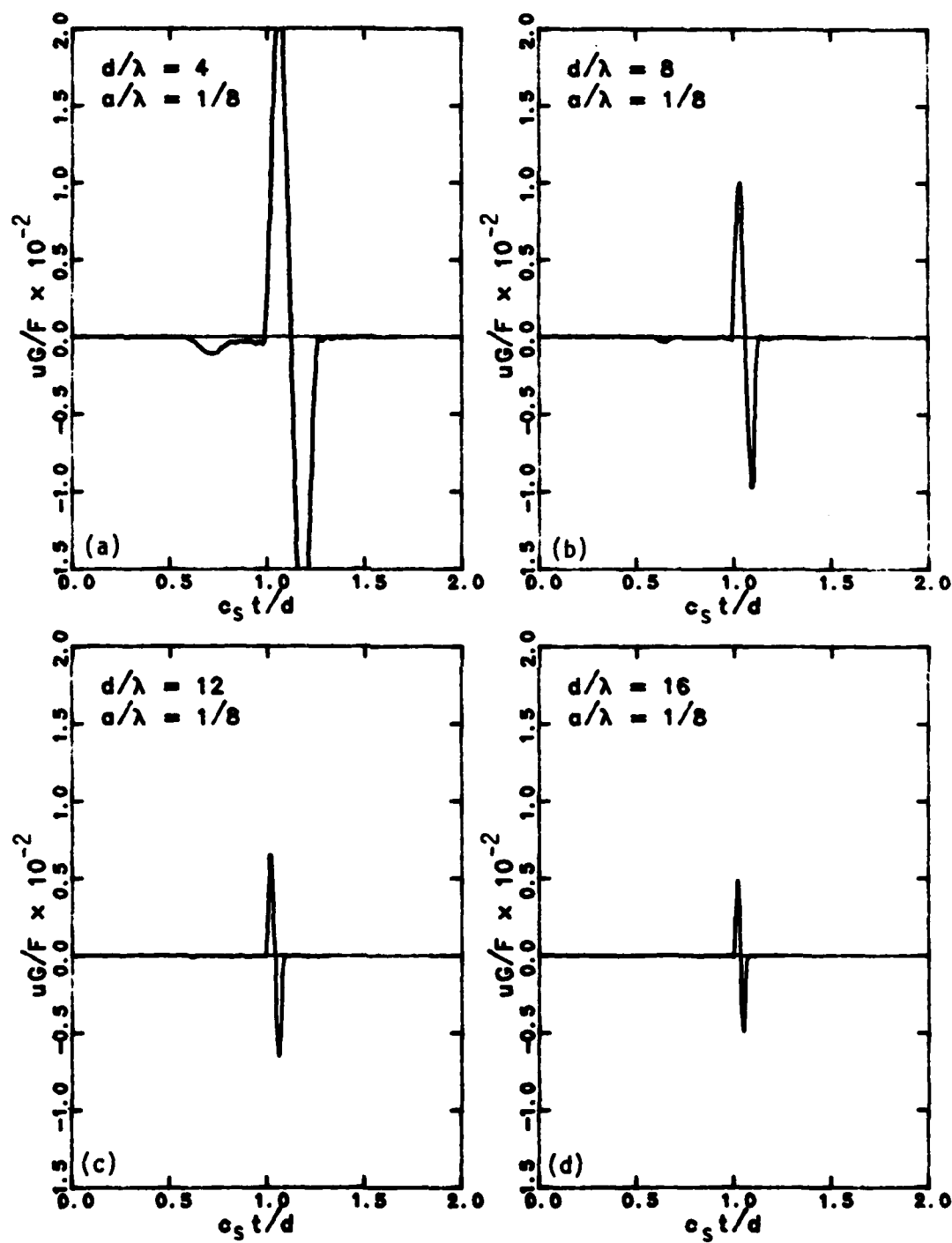Figure 6.32 - Amplitude Ratios between Cases with Inclusion and
Free Field, D = 0.10, 2-D

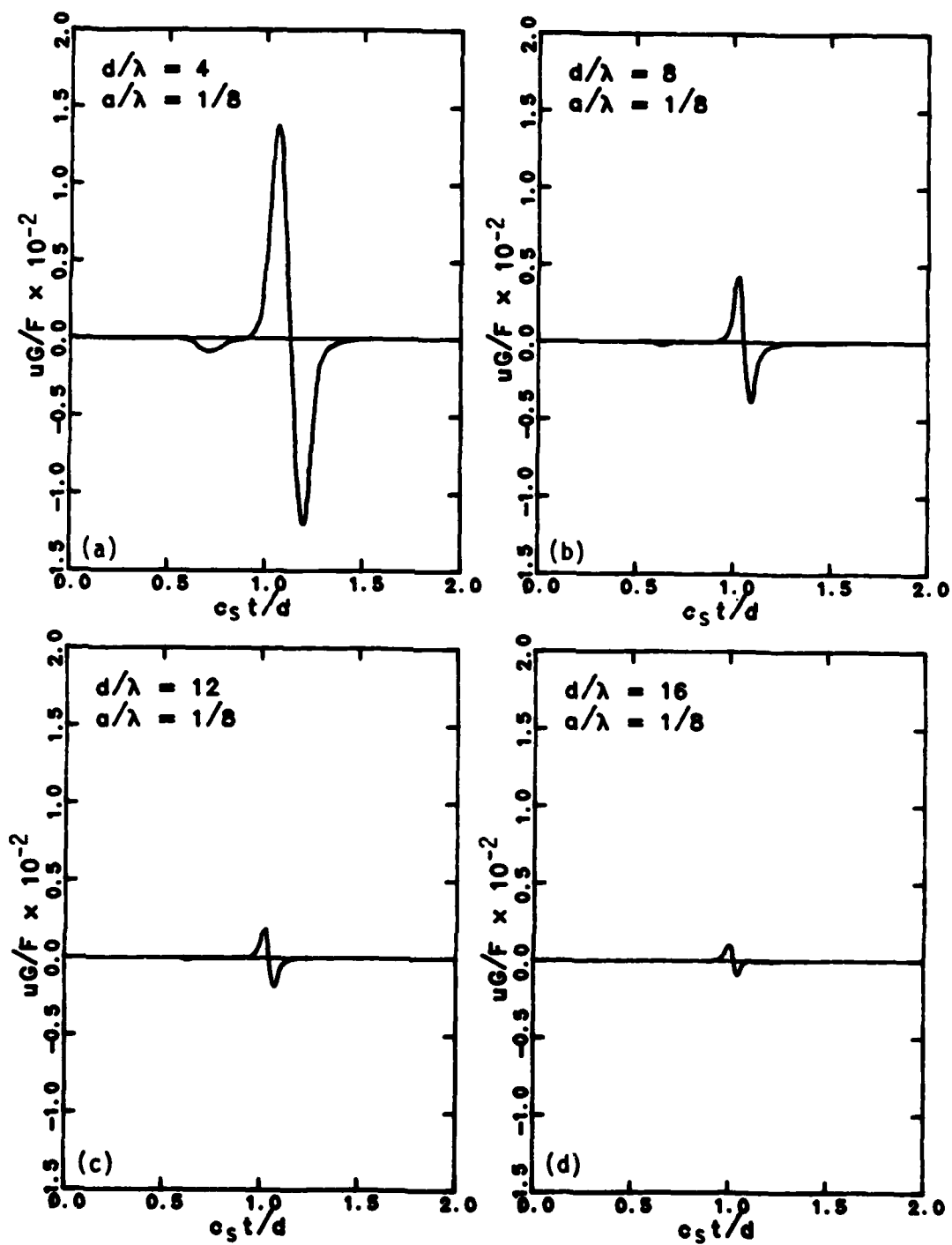Figure 6.33 - 3-D Displacement, One Inclusion, a/λ = 1/8, D = 0.0

Figure 6.34 - 3-D Displacement, One Inclusion, a/λ = 1/8, D = 0.02
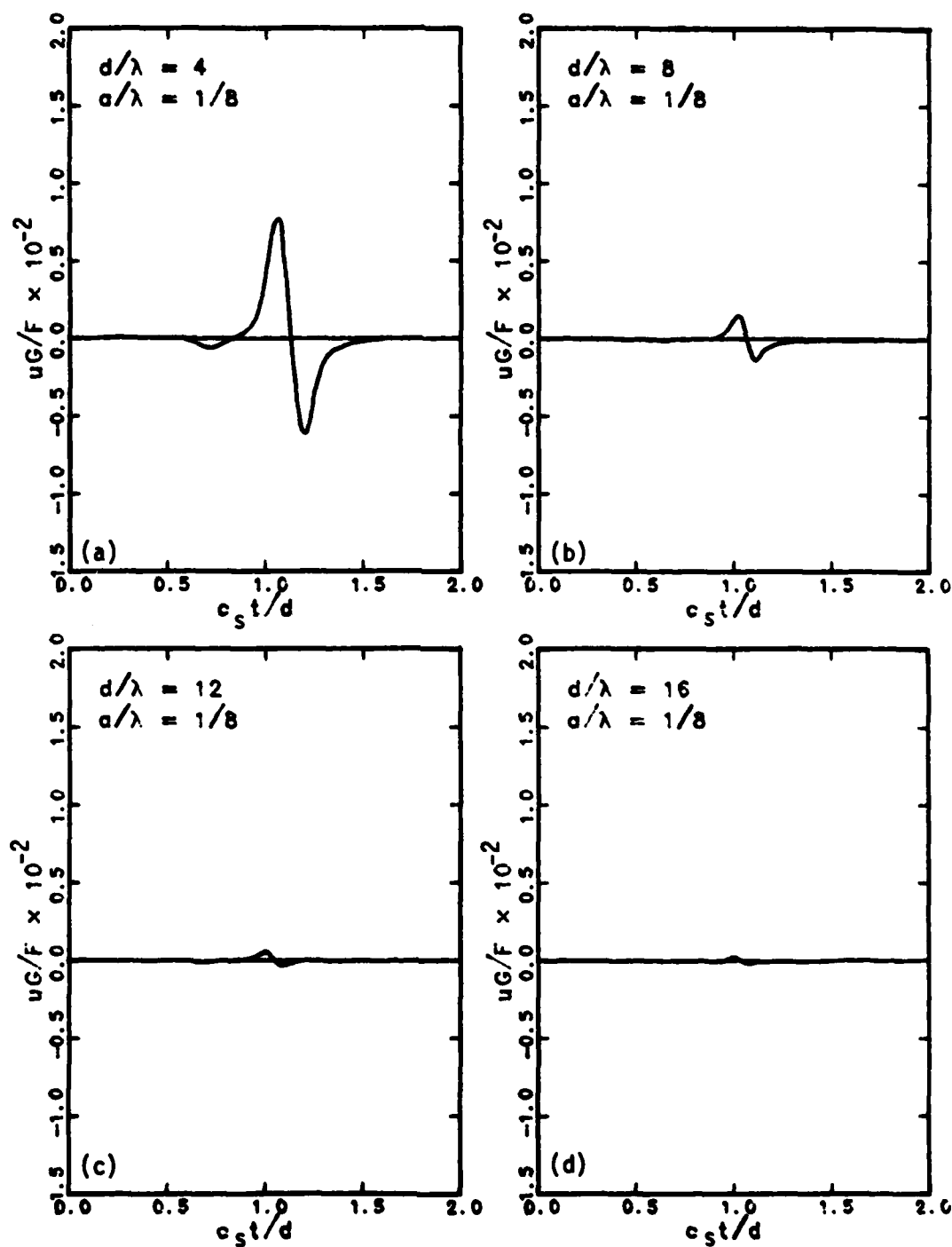
Figure 6.35 - 3-D Displacement, One Inclusion, a/λ = 1/8, D = 0.05

lower frequency than required to obtain a smooth curve. This only causes a slight irregularity on some portions of the displacement curve in the case without damping, as shown in Figure 6.33, while no significant accuracy is sacrificed. In the case with damping, most of the higher frequency components are, however, going to be damped out, and the truncation of the transfer function at a slightly lower frequency has, therefore, no significant effects of the smoothness of the results.

Except for the less smooth curve due to the truncation effect as mentioned, there are no significant differences between the results above and the free field results shown in Figures 6.11 to 6.13, which indicates that this size of inclusion (a/λ = 1/8) is too small to have any significant effects. The attenuation curves for this case (Figure 6.36) are, therefore, almost identical to those of the free field (Figure 6.16).

When the inclusion size is doubled (a/λ = 1/4), the peak amplitude decreases slightly as shown in Figures 6.37 and 6.38 for the case with damping ratios of 0.0 and 0.02 respectively. With damping ratios of 0.05, shown in Figure 6.39, the amplitude decrease can be detected only at close distances (d/λ of 4 to 8) beyond which the amplitude are all the same with the case a/λ = 1/8 and the free field case. This indicates a larger effect of the inclusion with closer targets and less soil damping. Figure 6.40 shows the corresponding attenuation curve which is still basically a straight line in the case D = 0.0.

In the results shown in Figure 6.41, the size of the inclusion is further increased (a/λ = 1/2). Because of the limit in the computer sto-

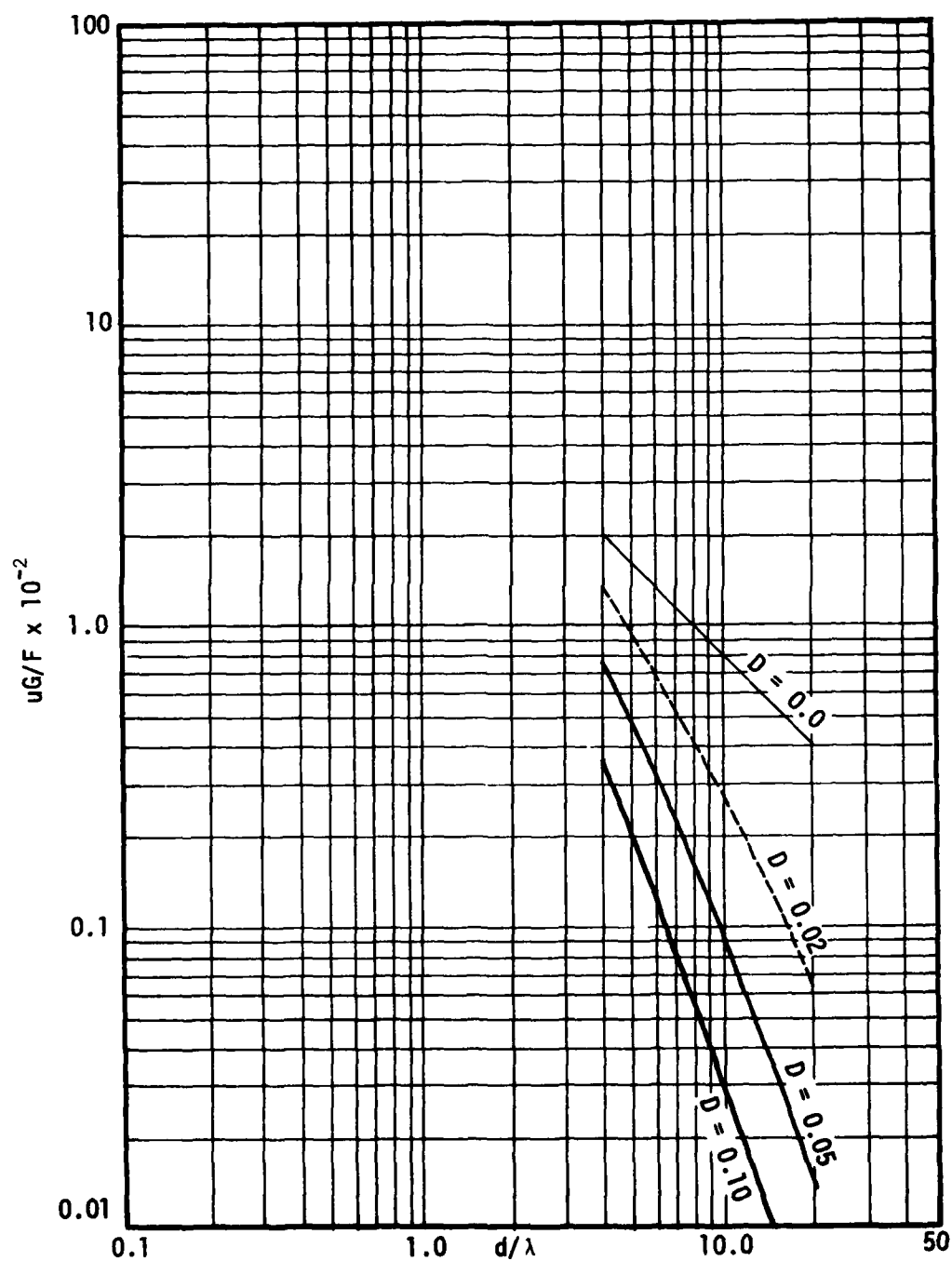Figure 6.36 - 3-D Attenuation, One Inclusion, a/λ = 1/8

Figure 6.37 - 3-D Displacement, One Inclusion, a/λ = 1/4, D = 0.0

Figure 6.38 - 3-D Displacement, One Inclusion, a/λ = 1/4, D = 0.02

128

Figure 6.39 - 3-D Displacement, One Inclusion, a/λ =1/4, D = 0.05
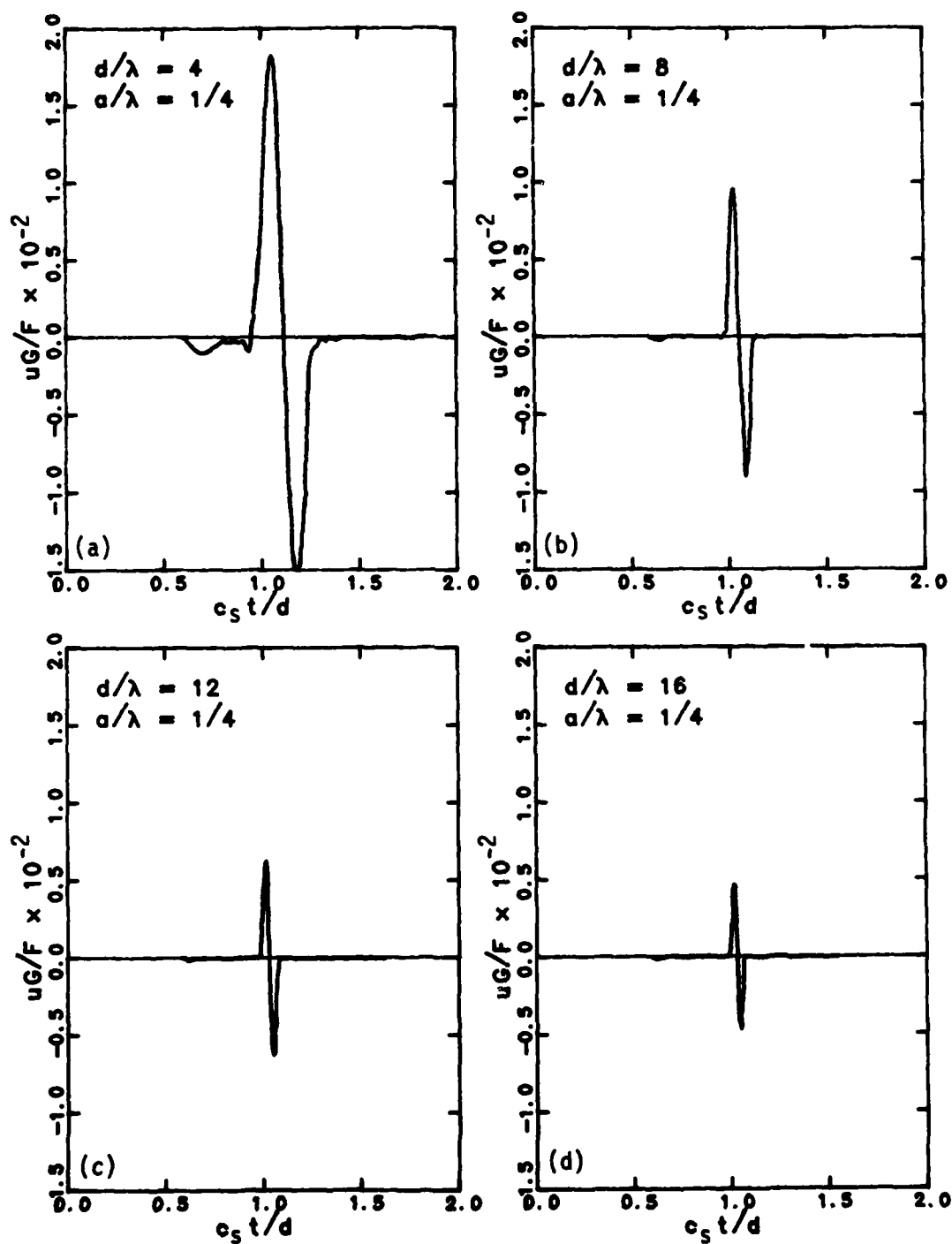
Figure 6.40 - 3-D Attenuation, One Inclusion, $a/\lambda = 1/4$

130

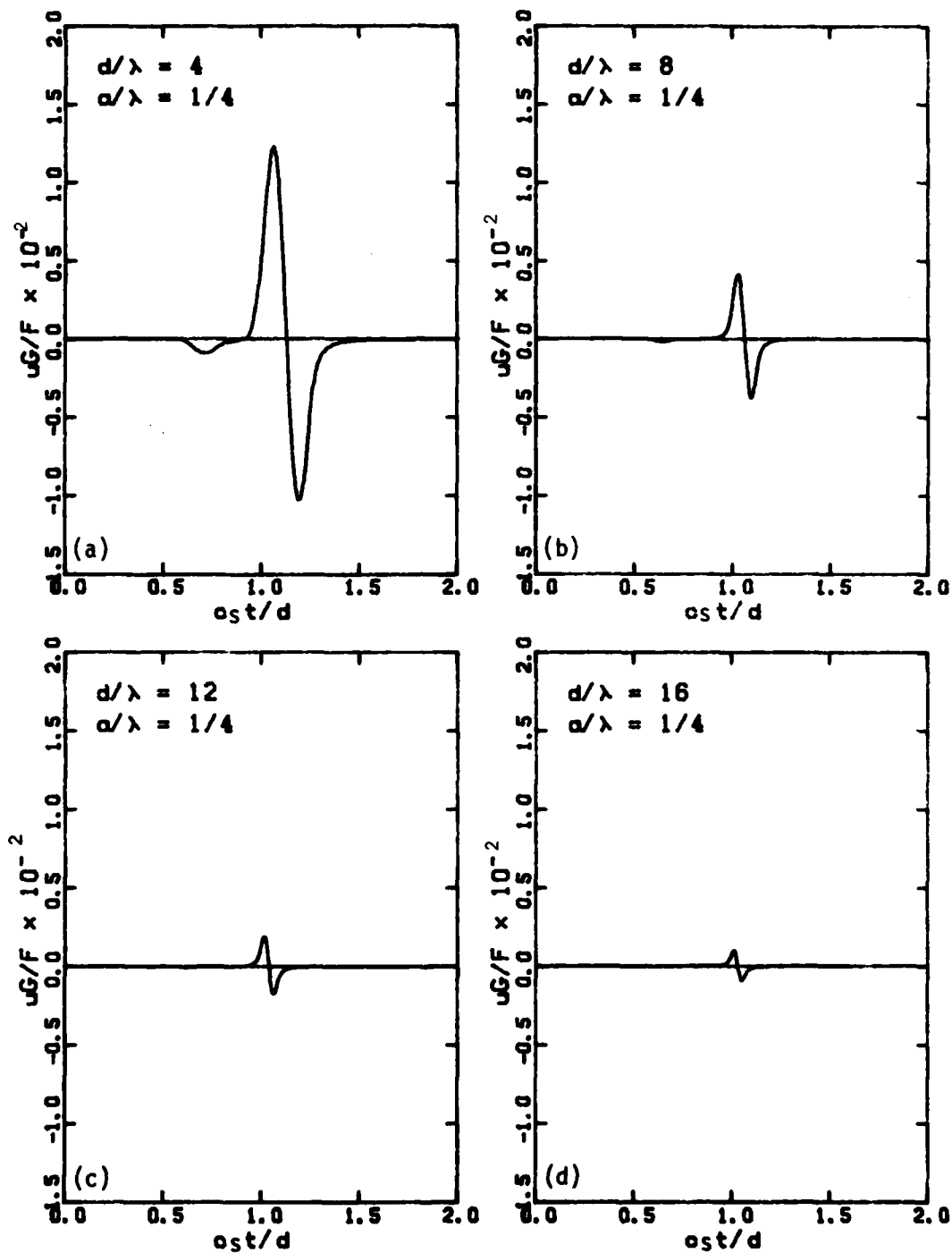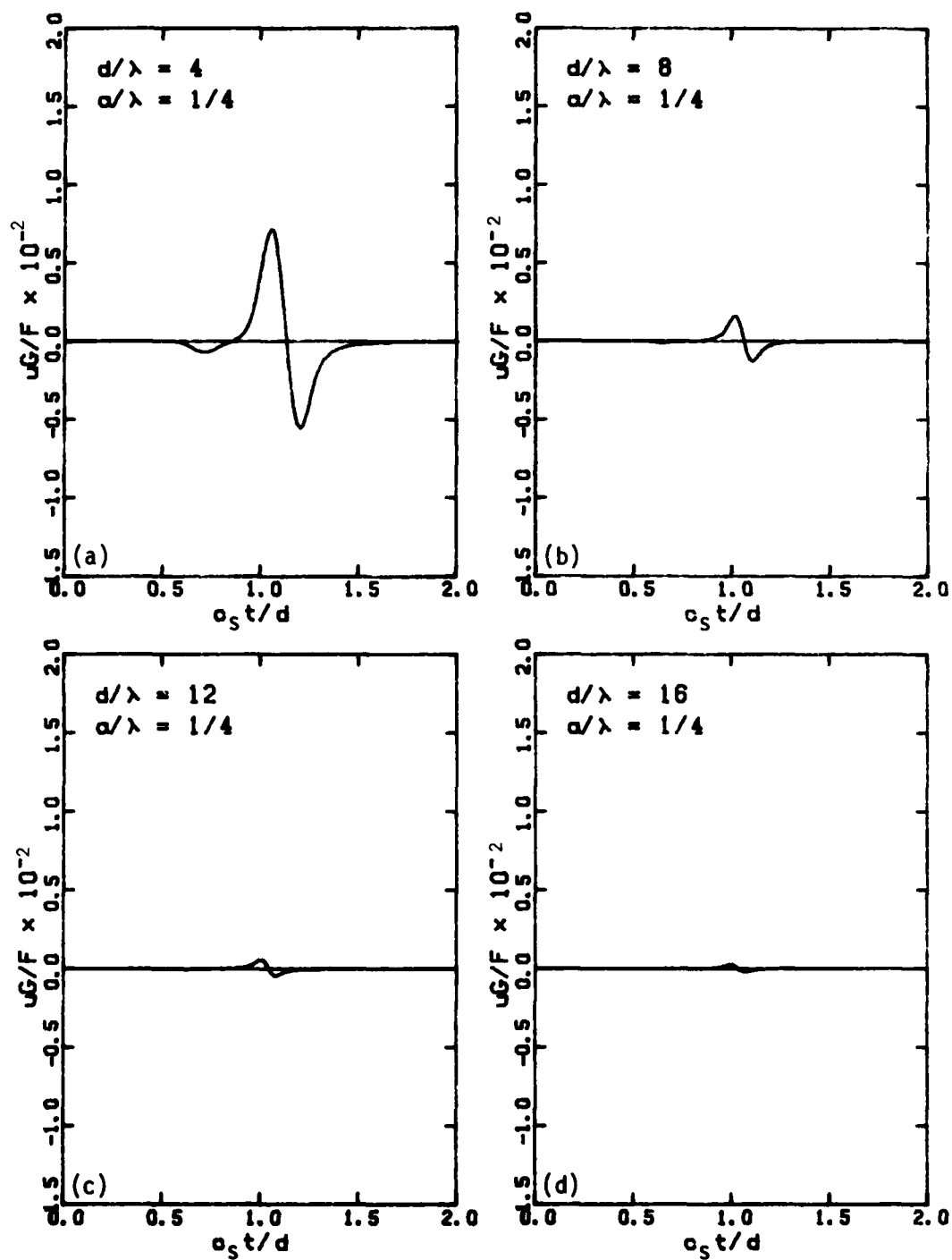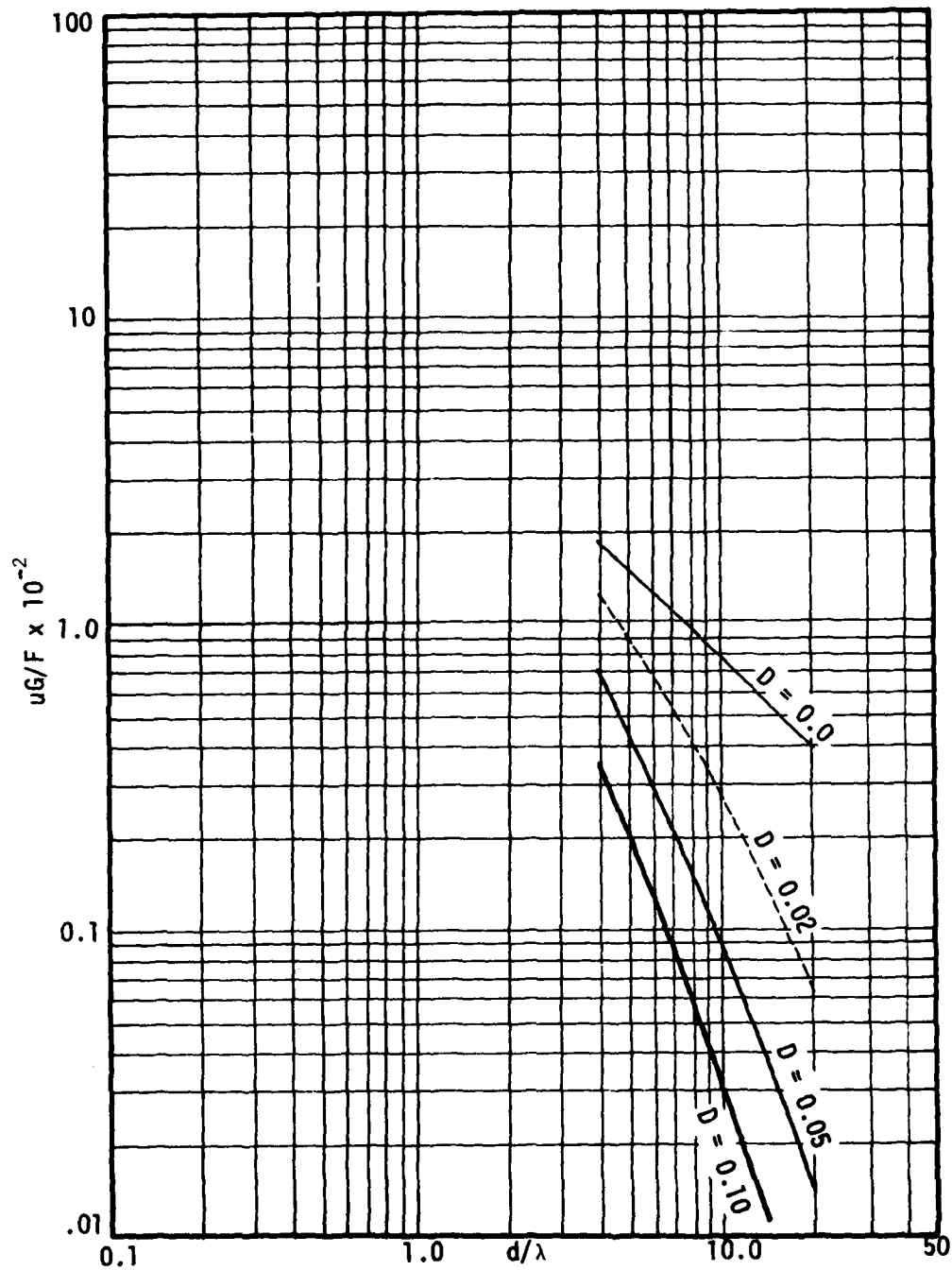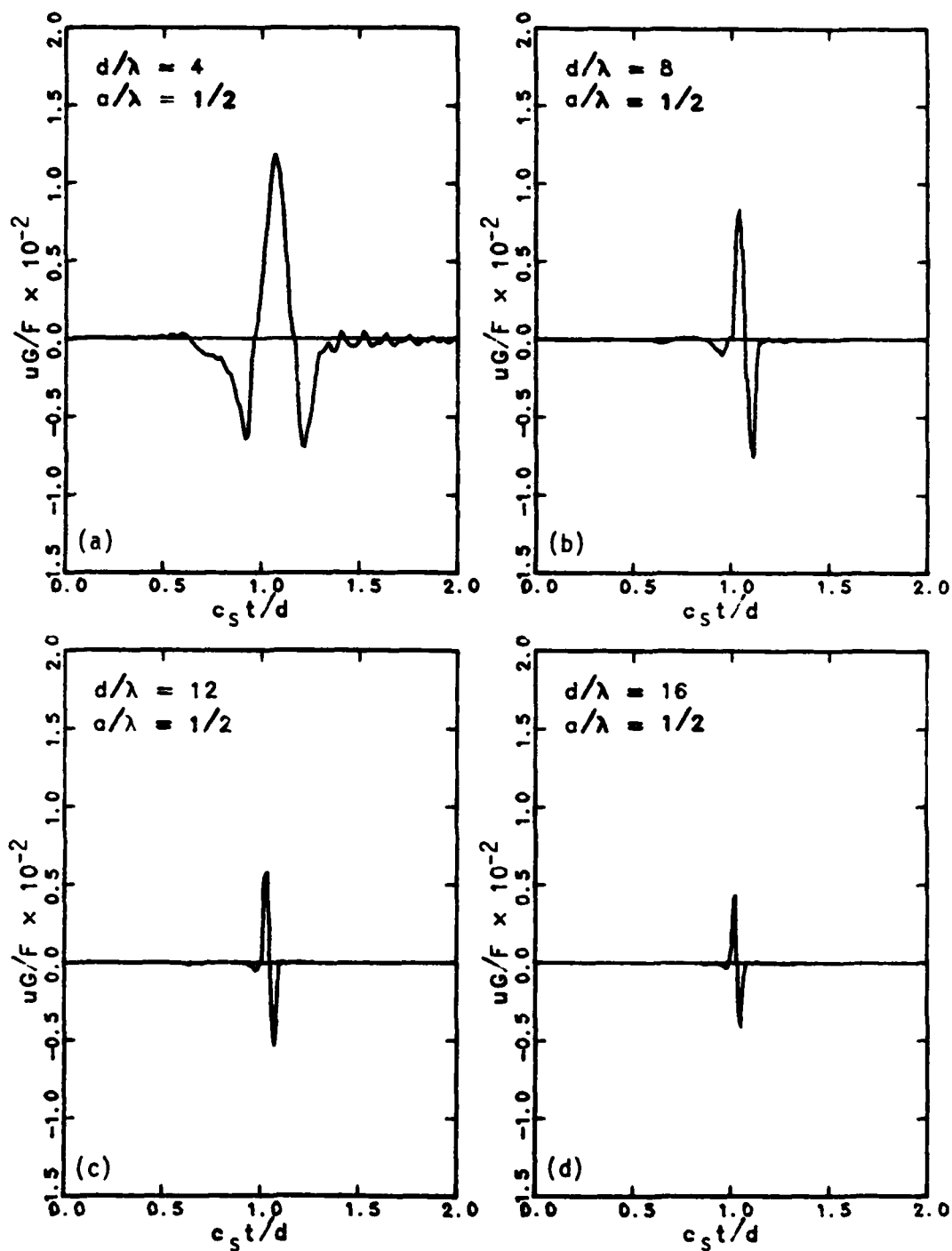Figure 6.41 - 3-D Displacement, One Inclusion, $a/\lambda = 1/2$, $D = 0.0$

rage available, the number of degrees of freedom had of be kept small by using larger elements which are below the limit required for accuracy. The side dimension of the boundary element used in this case is $\lambda/4$ instead of $\lambda/8$ as usual. The results, as expected, are not as accurate especially when the target point is close to the inclusion as shown in the curve when $d/\lambda = 4$. Despite the loss in accuracy, the results still indicate a larger amplitude reduction in the closer range target.

The ratios of the peak amplitude between the case with an inclusion and the free field case are plotted against d/λ in the same manner as in the two-dimensional case for a/λ of 1/8 and 1/4. These results are shown in Figures 6.42 to 6.45 for damping ratios of 0.0 to 0.10 respectively. For $a/\lambda = 1/8$, there is no reduction in amplitude except in the case without damping which shows a decrease in amplitude of about 2 percent at $d/\lambda = 4$, down to 1 percent at $d/\lambda = 20$. With larger inclusion size ($a/\lambda = 1/4$), the reduction is more evident. This reduction, however, decreases with the larger distance d/λ and larger damping ratio D. With the damping ratio $D = 0.10$, there is no reduction in amplitude at all distance ranges studied as shown in Figure 6.45.

The above results, as compared to the two-dimensional case, reveals that the amplitude reduction is caused more by the soil damping than by the presence of an inclusion. This explains why there are no differences in the results between the free field and the case with inclusion when the damping ratio increases.

132

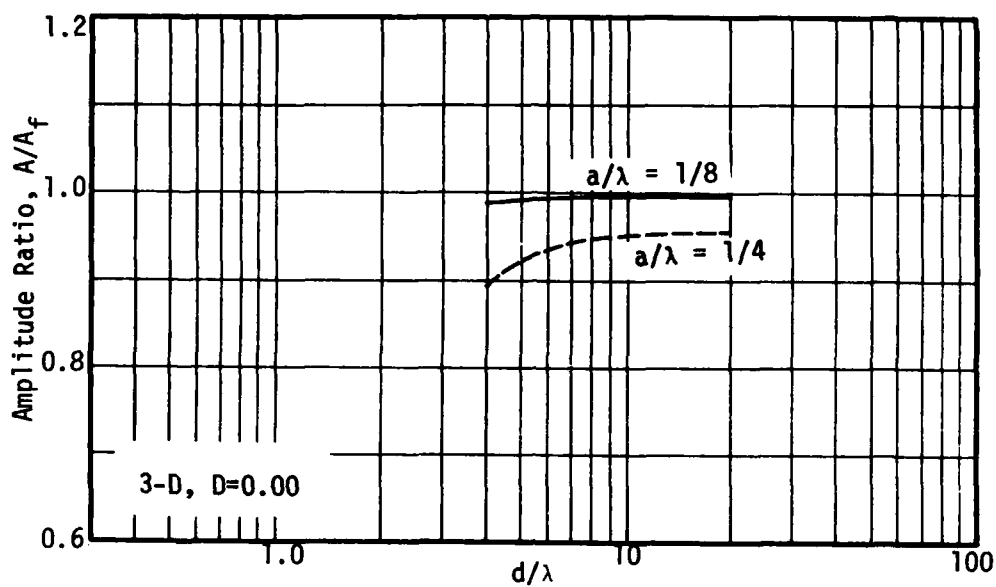
Figure 6.42 - Amplitude Ratios between Cases with Inclusion and
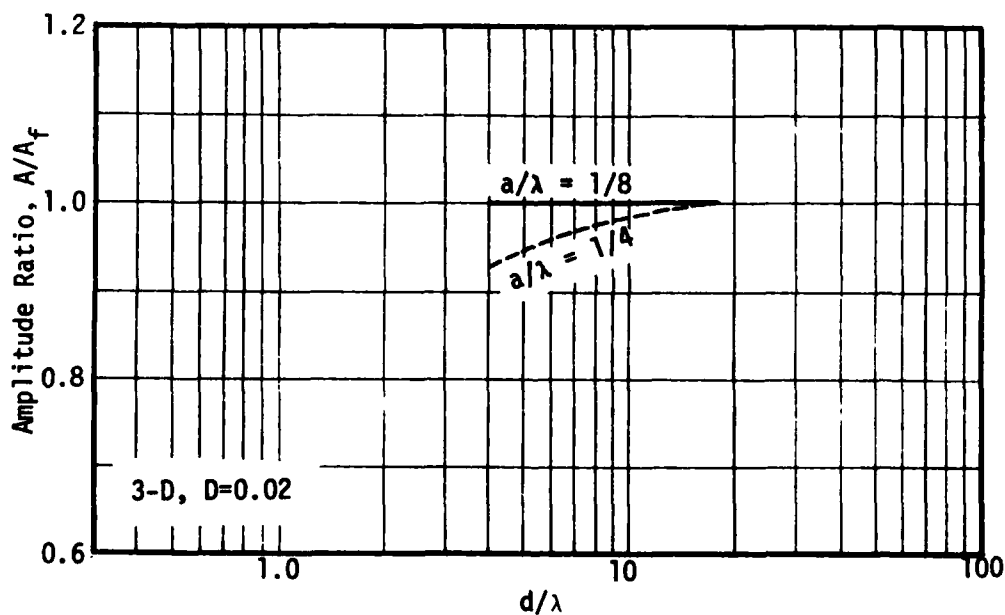Free Field, D = 0.00, 3-D

Figure 6.43 - Amplitude Ratios between Cases with Inclusion and
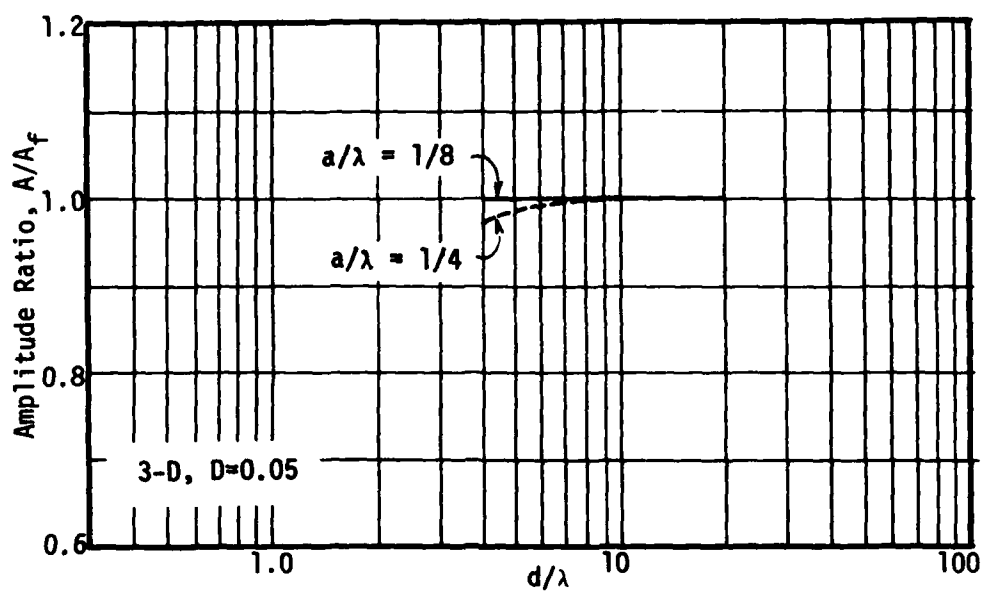Free Field, D = 0.02, 3-D

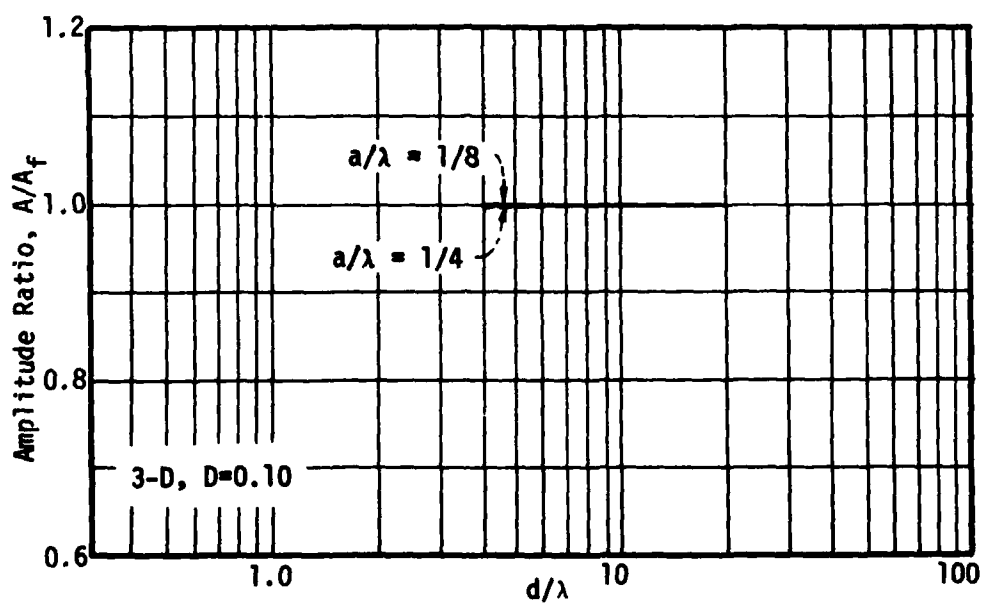Figure 6.44 - Amplitude Ratios between Cases with Inclusion and
Free Field, D = 0.05, 3-D

Figure 6.45 - Amplitude Ratios between Cases with Inclusion and
Free Field, D = 0.10, 3-D

6.3 EFFECT OF THE MASS AND STIFFNESS OF AN INCLUSION

Only the stiffness and inertia of the inclusion which are the essential system properties for the transmission of wave motion, are investigated in this section. The inclusion considered here is a square with the size parameter $a/\lambda = 1/8$. Two sets of results are presented. In the first set, the inclusion is 100 times stiffer than the medium ($c_{sb}/c_s = 10$), while in the second set, the inclusion is softer than the medium ($c_{sb}/c_s = 0.5$). In each set, the unit mass ratios between the inclusion and the medium are 0.5, 1.0, and 5.0.

Figure 6.46 shows the plots of amplitude versus distance in log-log scale for the case of the stiff inclusion. The plots show a slightly higher amplitude with the higher unit mass ratio. The rate of amplitude attenuation is, however, the same.

In the case of an inclusion that is softer than the medium, the effect of the inclusion unit mass on the amplitude and the attenuation characteristics are the same as in the case of a stiff inclusion; but, the increase in amplitude with the unit mass ratio is slightly larger as can be seen in Figure 6.47. By comparing this figure to Figure 6.46, it can be noticed that, for the same unit mass ratio, the case of a stiffer inclusion shows a slightly smaller amplitude than the soft inclusion.
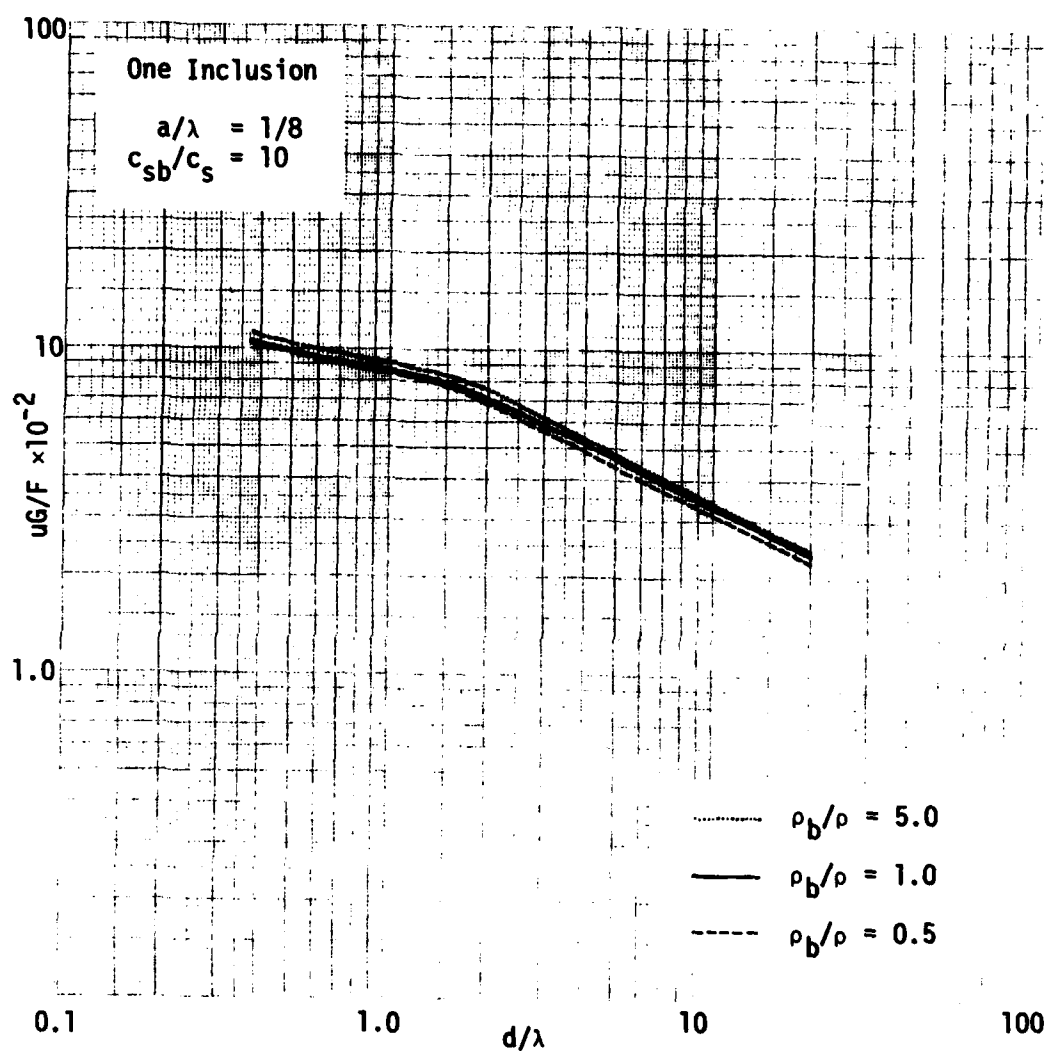
Figure 6.46 - Effect of the Unit Mass of the Inclusion, Stiff
Inclusion
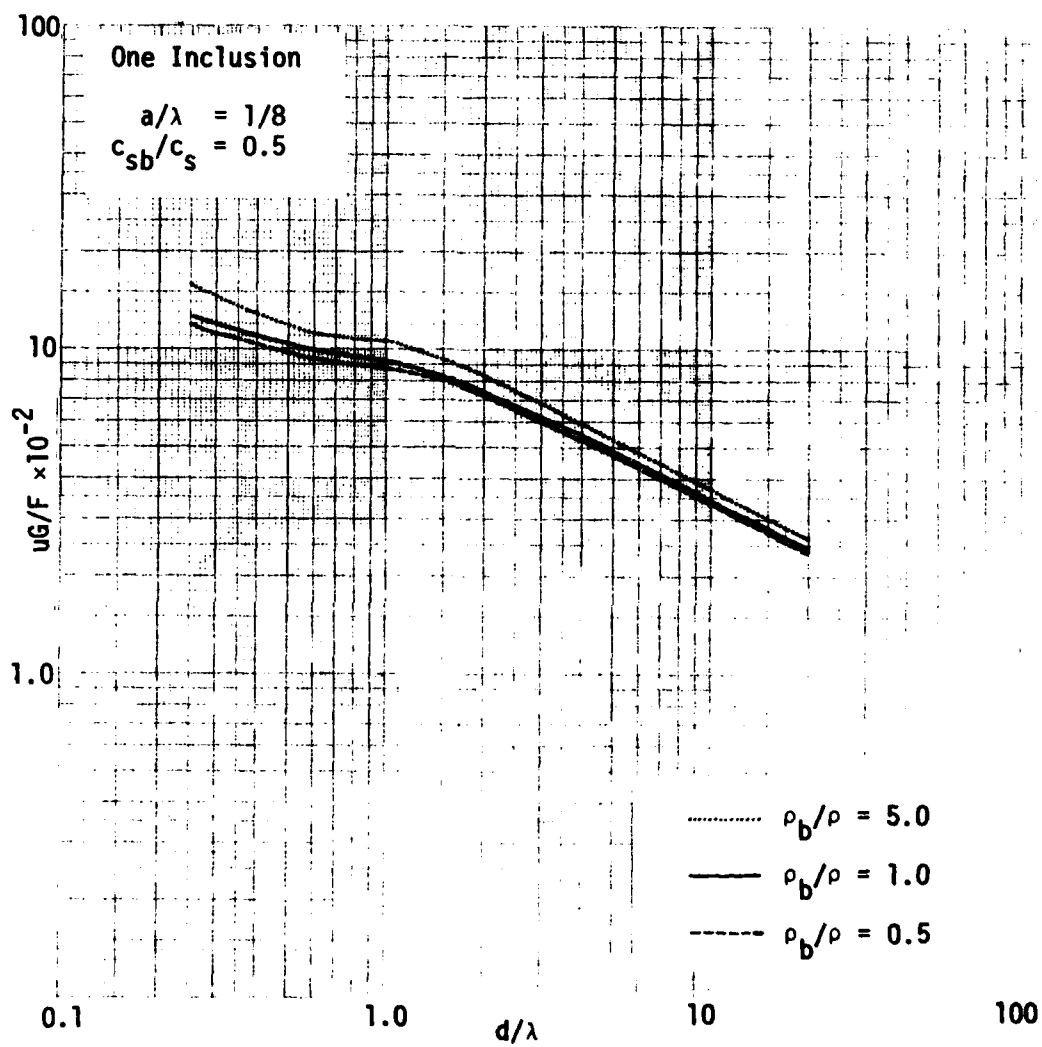
Figure 6.47 - Effect of the Unit Mass of the Inclusion, Soft
Inclusion

CHAPTER 7

EFFECT OF INCLUSIONS ON ARRIVAL TIME

Stress wave propagatiom techniques are often used in geotechni-
cal engineering for the exploration of soil deposits and determining
soil moduli in the field from measurements of wave velocities. In a non-
homogeneous medium or a medium with inclusions having different proper-
ties, such as an alluvial deposit, the velocity of the propagating wave
would be different depending on a complicated dynamic interaction
between the medium and the inclusions. This interaction will be a func-
tion of the physical properties, shape, and size of the inclusions as
well as their number and their arrangement in the cluster. As mentioned
at the beginning of Chapter 6, extensive studies on these factors involve
a considerable expense and time. Consequently, only some major cases for
the two-dimensional model will be investigated and presented in this
chapter.

7.1 INTERPRETATION AND PRESENTATION OF THE ARRIVAL TIME

Since the arrival time is an interpreted value from the plots of
motion (which may be the displacement, velocity, or acceleration) versus
time, the interpretation method has to be consistent in order to have

reliable results. Although the determination of the wave propagation velocity from the interval travel time between two target points proves to be somewhat easier and more reliable than from the first arrival time at one location, the latter approach will be used here since the main point of interest in this work is the relative change of the wave velocity (or arrival time) with the presence of inclusions. As long as the method is consistent, the results should show the same inclusion effect.

The determination of the first arrival time of the shear wave using the displacement versus time trace for the case of a finite domain with a point force excitation (Suddhiprakarn, 1983) showed that the first arrival time could be either selected as the zero crossing point (when the positive motion starts), or the point where the major upward movement starts (as often used in experimental work). The differences in the shear wave velocity between the above two criteria is about five percent. To justify the accuracy of these two approaches for the case of an infinite medium using the boundary element method, the free field displacement for short range and long range targets are plotted together in Figure 7.1 and Figure 7.2 respectively. The dimensionless displacement and time defined in Chapter 6 are used, which leads to a different horizontal scale for curves of different targets depending on the target-source distance. The theoretical arrival time of the shear wave to all targets in the free field, however, will always correspond to a value of $c_s t/d$ of one.

The results for the close range targets in Figure 7.1, whose horizontal scale is highly enlarged show that the zero crossing point does
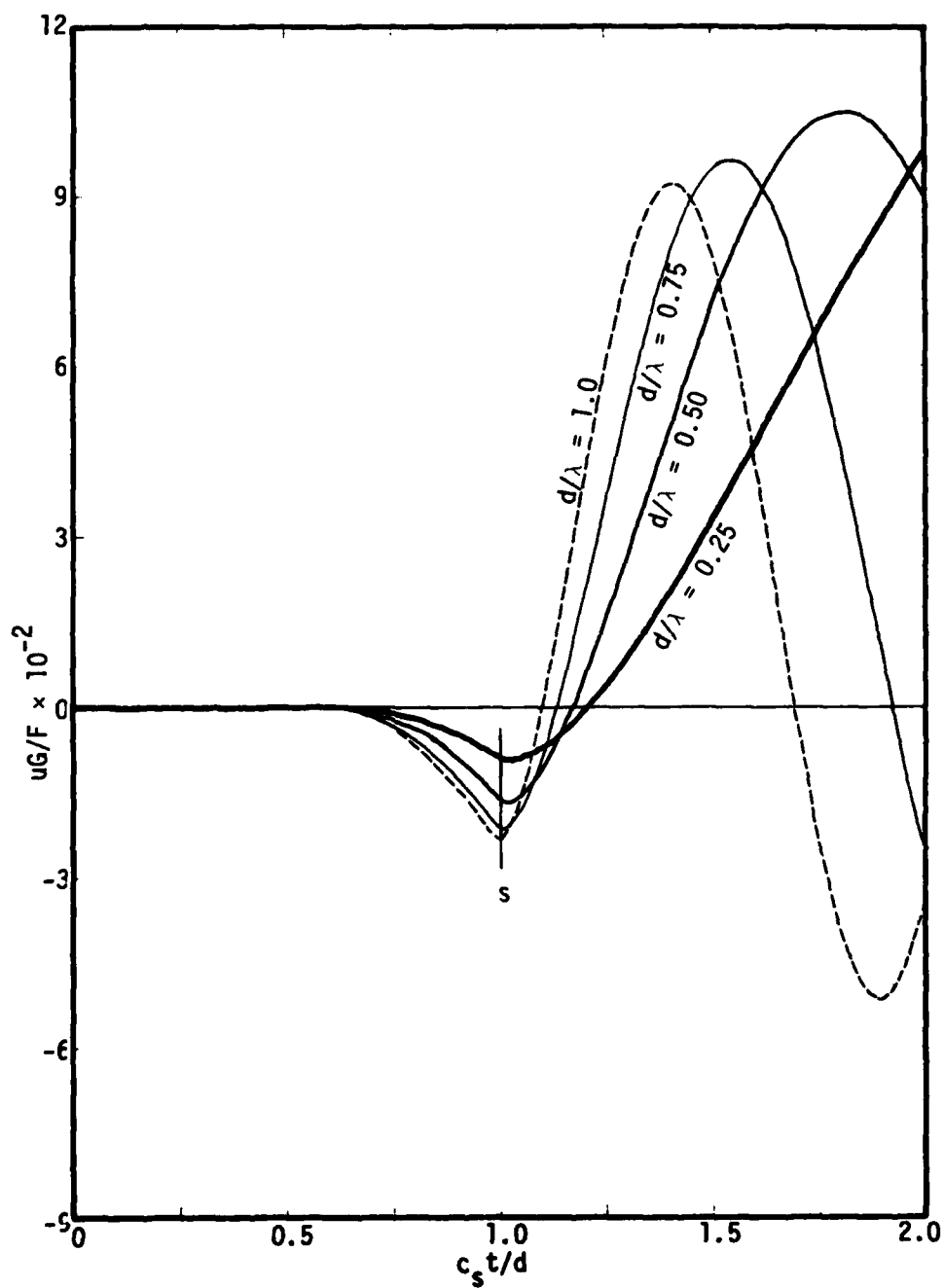
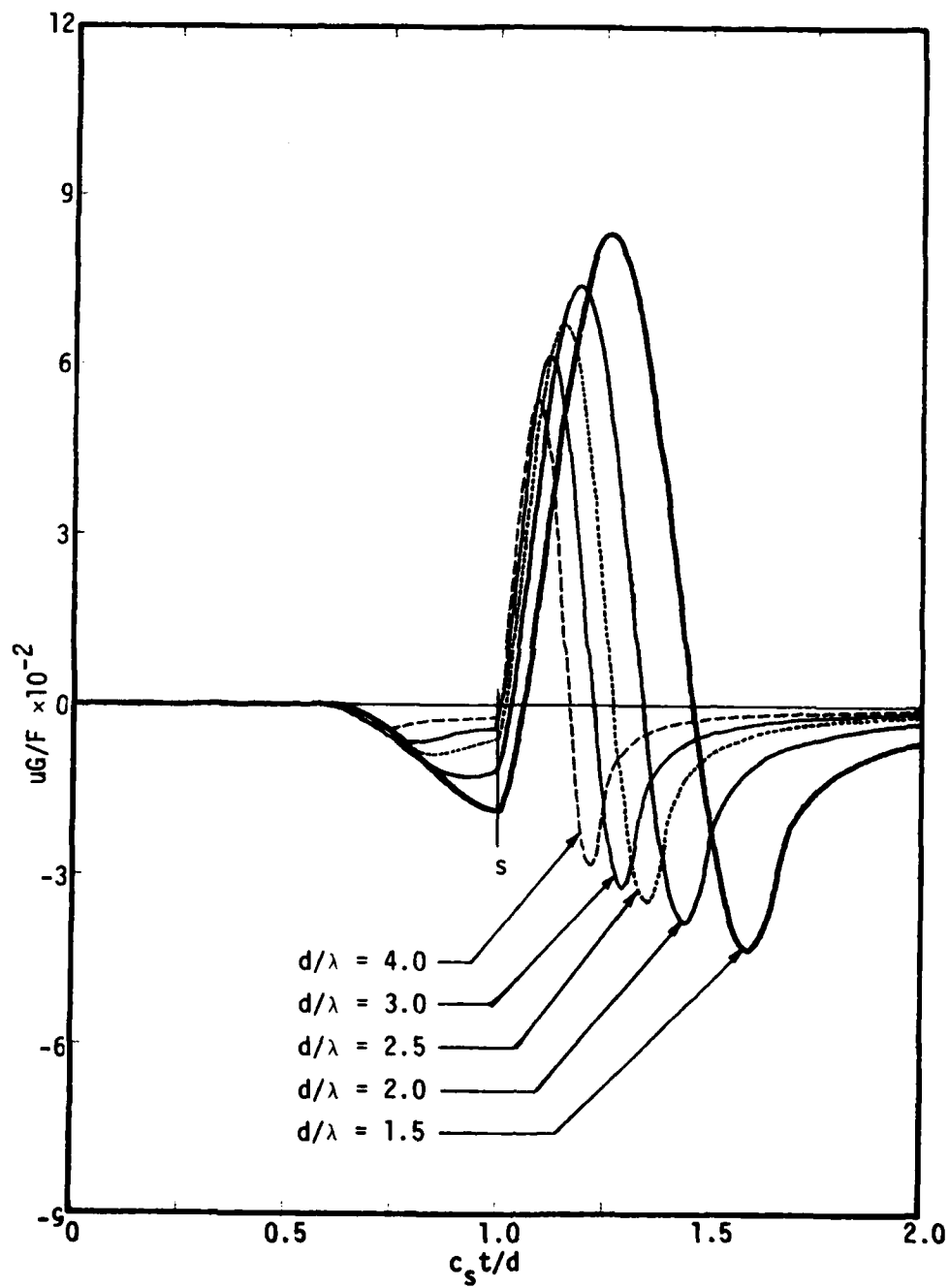Figure 7.1 - Free Field Displacement, Short Range, D = 0.0

140

Figure 7.2 - Free Field Displacement, Long Range, D = 0.0

not represent the first arrival time as well as the point where the major upward motion starts. This point can be located at the lowest point on the early motion part. As the distance from the source increases, the early motion starts to show a double curvature trace with a minimum point ahead of the theoretical arrival time as shown in Figure 7.2. In this case, it is clear that the arrival time would be best selected at the point where the big upward movement starts.

Both results for the close range and the long range targets, therefore, reveal that the point where the major upward motion starts is always the best point to represent the first shear wave arrival time irrespective of the shape of the early motion curve. This approach will, therefore, be used throughout this work.

7.2   EFFECT OF THE INCLUSION SIZE AND WAVELENGTH

Some results in Chapter 6 had already shown a trend of a faster shear wave velocity with the increase in the size of the inclusion. This is reasonable because the wave travel more in the inclusion which has a higher wave velocity. On the other hand, if the inclusion has a lower shear wave velocity, the effect should reverse. It is obvious that if the travelling path of the wave in an inclusion "d_b" makes up a large portion of the total travelling path "d", the effect of the inclusion size would be much more pronounced as shown in Figure 7.3. In this fig-ure, the displacements for square inclusions of different sizes (a/λ = 1/4 and 1/8) are plotted together with the free field displacement, all
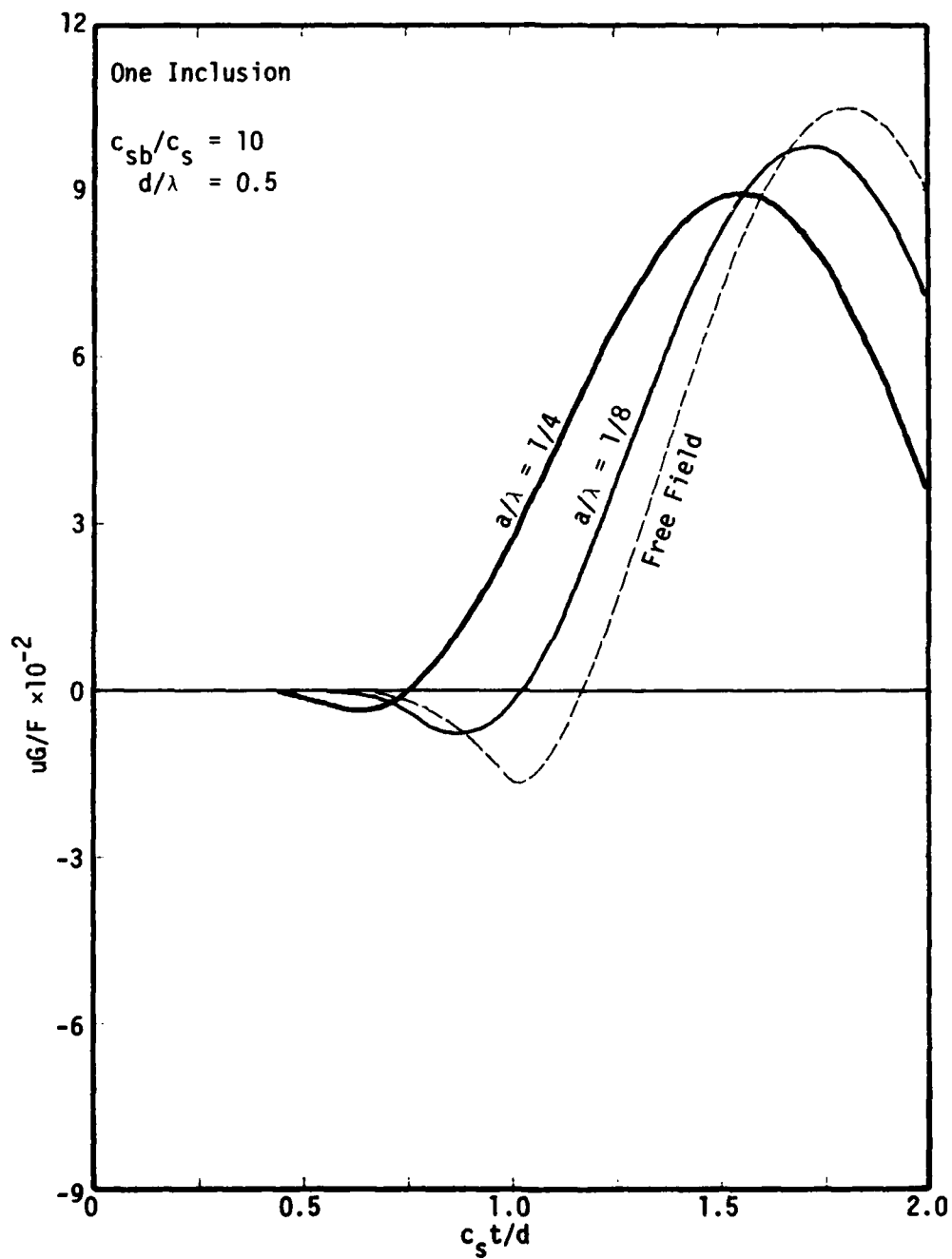
Figure 7.3 - Displacement versus Time for Different Sizes of
Inclusion

at $d/\lambda = 0.5$. The shear wave velocity of the inclusions in this case is ten times faster than that of the medium while other properties are the same. The figure clearly shows that the displacement curve shifts to the left as the inclusion size and the travelling path d_b increase.

Figure 7.4 shows the variation of the dimensionless variable $c_s t/d$ versus d_b/d (d_b length of the inclusion in the direction of propagation, d distance between the source and the target) for a one-dimensional situation where only one ray would travel through the distance $d-d_b$ with a velocity c_s and through the distance d_b with a velocity c_{sb}. For this simplified situation, one can define an equivalent distance

$$d_e = d - d_b + d_b \frac{c_s}{c_{sb}} = d[1 - (1 - \frac{c_s}{c_{sb}}) \frac{d_b}{d}]$$

The time of arrival would then be

$$t = d_e/c_s$$

and

$$c_s t/d = d_e/d = 1 - (1 - \frac{c_s}{c_{sb}}) \frac{d_b}{d} = 1 + ((\frac{c_s}{c_{sb}}) - 1) \frac{d_b}{d}$$

When the inclusion is stiffer than the surrounding medium and therefore c_{sb}/c_s is larger than one, this formula should provide a lower bound to the solution for a two dimensional situation. On the other

$$d_e = [1 + (\frac{c_s}{c_{sb}} - 1)\frac{d_b}{d}]d$$

Equiv. Free Field Distance, $d_e = [1 + (\frac{c_s}{c_{sb}} - 1)\frac{d_b}{d}]d$

Equiv. First Arrival Time, $c_s t/d = [1 + (\frac{c_s}{c_{sb}} - 1)\frac{d_b}{d}]$
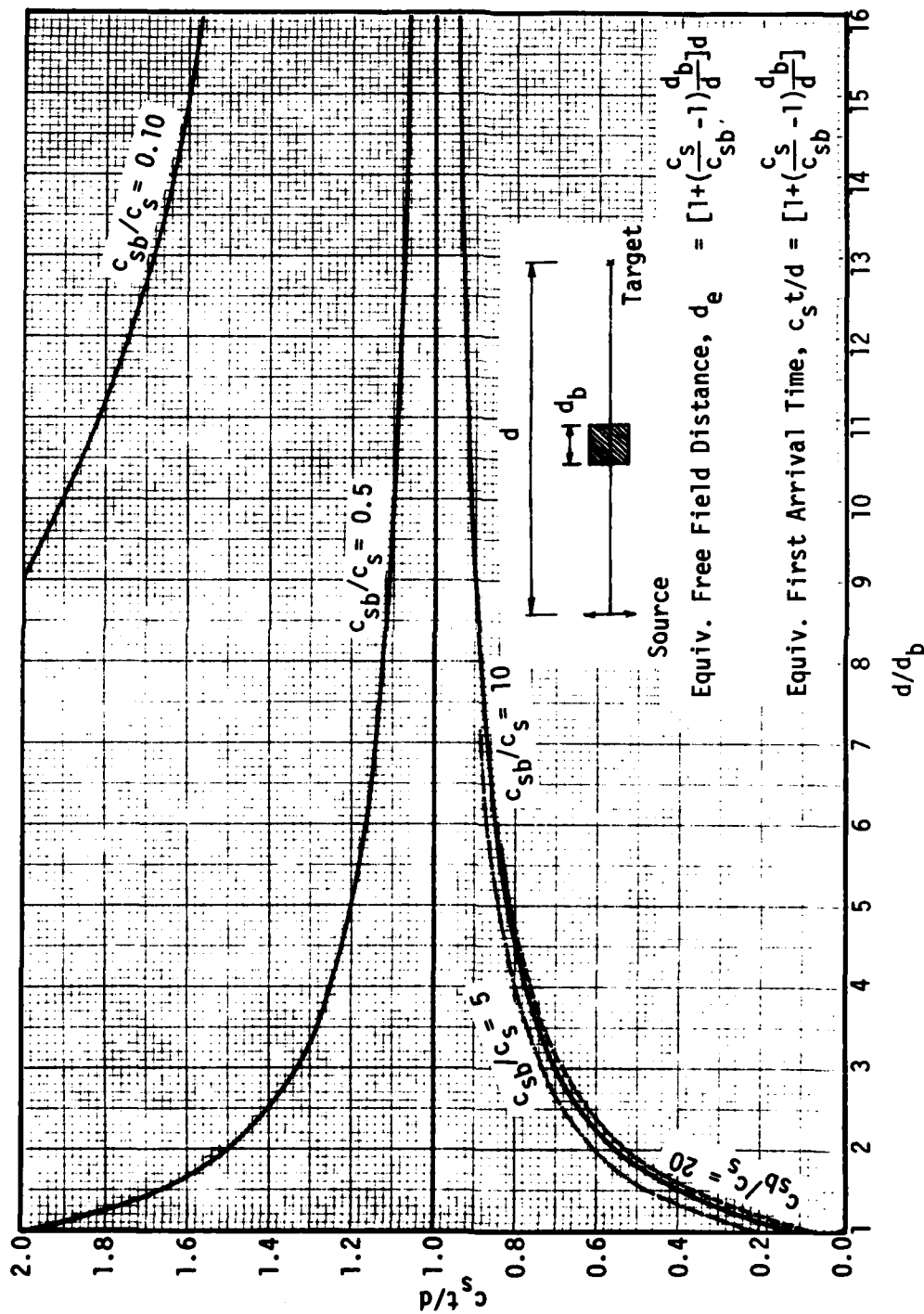
Figure 7.4 - Arrival Time Curves for 1-D Ray at Different Ratios c_{sb}/c_s, One Inclusion

hand, when the inclusion is softer than the medium the formula should provide an upper bound. Curves based on this formula will be used for the purpose of comparison when studying the effect of the inclusion on the time of arrival or apparent wave velocity for different inclusions.

The effect of the inclusion should be larger when dealing with ratios of d_b/d close to unity. This implies that both a source and a target point are relatively close to the inclusion. In this case, more boundary elements (or smaller element sizes) may be necessary to maintain the same level of accuracy. Plots of the arrival time versus the ratio d_b/d for the case $a/\lambda = 1/16$ using three different element sizes are shown in Figure 7.5. The case of the element length $\ell = \lambda/16$ corresponds to a single element per face of the inclusion, that is to say a total of four boundary elements. The case $\ell = \lambda/32$ corresponds to two elements per face and $\ell = \lambda/64$ to four elements per face (a total of 16 elements). It can be seen that, as the element size decreases, the arrival time curve shifts up and down (there is no monotonic convergence), and to reach the final position, the element size has to be very small. In our case, this final position was determined by judging from the results using two or three different element sizes.

The first arrival times $c_s t/d$ for different values of the ratio d/d_b are shown in Table 7.1 for three different wacelengths ($a/\lambda = 1/16$, 1/8, and 1/4). The values from this table are plotted in Figure 7.6 together with the curve for the 1-D ray for comparison. These plots show that the arrival time is larger as expected for the longer wavelength. This is because as the wavelength increases in relative to the inclusion
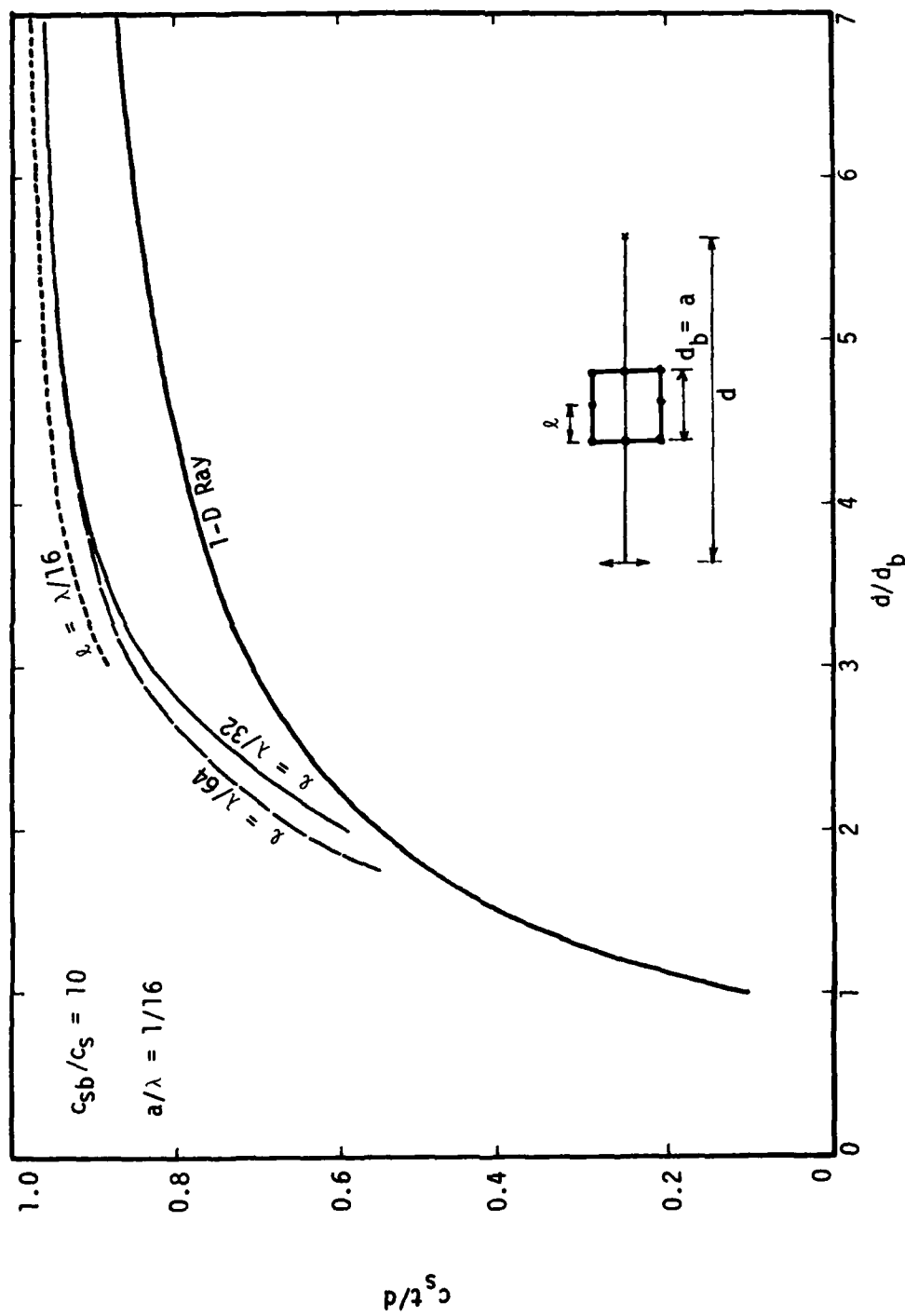
Figure 7.5 - First Arrival Time Using Different Element Size 'ℓ'

Table 7.1 - Values of $c_s t/d$ at the First Arrival of the Shear Wave

a/λ d/d_b	1/4	1/8	1/16
1.75	0.54	0.56	0.57
2.00	0.62	0.64	0.65
2.50		0.75	
3.00	0.79	0.82	0.85
4.00		0.90	
5.00	0.88	0.93	0.94
6.00		0.94	
7.00	0.90	0.94	0.96

$d_b=a$ (square inclusion)
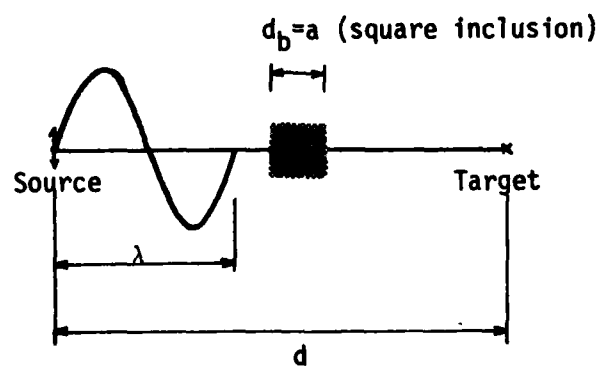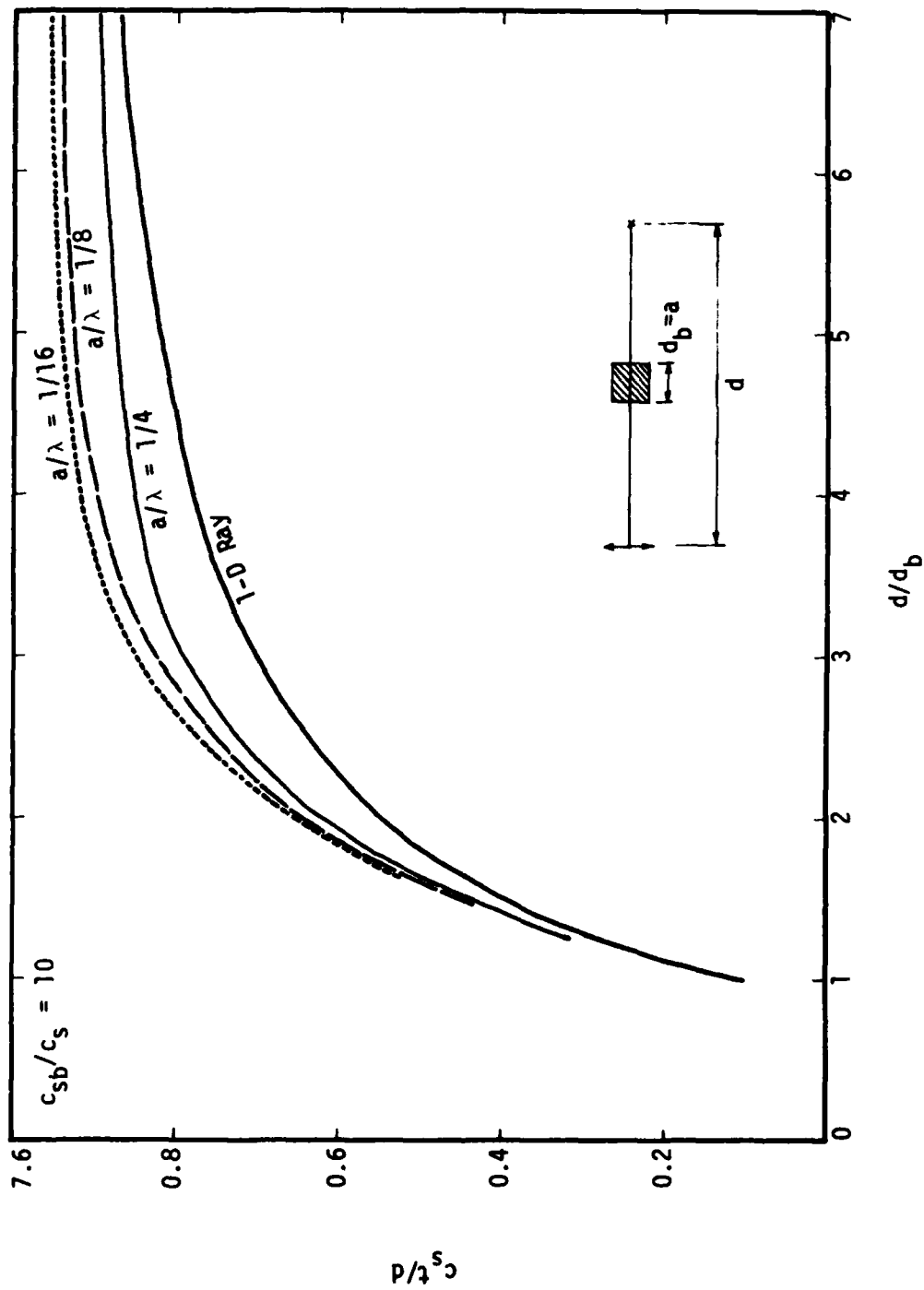
Figure 7.6 - Effect of Wavelength λ on the Arrival Time

size, most of the wave will propagate through the medium instead of the inclusion and the effect of the inclusion is thus smaller. As a result, the arrival time curve tends to be nearer to the upper bound at $c_s t/d$ of one (for the free field case). The results show that the decrease of the wavelength a/λ from 1/16 to 1/8 does not change the result as much as the decrease of a/λ from 1/8 to 1/4. This indicates the smaller effect from the inclusion when a/λ is less than 1/8.

7.3   EFFECT OF INCLUSION SHAPE

In the study of the effect of the shape of the inclusion, it is more difficult to standardize the procedure because of many types of shapes that can be considered. In addition, different inclusion shapes mean also different sizes. In an attempt to neutralize the effect of wavelength and the inclusion size as much as possible, two groups of shapes considered in this study are selected on the basis of two different criteria:

1. All inclusions have the same length of the wave path measured along the direction of propagation, (which is a one-dimensional consideration). The inclusion shapes in this group are a square, a vertical rectangle, a horizontal rectangle (having the same proportion as the vertical one) which is considerably smaller in order to meet the criterion, and lastly, a long vertical rectangle with a height of 1.125 of the wavelength.

2. All inclusions have the same cross-sectional area (which is more of a
    two-dimensional consideration). The inclusion shapes in this group
    are a vertical rectangle, a horizontal rectangle, a rhombus, a
    square, and a circle which is actually a dodecagon (12 sides polygon)
    because it is approximated by 12 straight elements.

The shapes and sizes of the inclusion of these two sets with the
relative size of the wavelength λ are shown in Figure 7.7. As in the
last section, the shear wave velocity of the inclusion used in this study
is ten times that of the medium, while another properties are the same,
and there is no damping in any of the materials.

The arrival time versus d/d_b curves for the inclusions under the
first set are shown in Figure 7.8. The arrival time is largest (smallest
apparent wave velocity, closest to that of the medium) for the case of a
horizontal rectangle whose size is much smaller than the rest in order to
satisfy the criterion. The wave velocity increases in the case of a
square, a vertical rectangular, and a long vertical rectangular inclu-
sions, consecutively. At larger distance, there is less difference in
the wave velocity between the case of a normal length and a long vertical
rectangle. These results indicate that the dimension of the inclusion
perpendicular to the direction of wave propagation affects also the sol-
ution for the two-dimensional case. As this dimension increases, the
solution should approach the one-dimensional curve.

Figure 7.9 shows the arrival time curves for the inclusions in
the second set. It can be seen that the wave velocity is slowest for a
rhombus and fastest for a square while the case of a circular inclusion

(a) Criteria 1, Same Principal Wave Path d_b

case 1a

Case 2a

case 3a

case 4a

Wavelength λ
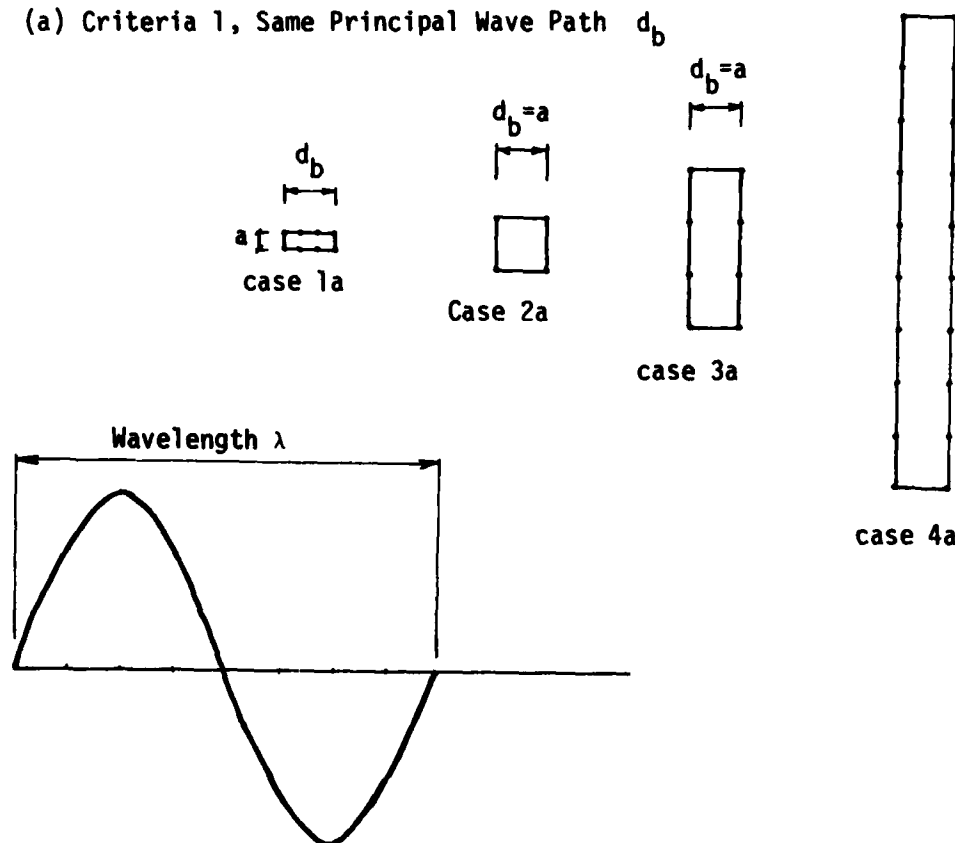
(b) Criteria 2, Same Total Area

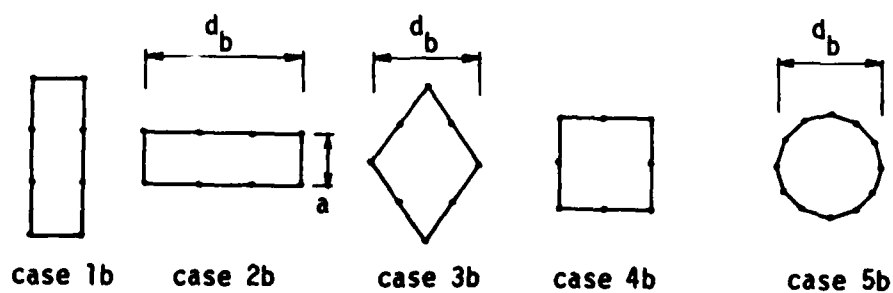case 1b case 2b case 3b case 4b case 5b

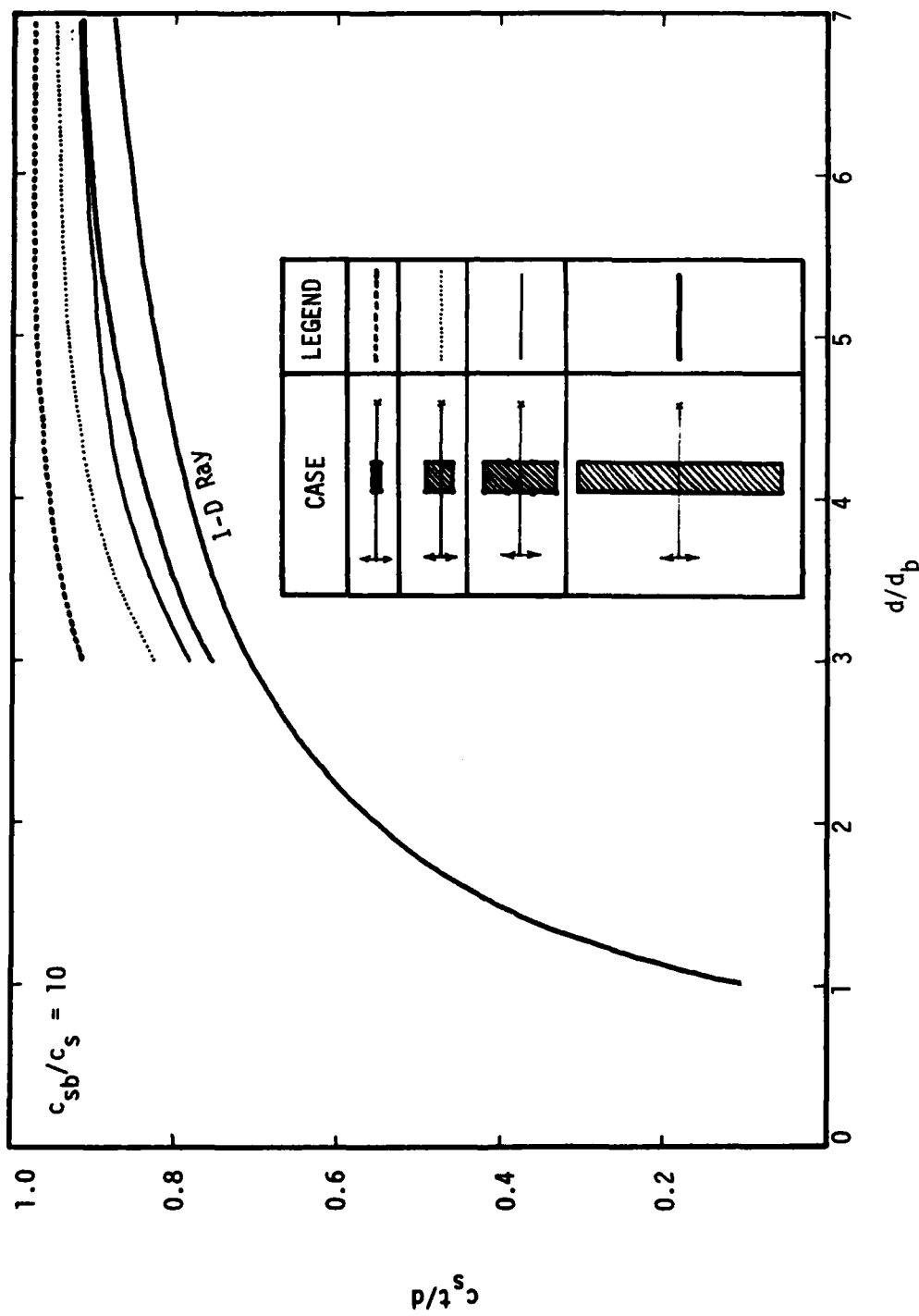Figure 7.7 - Shape of Inclusions Under Consideration

Figure 7.8 - Effect of Inclusion Shape on Arrival Time, Criteria 1
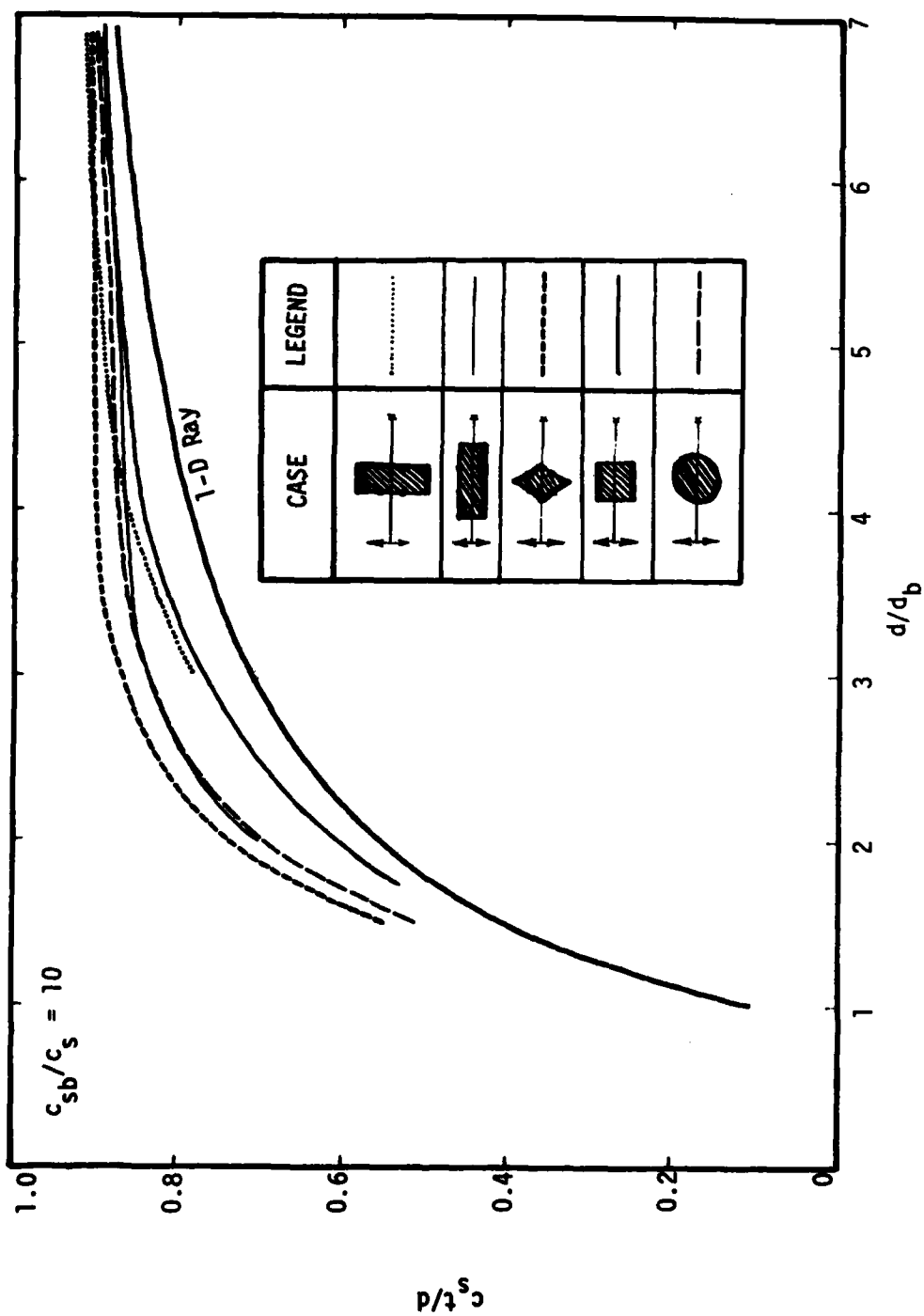
Figure 7.9 - Effect of Inclusion Shape on Arrival Time, Criteria 2

154

is in between. The case of a horizontal rectangle shows about the same wave velocity as that of the circle. The curve for the vertical rectangle shows a much faster wave velocity at small d/d_b (close to the case of a square inclusion) and slower as d/d_b increases.

It should be noted that of all five inclusion shapes considered, the rhombus and the circle have about the same length of the principal wave path d_b, both of which are slightly longer than that of a square inclusion. These three inclusions are, however, comparable in overall proportions. On the other hand, the vertical and the horizontal rectangles, each have significantly different path length from the rest. Because of this, the results from both rectangular shapes cannot compare well to the other cases since all plots are normalized on the basis of the value of the wave path's length.

The value of $c_s t/d$ at the first arrival time of the shear wave at different distances from source (normalized with the fixed wavelength λ) are tabulated in Table 7.2 and Table 7.3.

7.4   MULTIPLE INCLUSION

As in the case of the inclusion shape, it is difficult to select meaningful parameters to use as a basis for comparison between different arrangements of the inclusion cluster. The basis used in this section, which may not be the best, is that the total distance in the inclusions (d_b) along the principal axis of wave propagation is the same, as in the first criteria in the last section. In this section all inclusions con-

Table 7.2 - First Arrival Time $c_s t/d$ For Inclusions Under Shape Criterion 1

d/λ	First Arrival Time, $c_s t/d$				
	▬	■	▮	Long Vert. Rectangle length=$\frac{9}{8}\lambda$	1-D Solution
0.375	0.91	0.82	0.78	0.76	0.70
0.500	0.95	0.90	0.86	0.83	0.78
0.625	0.96	0.93	0.89	0.88	0.82
0.750	0.97	0.94	0.91	0.90	0.85
0.875	0.97	0.94	0.92	0.91	0.87

Table 7.3 - First Arrival Time $c_s t/d$ For Inclusions Under Shape Criterion 2

d/λ	First Arrival Time, $c_s t/d$				
	▮	▬	◆	◼	●
0.375	0.78		0.54	0.54	0.51
0.500	0.86		0.74	0.68	0.70
0.625	0.89		0.83	0.76	0.79
0.750	0.91	0.70	0.87	0.81	0.83
0.875	0.92		0.89	0.84	0.86
1.000			0.90	0.86	0.87
1.125		0.84	0.91	0.87	0.88
1.250			0.91	0.88	0.89
1.500		0.86	0.91	0.89	0.90
1.750			0.91	0.90	0.90
1.875		0.87			
2.250		0.88			

sidered are either rectangle or square with the least dimension "a" equal to 1/8 of the wavelength. The properties of the medium and the inclusions are as in the last section.

Figure 7.10 compares the arrival time curves between the case of a vertical rectangular inclusion and a group of three square inclusions aligned perpendicularly to the principal wave path. In both cases, the total area of the inclusions are also the same. The previous results for the case of one square inclusion are also shown for comparison. Of all three cases, the wave is fastest in the case of a rectangular inclusion and slowest in the case of one square inclusion. The results indicate that the effect on the wave velocity is maximum when the inclusion is in one large continuous piece serving as a long barrier so that most of the wave propagates through the inclusion. It appears that, for the case of an inclusion group, some of the wave can propagate through the medium between inclusions causing a smaller effect on the wave velocity.

In Figure 7.11, a similar comparison is made between the case of the horizontal rectangular inclusion and a group of three square inclusions oriented along the principal path of the propagating wave. Both cases have the same total length of wave path in the inclusions. The results show the faster wave velocity in the case of a continuous rectangular inclusion as in the previous case.

Figure 7.11 shows also the arrival time curve for a group of nine square inclusions arranged in a 3×3 block as shown. By comparing the results to those for a group of three inclusions, it can be seen that the addition of the extra rows of inclusions increases the wave velocity
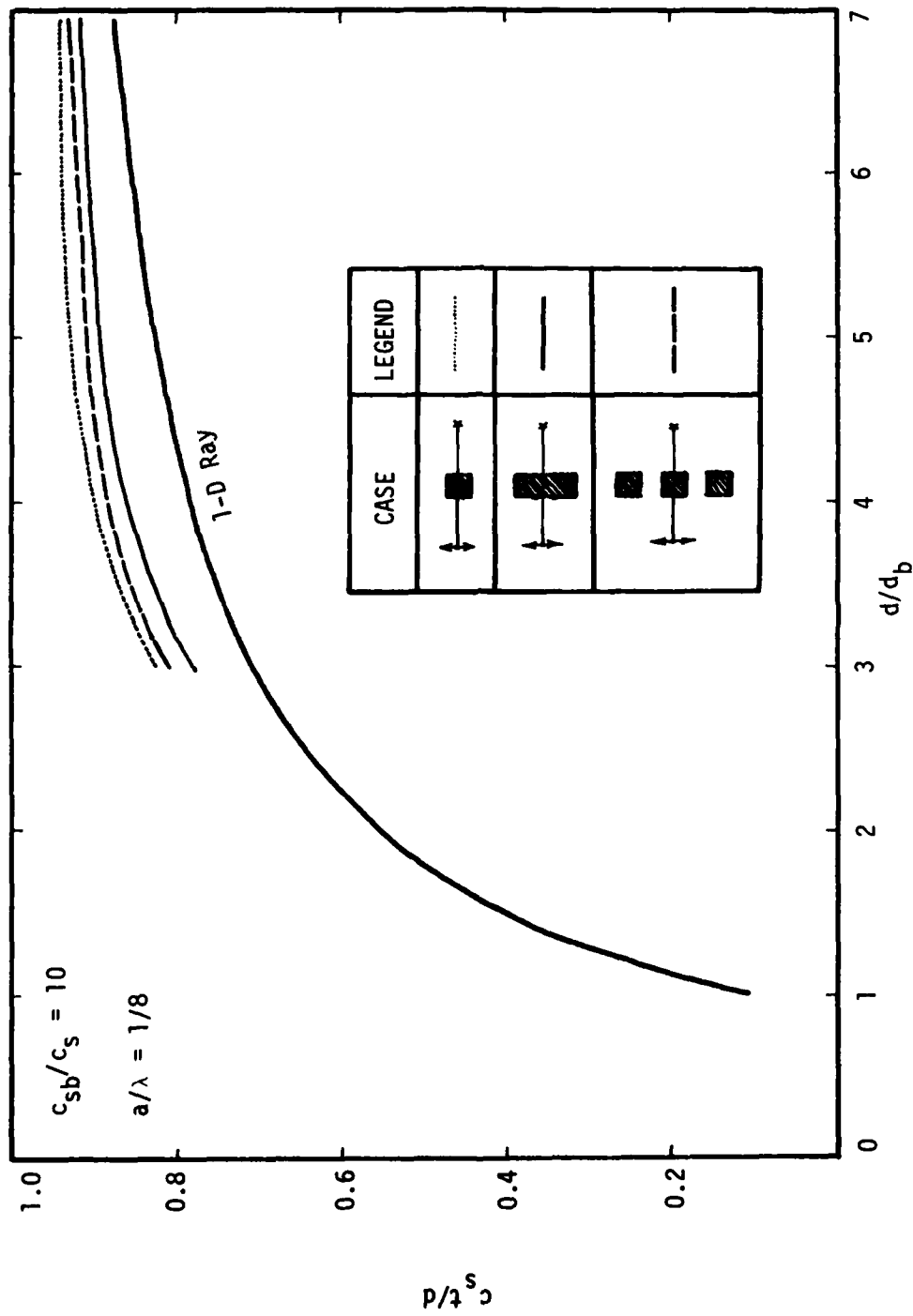
Figure 7.10 - First Arrival Time for the Inclusion Cluster vs. Single Inclusion
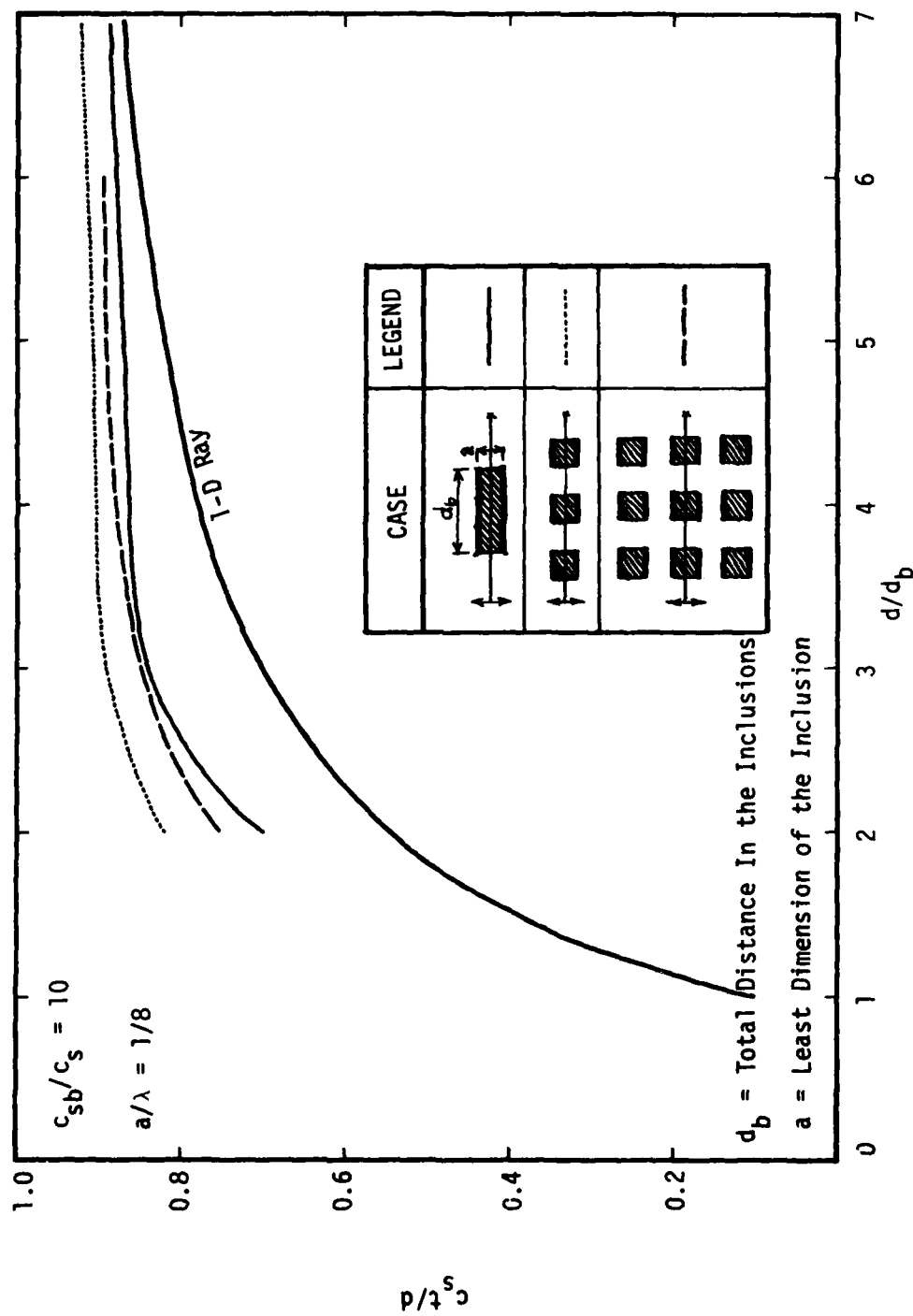
Figure 7.11 - First Arrival Time for the Inclusion Cluster vs. Single Inclusion

slightly, but it is still slower than from the case of one continuous inclusion.

As in the case of the vertical and the horizontal rectangle, the results between the inclusion cluster that are arranged vertically and horizontally cannot be compared very well as shown in the figures because of the different length of the total principal wave path "d_b" in the inclusions and, consequently, the dimensionless parameter d/d_b. On the basis of the same source-target distance "d", the horizontally aligned group has more effect of the wave velocity due to the longer "d_b" This can be seen in Table 7.4 and Table 7.5 (at $d/\lambda = 0.75$) where the values of $c_s t/d$ at the first arrival time of the shear wave at different distances (relative to the fixed wavelength λ) are tabulated for different inclusion clusters. The values for the single inclusions are also shown for comparison.

It can, therefore, be concluded that increasing the area of inclusions, either as a larger inclusion (compared with the wavelength) or a larger number of inclusions in a group, will increase the effect on the wave velocity. More importantly, for the equivalent total inclusion area, one large continuous inclusion will affect the wave velocity more than a group of several smaller inclusions (with the same total area and travelling path).

7.5   INCLUSION STIFFNESS

The results presented earlier dealt only with inclusion with a

Table 7.4 - First Arrival Time, Single and Group Inclusion, Vertical
Arrangement
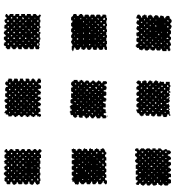
d/λ	First Arrival Time, $c_s t/d$	
0.375	0.78	0.81
0.500	0.86	0.88
0.625	0.89	0.91
0.750	0.91	0.92
0.875	0.92	0.93

Table 7.5 - First Arrival Time, Single and Group Inclusion, Horizontal and Mixed Arrangement

d/λ	First Arrival Time, $c_s t/d$		
0.750	0.70	0.82	0.75
1.125	0.84	0.89	0.85
1.500	0.86	0.90	0.88
1.875	0.87	0.90	0.89
2.250	0.88	0.91	0.89

shear wave velocity ten times (or shear stiffness of 100 times) that of the medium. In many real situations, the inclusions may have a wide range of shear wave velocities different from that of the medium. They may represent a rock or a boulder, a pocket of softer material, sand or silt in a soil deposit or even an underground structure. This section will shows the results of the shear wave arrival time for the case of a square inclusion ($a/\lambda = 1/8$) with different shear wave velocity ratios c_{sb}/c_s (0.1, 0.5, 5, 10, and 20) while other properties of the inclusion and the medium are the same. Both materials have no damping.

In the previous studies with an inclusion having c_{sb}/c_s of 10, the element size used, which is 1/8 of the wavelength, is normally adequate for an accurate result except when the source and the target are very close to the inclusion. In the study of inclusions with different stiffness, it was also found that the element size 1/8 of the wavelength works well until the ratio c_{sb}/c_s goes lower than 0.5 where the results start to be less reliable. This is demonstrated in Figure 7.12 where the displacement curves for an inclusion with c_{sb}/c_s of 0.1 using two different element sizes are plotted together. This is because the surface of the less stiff inclusion cannot retain the shape as in the case of the stiffer inclusion. The displacement at the surface is, therefore, larger and less uniform and cannot be accurately represented by just a few elements. In this section, more elements are, therefore, used.

Figure 7.13 shows the arrival time curves for different inclusion stiffness (c_{sb}/c_s of 0.1, 0.5, 5, 10, and 20). The curve for the free field case ($c_{sb}/c_s = 1.0$) is represented by a horizontal line at
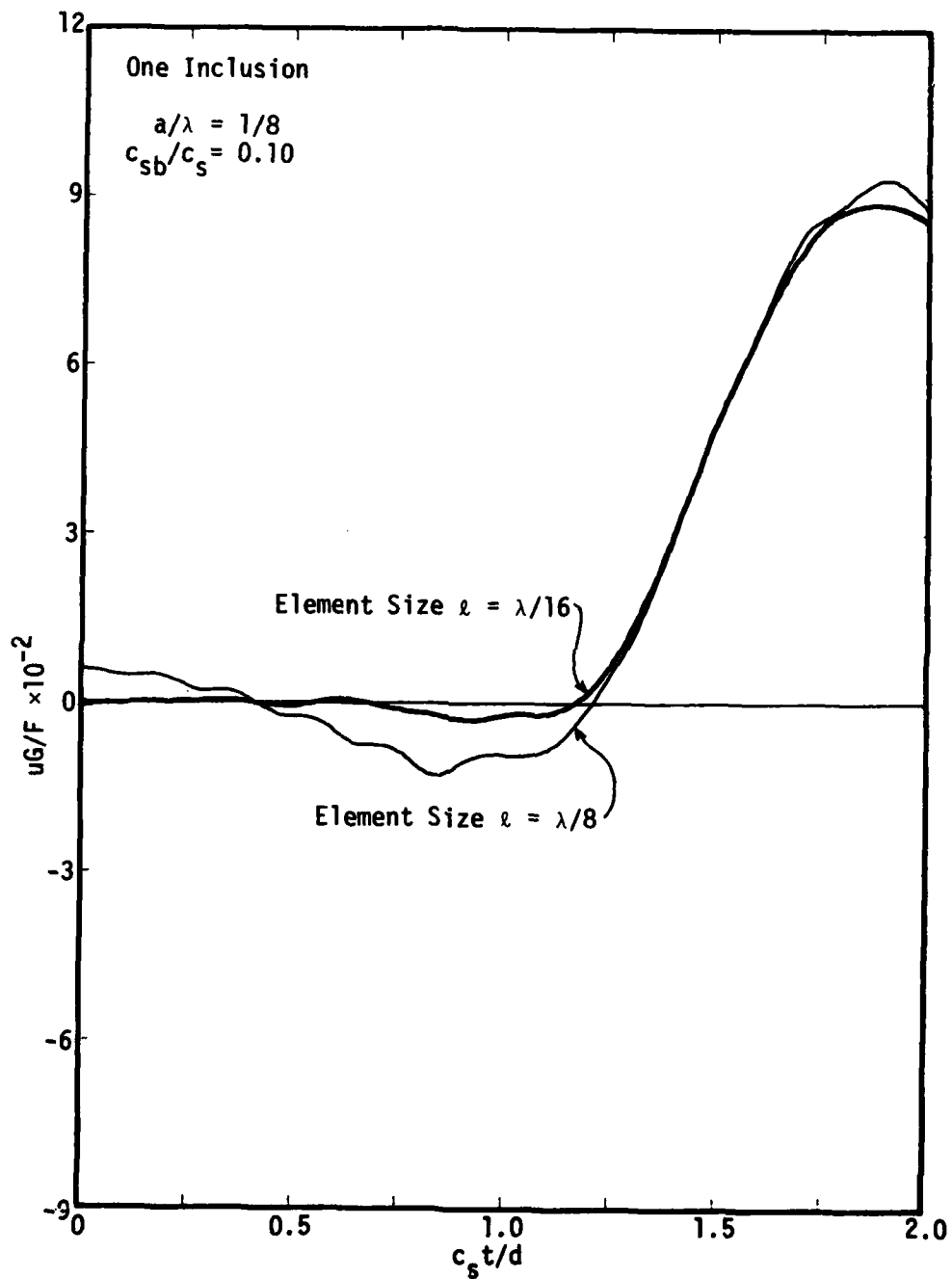
Figure 7.12 - Effect of Element Size on the Displacement in the
Case of Soft Inclusion
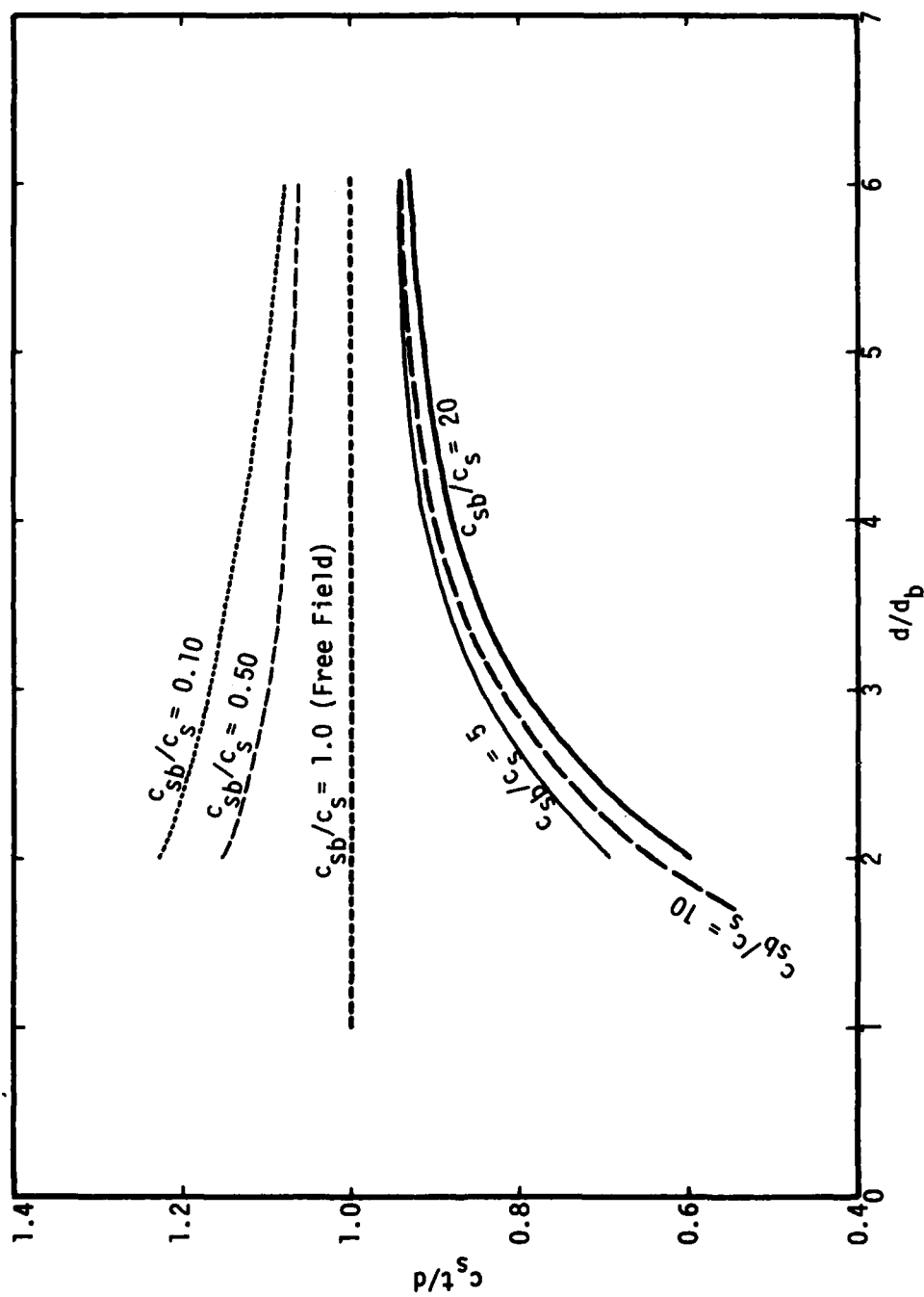
Figure 7.13 - Effect of the Inclusion Stiffness on the Arrival Time

$c_s t/d$ of one. The vertical scale in this figure is also displaced slightly to accommodate the plots for the case of c_{sb}/c_s less than one. The results show that the wave velocity is faster with the increase in the inclusion stiffness as expected. The arrival times for the cases where c_{sb}/c_s equals to 5, 10, and 20 are not much different from each other and these curves look similar to the curves of a 1-D ray shown in Figure 7.4, but somewhat higher. When the inclusion is less stiff than the medium, the wave velocity reduces slightly, not as much as in the case of a 1-D ray. This can be seen by comparing the arrival time curve for the case $c_{sb}/c_s = 0.1$ in Figure 7.13 and Figure 7.4. This result, therefore, reveals that the softer inclusions may not have a strong effect in reducing the overall wave velocity since the wave can arrive faster following a route of higher wave velocity.

7.6   INCLUSION MASS

Most of the inclusions considered so far have the same unit mass as the surrounding medium. Actually, the unit mass of the inclusion can also have a wide range of values from as low as an air void to a heavy buried structures.

To study the effect of the unit mass of the inclusion, stiff and soft inclusions are considered as in Section 6.3. The stiff and soft inclusions considered have c_{sb}/c_s of 10 and 0.5 respectively. In each case, the unit mass ratios between the inclusion and the medium are 0.5, 1.0, and 5.0.

Figure 7.14 shows the displacement versus time plots from the case of a stiff inclusion for all three unit mass ratios mentioned above. These results were selected from the target at $d/\lambda = 0.625$ because at such distance, it is not too close to an inclusion surface to make the results lack in accuracy, and it is yet small enough that the change of the arrival time can still be noticed easily. The plots show that the difference in the arrival times of the shear wave between the unit mass ratio of 0.5 and 1.0 are insignificant. With a further increase of the unit mass ratio up to 5.0, the increase in the arrival time is now more obvious. Figure 7.15 shows the same type of plots for the case of a soft inclusion with the same trends of results.
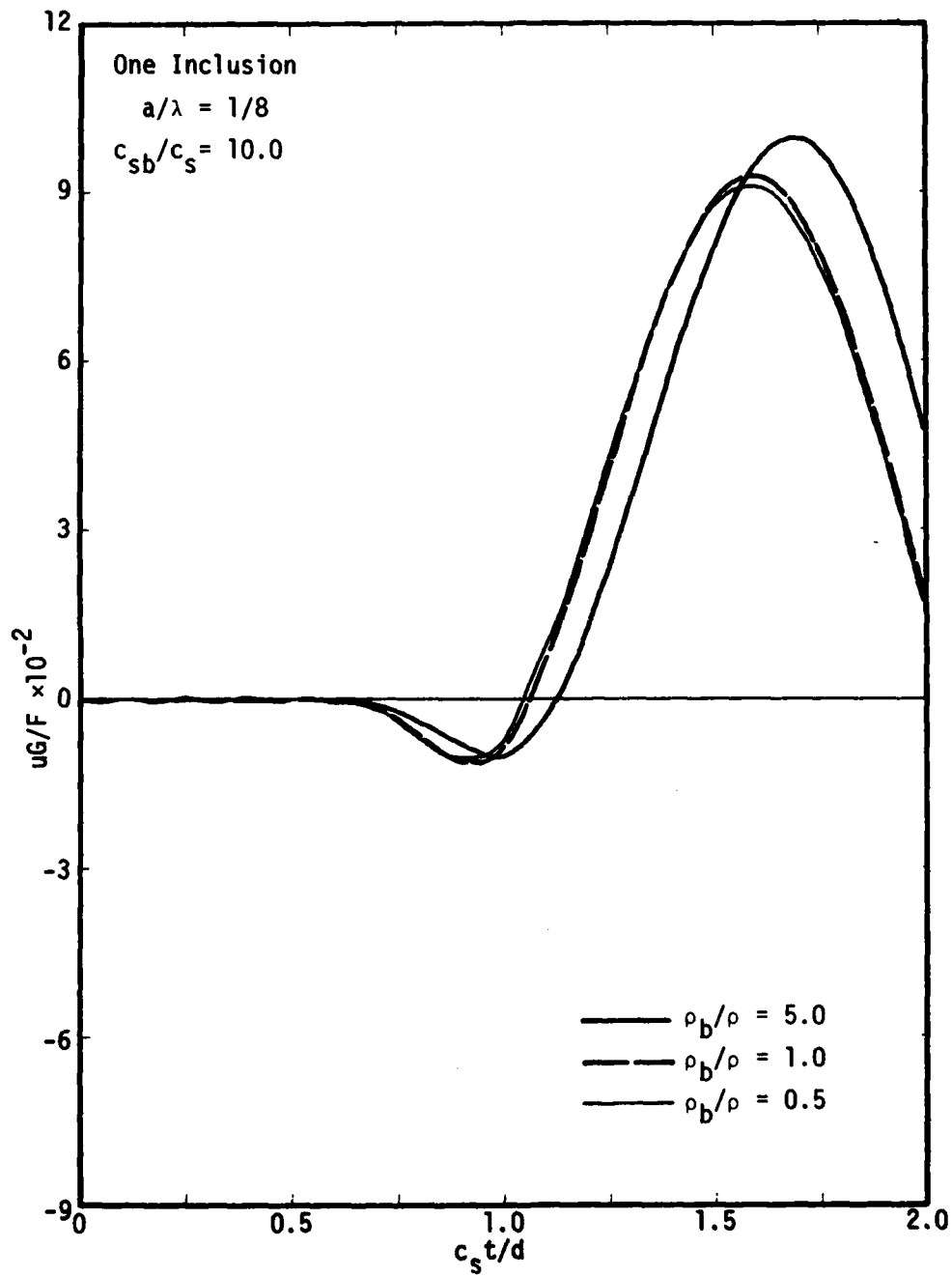
Figure 7.14 - Effect of the Unit Mass of the Inclusion, Stiff
Inclusion
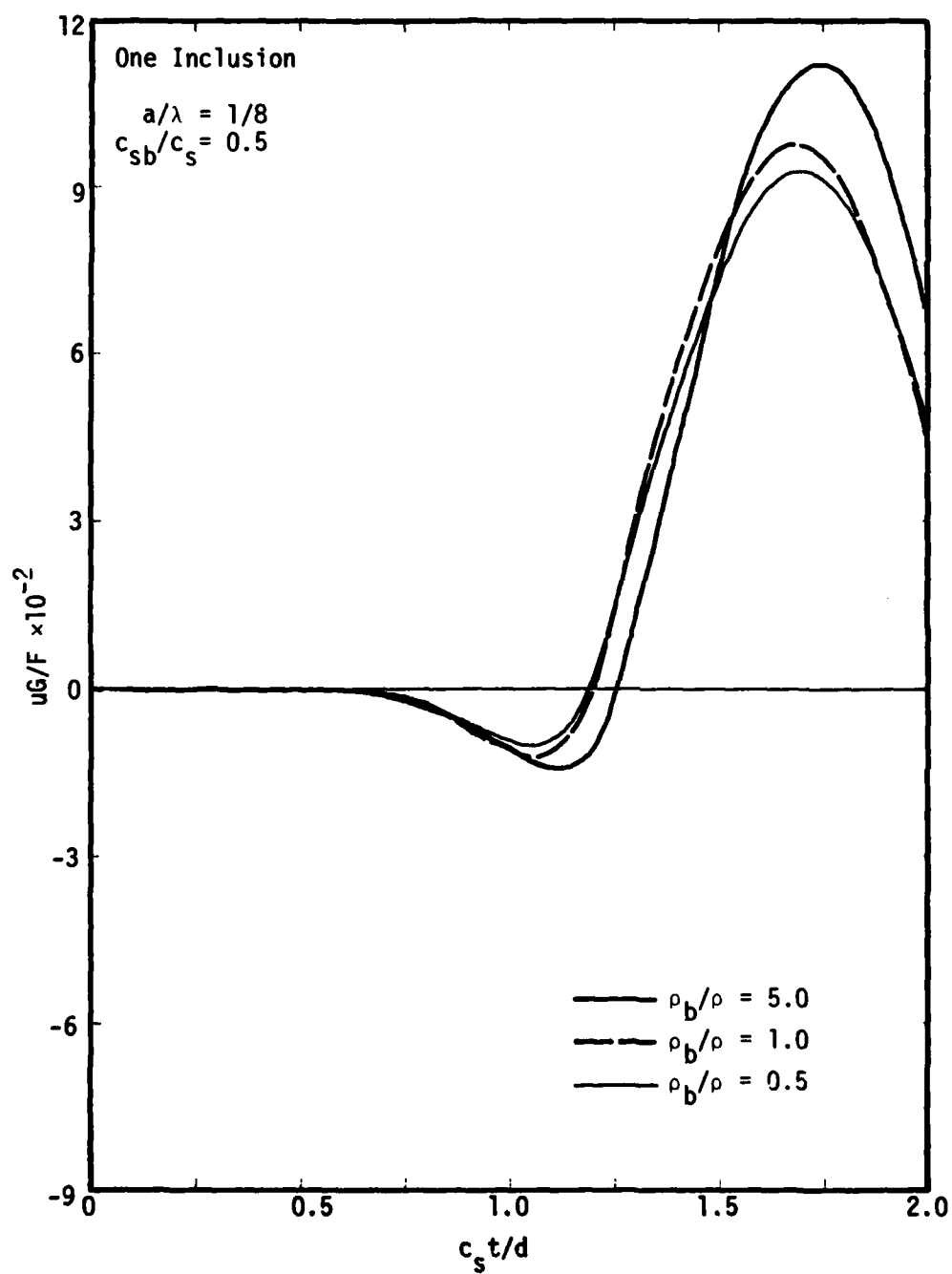
Figure 7.15 - Effect of the Unit Mass of the Inclusion, Soft Inclusion

CHAPTER 8

CONCLUSIONS

This research resulted as an ex'ansion of analyses performed to support an experimental investigation on the effect of the state of stresses on wave velocities in soil (Stokoe et al, 1980). In the original investigation, a model based on the finite element method (FEM) with an explicit integration scheme was implemented to simulate the propagation of waves inside a big triaxial cube containing soil, and the instrument packages as rigid inclusions. The procedure was suitable for that particular problem because of the finite domain and the possibility to study c ̊ferent boundary effects.

In this work, the more general area of wave propagation in a medium with inclusions having different properties is addressed by considering a full space so that boundary effects can be eliminated. In this case, an analysis in the frequency domain using the boundary element method has obvious advantages while the finite element model from the previous work was modified to approximate an infinite medium in order to compare the results to those of the BEM.

The FEM used in this work is based on the displacement method with a linear basis function and four-node rectangular elements. The equations of equilibrium for a finite element system in motion were

derived by applying Hamiltion's principle. With a lumped mass matrix, neglecting the velocity dependent damping forces and using an explicit integration scheme, the solution can be marched out in the time domain, at the element level, without assembling the global stiffness matrix. The time step of integration, however, has to be sufficiently small to guarantee stability. In this FEM model, an inclusion is represented by a single element, and an infinite medium is approximated by extending the boundaries far enough so that they have insignificant effects.

In the BEM, the formulation for both two and three dimensional cases was carried out in the frequency domain. Starting with the Betti-Maxwell reciprocity relation and a fundamental solution in transform space for a unit harmonic point force in an infinite medium, the expression for displacements (so called Somigliana's identity) is derived. The integral equation is then formed by taking the limiting case of Somigliana's identity for the point on the boundary. This procedure is carried out both for the inclusion and for the medium with cavities and the excitation force. Both parts are then combined to satisfy equilibrium and compatibility conditions leading to a system of equations that can be solved for displacements and tractions at the boundary. The displacements at any points in the domain can be solved using again Somigliana's identity. These displacements or transfer functions are solved at different frequencies and multiplied by the Fourier transform of the loading function. The inverse Fourier transforms of this product are then obtained to get the time responses.

A discrete Fourier transform based on the Fast Fourier transform (FFT) algorithm of Cooley and Tukey (1965), is used in this work. Since the transfer function has to be supplied at every frequency component in the FFT and the exact calculation for all of them will be prohibitively expensive, part of the transfer function will either be defined by interpolation or be neglected (truncation). Preliminary studies revealed that the use of extrapolated values worsened the results. Truncation was, therefore, used but the frequency beyond which the transfer function is neglected must be sufficiently high to reproduce the excitation frequency. In the preliminary studies, other parameters involved in frequency domain analyses, and the size of the finite element domain necessary to represent an infinite medium were also investigated.

The main body of this study focuses on the effect of inclusions on the wave attenuation, wave form, and wave velocity (in terms of arrival time) for shear waves. The results from the investigation lead to the following conclusions:

2-D Free Field Attenuation: BEM versus FEM

1. With a shear type excitation over a small area, which can be considered as a point (as used throughout this work), the displacement curves of both FEM and BEM show a small motion starting at the arrival time of the P-wave. This early motion flattens out very fast as the distance from the source increases. The displacement curve from the FEM is smoother and decays with an oscillatory motion after

the loading cycle in contrast with the asymptotic decay obtained with the BEM. Both positive and negative peaks in the FEM results are almost the same in amplitude while for the BEM, the positive amplitude is considerably larger than the negative one.

2. For a material without internal damping, the positive peak amplitude from the FEM is larger at close range and smaller as d/λ increases than that obtained from the BEM, which implies that the attenuation rate is slightly faster for the former. Furthermore, the plot of amplitude versus distance for the FEM is a curve throughout. This behaviour looks similar to that of systems with a small amount of material damping, indicating that the FEM model used introduces some fictitious damping in the solution (less than 1 percent).

Free Field Attenuation: 2-D versus 3-D

3. The displacement versus time plot for the three-dimensional case shows also a small early motion starting at the P-wave arrival time. Except for this early motion, the three dimensional displacement curve retains very well the sinusoidal shape of the excitation because both positive and negative peaks are almost the same in amplitude, and the displacement after a loading cycle is perfectly zero instead of decreasing asymtotically as in the two-dimensional case.

MICROCOPY RESOLUTION TEST CHART
NATIONAL BUREAU OF STANDARDS-1963-A

174

4. Damping in the medium not only reduces the amplitude of the displace-
ment but also smoothens out all abrupt changes in the motion and
results in a very smooth displacement curve. The velocity of the
shear wave and the period T of the motion appear to increase with
damping. These effects happen in both the two and the
three-dimensional cases.

5. Without damping in the medium, and at distances larger than twice the
wavelength, the log-log plots of amplitude versus distance are
straight lines with a slope equal to -1/2 and -1 for the two and the
three-dimensional cases respectively. In both cases, the plots are
no longer a straight line as d/λ decreases. The maximum curvature
occurs at a distance of approximately one wavelength ($d/\lambda = 1$). This
deviation from a straight line is due to the combination of SV and P
waves caused by the point excitation.

6. In a medium with damping, the log-log plots of amplitude versus dis-
tance are not straight lines. The maximum curvature also occurs
around $d/\lambda = 1$. In both the two and the three-dimensional cases the
curves have a steeper slope as damping increases indicating that the
waves attenuate faster.

the loading cycle in contrast with the asymptotic decay obtained with the BEM. Both positive and negative peaks in the FEM results are almost the same in amplitude while for the BEM, the positive amplitude is considerably larger than the negative one.

2. For a material without internal damping, the positive peak amplitude from the FEM is larger at close range and smaller as d/λ increases than that obtained from the BEM, which implies that the attenuation rate is slightly faster for the former. Furthermore, the plot of amplitude versus distance for the FEM is a curve throughout. This behaviour looks similar to that of systems with a small amount of material damping, indicating that the FEM model used introduces some fictitious damping in the solution (less than 1 percent).

Free Field Attenuation: 2-D versus 3-D

3. The displacement versus time plot for the three-dimensional case shows also a small early motion starting at the P-wave arrival time. Except for this early motion, the three dimensional displacement curve retains very well the sinusoidal shape of the excitation because both positive and negative peaks are almost the same in amplitude, and the displacement after a loading cycle is perfectly zero instead of decreasing asymtotically as in the two-dimensional case.

Attenuation in a Medium with an Inclusion: 2-D versus 3-D

7. For both the two and the three-dimensional cases, the attenuation rate with the presence of an inclusion is virtually the same as that in the free field although the overall amplitude is reduced. This indicates that the attenuation rate is not a good indicator of the presence of an inclusion.

8. The reduction in amplitude is more pronounced with the increase in the size of an inclusion (relative to the wavelength). In the two-dimensional case without damping, the reduction is almost constant in the range of d/λ from 2 to 20. As the damping ratio of the medium increases, the effect of an inclusion on the amplitude reduction decreases especially at larger values of d/λ. For all damping ratios, the maximum reduction of amplitude occurs at a distance of about 1.25 times the wavelength for an inclusion with size equal to 1/2 to 1/4 of the wavelength. For smaller inclusions, this distance decreases slightly. In the three-dimensional case, the reduction in the amplitude due to an inclusion is very small especially at large distances and for large damping ratios, which indicates that the geometrical damping and the material damping play a more important role than the inclusion in the reduction of the wave amplitude. It is thus very difficult to predict the existence of an inclusion from the amplitude reduction when there is internal damping, particularly if measurements are made at large distances.

9. Studies conducted for the two-dimensional case without damping show that, for different stiffness and mass density of the inclusion, the rate of wave attenuation is practically the same. An increase in the unit mass of the inclusion increases the amplitude slightly at all distance ranges. This overall increase in amplitude is also achieved with a decrease in the stiffness of the inclusion.

Effect of Inclusions on the Wave Velocity

10. The apparent velocity of the propagating waves is affected, as could be expected, by the presence of an inclusion along the wave path. It may become faster or slower depending upon the wave velocity (or stiffness) of the inclusion relative to the medium. The wave velocity for the system was computed from the first arrival time of the shear wave which is determined from the displacement versus time curve at the point where the major wave motion starts. This point is easy to detect at some distance and for a material without internal damping but it becomes harder to locate accurately at very short distances or when there is material damping.

11. The maximum effect on the arrival time of the shear waves obviously occurs when the travelling path of the wave consists largely of inclusions. This can be achieved either by increasing the size or the number of inclusions, or more specifically, increasing the total length of the inclusions in the direction of the wave propagation.

The size of the inclusion in the direction perpendicular to that of wave propagation also affects the shear wave velocity.

12. The solution provided by one-dimensional ray theory, computing directly the time of travel in both media gives a lower bound when the inclusion is stiffer than the surrounding soil and an upper bound in the opposite case.

Effect of the Inclusion Shape

Different shapes of inclusions were considered in this study. They were classified under two criteria: same length of the principal wave path; and same total area. None of these two criteria can provide a full description of the results but the former seems to be the better of the two.

13. Results from different inclusion shapes under the first criterion, ranging from a small horizontal rectangle to a long vertical rectangle, reveal that the length of the inclusion in the direction perpendicular to the principal wave path also affects the velocity of the wave. The results show that the longer this length is, the larger the effect, and the closer the curve is to the ray solution.

14. Results for the inclusions under the second criterion, for a horizontal rectangle, a vertical rectangle, a rhombus, a square, and a circle, show that the effect on the the arrival time of the wave is

178

least for a rhombic shape and largest for a square, while the results from the circular shape fall in between. The horizontal and the vertical rectangles also show results that are close to those for a circular shape. These two cases, however, cannot be compared well with others due to the difference in the length of the wave path in the inclusions (which is used as the normalizing parameter).

Multiple Inclusion Effect

15. Results for the case of multiple inclusions show that the larger the total area of inclusions (or the number of inclusions) the stronger the effect on the wave velocity. One large continuous inclusion affects the wave velocity, however, more than a cluster of several smaller inclusions with the same total area.

Effect of Inclusion Stiffness

16. With a stiffer inclusion in a medium, the apparent wave velocity should obviously increase. The results show that when the inclusion is less stiff than the medium, the change in the arrival time is not as pronounced as when the inclusion is stiffer (than the medium). This is because the wave can take a faster route around the inclusion.

Effect of the Unit Mass of the Inclusion

17. For the square inclusion considered ($a/\lambda = 1/8$), an increase in its unit mass of up to 100 percent does not significantly change the arrival time. The increase in the arrival time is more obvious with a larger increase (above 300 percent) in the unit mass of the inclusion.

This work was intended to demonstrate the numerical formulation of the boundary element method to solve the problem of wave propagation in an infinite medium with inclusions having different properties. Using this formulation, further parametric studies on the effect of inclusions should be conducted. The use of a higher order element to improve the efficiency of the model should also be investigated. Another area which deserves further research is that of wave propagation in a nonhomogeneous semi-infinite medium. This may be done either by discretizing the soil surface in addition to the soil-inclusion contact surface (Dominguez, 1978), or by using the dynamic Green's function for a semi-infinite medium (Johnson, 1974; Apsel and Luco, 1983; Luco and Apsel, 1983). In this way, a more practical model for wave propagation in soils, including surface waves and the effects of inclusions can be investigated.

BIBLIOGRAPHY

Abramowitz, M. and I.A. Stegun (1965) <u>Handbook of Mathematical Functions</u>, Dover, New York, 1965.

Apsel, R.J. and J.E. Luco (1983) "On the Green's Functions for a Layered Half Space. Part II," <u>Bulletin of the Seismological Society of America</u>, Vol.73, No.4, August 1983.

Banerjee, P.K. (1971) "Foundation within a Finite Elastic Layer, Application of the Integral Equation Method," <u>Civil Engineering</u>, November 1971.

Barnerjee, P.K. and R. Butterfield (1981) <u>Boundary Element Methods in Engineering Science</u>, McGraw-Hill (UK), 1981.

Baron, M.L. and A.T. Matthews (1961) "Diffraction of a Pressure Wave by a Cylindrical Cavity in an Elastic Medium," <u>Journal of Applied Mechanics</u>, Vol. 28, 1961.

Bathe, K. and E.L. Wilson (1976) <u>Numerical Method in Finite Element Analysis</u>, Prentice-Hall, Englewood Cliffs, N.J., 1976.

Brebbia, C.A. ed. (1978) <u>Recent Advances in Boundary Element Methods</u>, Pentech Press, London, 1978.

Brebbia, C.A. (1978) <u>The Boundary Element Method for Engineers</u>, Pentech Press, London, 1978.

Brebbia, C.A. and S. Walker (1980) <u>Boundary Element Techniques in Engineering</u>, Butterworth and Co., Ltd., London, 1980.

Brebbia, C.A. ed. (1981) "Boundary Element Method," <u>Proceeding of the Third International Seminar, Irvine, California</u>, Springer-Verlag Berlin, Heidelberg, 1981.

Cole, D.M., D.D. Kolsloff, and J.B. Minster (1978) "A Numerical Boundary Integral Equation Method for Elastodynamics I," <u>Bulletin of the Seismological Society of America</u>, Vol. 68, 1978.

Cooley, J.W. and J.W. Tukey (1965) "An algorithm for Machine Calculation of Complex Fourier Series," <u>Math Computation</u>, Vol. 19, 1965.

Cruse, T.A. (1968) "A Direct Formulation and Numerical Solution of the General Transient Elastodynamic Problem II," Journal of Mathematical Analysis and Applications, Vol. 22, 1968.

Cruse, T.A. and F.J. Rizzo (1968) "A Direct Formulation and Numerical Solution of the General Transient Elastodynamic Problem I," Journal of Mathematical Analysis and Applications, Vol. 22, 1968.

Cruse, T.A. and F.J. Rizzo eds. (1975) "Boundary Integral Equation Method:Computational Applications in Applied Mechanics," AMD-Vol. 11, ASME, New York, 1975.

Dominguez, J. (1978) "Dynamic Stiffness of Rectangular Foundations," Research Report R78-20, Dept. of Civil Engineering, MIT, 1978.

Doyle, J.M. (1966) "Integration of the Laplace Transformed Equations of Classical Elasto-kinetics,"Journal of Mathematical Analysis and Applications, Vol. 13, 1966.

Eringen, A.C. and E. Suhubi (1975) Elastodynamics, Vol. II, Academic Press, New York, 1975.

Ewing, M., W. Jardetzky, and F. Press (1957) Elastic Waves in Layered Media, McGraw-Hill, New York, 1957.

Hardin, B.O. (1975) "The Nature of Damping In Sands," Journal of the Soil Mechanics and Foundations Division, ASCE, Vol. 91, No. SM1, 1975.

Jaswon, M.A. and A.R. Ponter (1963) "An Integral Equation Solution of the Torsion Problem," Proc. Royal Soc., Series A, Vol. 273, 1963.

Johnson, L.R. (1974) "Green's Function for Lamb's Problem," Geophysical Journal of the Royal Astronomical Society, Vol. 37, No. 1, 1974.

Kupradze, V.D. (1963) "Dynamic Problems in Elasticity," Progress in Solid Mechanics, Vol. III, (I.N. Sneddon and R. Hill eds.), Wiley-Interscience, New York, 1963.

Ligget, J.A. and P.L-F. Liu (1983) The Boundary Integral Equation Method for Porous Media Flow, George Allen&Unwin, Ltd., London, 1983.

Love, A.E.H. (1944) A Treatise on the Mathematical Theory of Elasticity, Dover, New York, 1944.

Luco, J.E. and R.J. Apsel (1983) "On the Green's Functions for a Layered Half Space, Part I," Bulletin of the Seismological Society of America, Vol. 73, No. 41, 1983.

182

Massonet, C.E. (1965) "Numerical Use of Integral Procedures," Stress Analysis, (O.C. Zienkiewicz and G.S. Holister, eds.), Wiley, New York, 1965.

Miklowitz, J. (1966) "Elastic Wave Propagation," Applied Mechanics Surveys, (H. Abramson, et al eds.), Spatan Books, 1966.

Miklowitz, J. (1978) The Theory of Elastic Waves and Waveguides, North-Holland Publishing Co., 1978.

Oliveira, E.R.A. (1968) "Plane Stress Analysis by a General Integral Method," Journal of the Engineering Mechanics Division, ASCE, Vol. 97, 1968.

Pao, Y.H. and C.C. Mow (1973) Diffraction of Elastic Waves and Dynamic Stress Concentrations, Crane, Russik & Co., Inc., New York, 1973.

Rizzo, F.J. (1967) "An Integral Equation Approach to Boundary Value Problem of Classical Elastostatics," Quart. Appl. Math, Vol. 25, 1967.

Scaletti Farina, H. (1977) "Nonlinear Effects in Soil Structure Interaction," Ph.D. Dissertation, Civil Engineering Dept., MIT, September 1977.

Stokoe II, K.H., et al (1980) "Development of A Large-Scale Triaxial Testing Device for Wave Propagation Studies," Geotecnical Engineering Report GR80-10, The University of Texas, Austin, Texas, 1980.

Suddhiprakarn, C. (1983) "Effects of Rigid Inclusions on Wave Propagation," Geotecnical Engineering Report GR83-3, The University of Texas, Austin, Texas, 1983.

Symm, G.T. (1963) "Integral Equation Methods in Potential Theory II," Proc. Roy. Soc. A, Vol. 275, 1963.

Tomlin, G.R. and R. Butterfield (1974) "Elastic Analysis of Zoned Orthotropic Continua," Journal of the Engineering Mechanics Division, ASCE, No. EM3, 1974.

Zienkiewicz, O.C. (1978) The Finite Element Method, Third Edition, McGraw-Hill, London, 1978.